

DEVELOPMENT OF EXPERIMENTAL  
AND FINITE ELEMENT MODELLING  
TECHNIQUES FOR INVESTIGATION OF  
HUMAN FEMURS

THESIS SUBMITTED FOR THE DEGREE OF  
DOCTOR OF PHILOSOPHY  
AT THE UNIVERSITY OF LEICESTER

by

Caroline Meakin

Department of Physics and Astronomy

University of Leicester

April 2017

# Abstract

Development of Experimental and Finite Element Modelling Techniques for

Investigation of Human Femurs

Caroline Meakin

The aim of the work presented in this thesis was to develop a finite element model and experiment to simulate the loading conditions caused by a fall on the proximal femur. Investigations were carried out with a PVC surrogate human femur and a sheep's femur. The results of the model and experiment were used to assess the effect of the orientation of the femur at time of impact on the strain distribution.

The finite element model was based on data obtained from computed tomography scans of the samples, which were used to characterise their geometry and material properties, and included a simulation of the contact mechanics in the hip joint. The experiment involved the use of strain gauges to measure strain at a number of locations on the samples. Apparatus was developed to support the samples at a range of orientations with respect to the direction of an applied load. Trilateration was used to identify the model coordinates of the strain gauges. The accuracy of the model, assessed by comparison with the results of the experiment, was found to be limited by restrictions in the resolution of the CT data.

An investigation into the effect of multiple freeze-thaw cycles on strain gauge measurements showed that the accuracy of strain readings taken after four cycles could not be guaranteed. The use of different materials to simulate the acetabular surface through which the load is applied to the femoral head was determined to have a significant effect on the strain, as was the difference between using a foam soft tissue surrogate and a hard PMMA cap to protect the greater trochanter.

The effect of changing the angle of rotation about the shaft of the femur was assessed. It was found that the largest strains per unit force were associated with posterolateral falls.

# Acknowledgements

I would like to thank my supervisors, Peter Maksym, Simon Gill, and Simon Conroy, for their extensive support, advice, and guidance which have been essential to me completing this thesis. I would also like to thank all members of staff in the Department of Physics and Astronomy and the Department of Engineering, as well as at Leicester Royal Infirmary and Glenfield Hospital, whose help has been of immense value.

---

# Contents

<b>1</b>	<b>Introduction</b>	<b>1</b>
1.1	Falls and Hip Fracture . . . . .	2
1.2	Finite Element Modelling and Experimental Investigation of Hip Fracture - A General Review . . . . .	4
1.3	The Structure of This Thesis . . . . .	8
<b>2</b>	<b>CT Characterisation of Femoral Bone and Finite Element Modelling of Bone Tissue</b>	<b>10</b>
2.1	Introduction . . . . .	10
2.2	Modelling bone tissue . . . . .	11
2.2.1	Computed Tomography . . . . .	11
2.2.1.1	Geometry . . . . .	11
2.2.1.2	Material Properties . . . . .	12
2.2.2	Densitometry of sheep femur . . . . .	15
2.3	Preliminary Finite Element Model - PVC . . . . .	19
2.3.1	Model . . . . .	20
2.3.2	Results . . . . .	22
2.4	Preliminary Finite Element Model - Bone . . . . .	25
2.4.1	Model . . . . .	26
2.4.2	Results . . . . .	27
2.5	Discussion . . . . .	31
2.6	Conclusion . . . . .	32
<b>3</b>	<b>Strain Measurement Techniques for Femoral Bone</b>	<b>34</b>
3.1	Introduction . . . . .	34

3.2	Strain Measurement . . . . .	35
3.2.1	Apparatus . . . . .	35
3.2.2	Applying Strain Gauges to Bone . . . . .	37
3.3	Distal Fixture . . . . .	38
3.3.1	PMMA . . . . .	40
3.4	Freeze-Thaw Cycling . . . . .	43
3.4.1	Freeze-Thaw Experiment . . . . .	43
3.4.2	Results . . . . .	45
3.4.2.1	Statistical Data Analysis . . . . .	47
3.5	Conclusion . . . . .	50
<b>4</b>	<b>Computational and Experimental Investigation of Strain in a PVC Femur Model</b>	<b>52</b>
4.1	Introduction . . . . .	52
4.2	Experiment . . . . .	54
4.2.1	Design . . . . .	54
4.2.1.1	Load Cell Attachment . . . . .	55
4.2.1.2	Tower . . . . .	57
4.2.2	Measuring and Recording Strain . . . . .	59
4.2.3	Experimental Method . . . . .	61
4.3	Identification of Gauge Locations . . . . .	62
4.3.1	Trilateration . . . . .	63
4.3.2	Analysis of Errors in Gauge Location Measurement . . . . .	66
4.4	Model . . . . .	68
4.4.1	Contact Physics . . . . .	68
4.4.1.1	Comsol . . . . .	68
4.4.1.2	Hertzian Contact . . . . .	69
4.4.2	Model Design . . . . .	71
4.4.3	Calculating Strains in the Model . . . . .	73
4.4.3.1	Strain Direction in Single Gauges . . . . .	73
4.4.3.2	Strain Direction in Rosette Gauges . . . . .	75
4.5	Results . . . . .	76
4.6	Conclusion . . . . .	83

<b>5</b>	<b>Computational and Experimental Investigation of Strain in a Sheep's Femur</b>	<b>85</b>
5.1	Introduction . . . . .	85
5.2	Experiment . . . . .	86
5.2.1	Load Cell Attachments . . . . .	87
5.2.2	Greater Trochanter protection . . . . .	88
5.2.3	Method . . . . .	90
5.3	Model . . . . .	93
5.3.1	Trilateration . . . . .	96
5.4	Results . . . . .	97
5.4.1	Comparison of Experimental Results . . . . .	97
5.4.2	Comparison of Experimental and Model Results . . . . .	104
5.4.2.1	Young's Modulus Compensation . . . . .	109
5.5	Conclusion . . . . .	110
<b>6</b>	<b>Conclusion</b>	<b>113</b>
6.1	Overview . . . . .	113
6.2	Outcomes . . . . .	114
6.3	Limitations and Future Work . . . . .	115

---

# List of Tables

2.1	Minimum and maximum values of ash density and Young's modulus.	26
3.1	Test statistic, $p=0.05$ threshold test statistic, and $p$ -value associated with the two null hypotheses calculated for data collected following each repeated week. . . . .	50
4.1	Distances of each gauge from each of the three reference points. . . .	64
4.2	Distance from selected gauge node in mm of points with deviations of $\pm 0.5$ mm from the original measurements of one, two, or three radii.	66
4.3	Distance from selected gauge node in mm of points with deviations of $\pm 0.25$ mm from the original measurements of one, two, or three radii.	67
5.1	Distances of each gauge from each of the three reference points on the sheep femur. . . . .	96
5.2	$t$ -test statistics calculated from results taken with the same cells . . .	102
5.3	$t$ -test statistics calculated from results taken with the same greater trochanter protectors . . . . .	103

---

# List of Figures

1.1	Categorisation of hip fractures based on the region of the femur where they occur. . . . .	3
2.1	Images of both the PVC femur meshes before and after reduction. . .	13
2.2	The process of generating a mesh and spatially varying Young's modulus function within the finite element model. The left hand column shows the process used to import the linear attenuation data obtained during the scan, calibrate it to determine ash density, then calculate the Young's modulus. The right hand column shows the process used to generate the surface mesh for the femur. . . . .	16
2.3	Images of the sheep bone meshes before and after reduction. Parts of the plastic pot and calibration vials were present in the original file (visible in the left-hand image) and removed after reduction. . . . .	17
2.4	Sample slice (slice number 687) taken from scan of sheep femur and $K_2HPO_4$ calibration vials. All five vials are visible, along with a cross-section through the shaft of the femur. Expanded image shows $C = 1$ g/ml phantom vial. Pixels within the yellow box (24 by 23 pixels) were sampled along with data from 4 other slices to generate a mean and standard deviation for the linear attenuation of the contents of this vial. . . . .	17
2.5	Calibration graph of $K_2HPO_4$ concentration $C$ plotted against mean linear attenuation $\mu$ in each of the five phantom tubes. Error bars are the standard deviation in $\mu$ for the samples taken from each vial. . . . .	18

2.6	Clockwise, from top left: a sample image slice; the same slice after downsampling; the elastic modulus (GPa) plotted on a cut plane at the same $z$ value as the image slices; the location of the cutplane in the geometry of the proximal femur geometry. . . . .	19
2.7	Position on the PVC femur of a) boundary loads and b) fixed boundaries for each loading condition. c) the fixed boundaries for all loading conditions at the distal end of the femur . . . . .	20
2.8	Loading configuration of model depends on two angles: $\alpha$ - the angle of rotation about the shaft, and $\phi$ - the angle between the shaft and the floor. The point and direction of the applied 1 N load is shown with an arrow, and the floor is represented by a workplane. . . . .	21
2.9	Maximum surface principal strain induced on the surface of the PVC femur under 1 N load for each combination of $\alpha$ and $\phi$ : posterior (top row) and anterior (bottom row) view. The range of strains mapped was limited to $\pm 5 \mu\text{strain}$ . . . . .	23
2.10	Location of the three sampled test points. Suitable locations were selected by observation of the strain distribution, and under the condition that the femoral surface must be relatively smooth. . . . .	24
2.11	Maximum principal strain vs. $\alpha$ : PVC model. . . . .	25
2.12	Position on the sheep femur of a) boundary loads and b) fixed boundaries for each loading condition. c) the fixed boundaries for all loading conditions at the distal end of the femur . . . . .	26
2.13	Angles $\alpha$ and $\phi$ defining the loading conditions of the sheep bone model. Arrow shows point and direction of application of 1 N load. A workplane touching the greater trochanter represents the floor. . .	27
2.14	Maximum surface principal strain for each combination of $\alpha$ and $\phi$ for the homogeneous sheep femur model under 1 N load. The range of strains mapped was limited to $\pm 10 \mu\text{strain}$ . . . . .	28
2.15	Maximum surface principal strain for each combination of $\alpha$ and $\phi$ for the spatially dependent sheep femur model under 1 N load. The range of strains mapped was limited to $\pm 10 \mu\text{strain}$ . . . . .	29
2.16	Location of the three sampled test points on both sheep bone models.	30

2.17	Maximum principal strain vs. $\alpha$ : bone models. . . . .	31
3.1	a) The rosette gauges used in this project consist of three single strain gauges stacked a single backing foil. The gauges are aligned at $0^\circ$ , $45^\circ$ , and $90^\circ$ . b) Circuit diagram of the strain gauge quarter-bridge circuit in the two-wire and three-wire arrangement. Both lead wires are connected to the same arm of the bridge, resulting in an increased resistance in this arm and causing the bridge to become unbalanced. In the three-wire circuit, the lead wire resistances $R_{L1}$ and $R_{L2}$ are joined to separate arms of the bridge, one either side of the output sensor. If $R_{L1} = R_{L2}$ , the bridge will be balanced when $R_G = R_2 = R_3 = R_4$ . . . . .	35
3.2	Images from the CT scans of the bone cements test using a) only the instructions supplied with the cement and b) the procedure recommended by Eyerer and Jin. . . . .	41
3.3	The result of the first PMMA test, outer cylinder removed. The void spanning the entire thickness of the side of the cement is visible in the centre of the image. . . . .	42
3.4	The loading frame, with loaded rib, shown from above (photo) and the side (diagram). . . . .	45
3.5	Strain vs. number of masses for the data collected from each week. The data taken in each of the four loading cycles is plotted separately, but the intercept and slope is calculated for the all the data taken that week pooled together. It is assumed that the strain response to leading is linear. . . . .	46
4.1	CAD drawing of load cell attachment. . . . .	56
4.2	Apparatus used to support the distal end of the femur and provide an angled contact plane for the greater trochanter. The tab which is bolted onto the cylinder is visible in the right hand image. . . . .	58

4.3	The upper two images are taken from the CAD drawing of the apparatus, and shows the angles describing the loading conditions of the femur. The right femur is shown, as this model was used in the initial design of the apparatus. The angles are the same for the left femur, but the direction of $\alpha$ is reversed. The photograph shows the sheep's bone femur fixed into the apparatus and positioned in the loading frame beneath the load cell attachment. Exactly the same arrangement was used for the experiments with the PVC femur. The sheep's femur experiment will be discussed in the following chapter. . . . .	59
4.4	Load plotted against time output from Bluehill software. Red line shows regression line. First 15 seconds not used for regressional analysis.	60
4.5	Strain plotted against time, demonstrating the linear response to load (which increases linearly with time). The data taken during the first 15 seconds were removed when calculating the gradient, as the load measurements shown in figure 4.4 indicate that the programmed load increase per second cannot be assumed for these data. . . . .	60
4.6	Schematic representation of the geometric problem solved in the process of three-dimensional trilateration. The three spheres are constructed at the measured radii from the corresponding reference points. The spherical surfaces around $\mathbf{P}_1$ and $\mathbf{P}_2$ intersect along a circle $c$ . The third sphere intersects $c$ in at two points, $\mathbf{P}_a$ and $\mathbf{P}_b$ . . . . .	63
4.7	Locations in the model 3 reference points $\mathbf{P}_1$ , $\mathbf{P}_2$ , and $\mathbf{P}_3$ , and strain gauge points $R_1$ , $R_2$ , $S_1$ , and $S_2$ . . . . .	64
4.8	Contact. Most convex object is labelled "destination", most concave labelled and "source". Force acts between point on destination boundary and closest point on destination boundary in the perpendicular direction. . . . .	68
4.9	Contact pressure is calculated between regular shapes to provide an estimate of pressures between a) femoral head and acetabulum (sphere and cup), and b) greater trochanter and base plate (ellipsoid and plane). . . . .	70

4.10	Geometry of the PVC femur finite element model, including the imported femur geometry and the load cell attachment and floor block drawn in the Comsol environment. . . . .	72
4.11	Surface boundaries where the contact force was applied. . . . .	73
4.12	The surface strain tensor $\boldsymbol{\varepsilon}'$ calculated in the boundary coordinate system is rotated to give $\boldsymbol{\varepsilon}''$ , the 2-dimensional strain tensor in plane with the surface and with one component, $\varepsilon''_{11} = \varepsilon_{\text{gauge}}$ , parallel with the gauge. Anti-clockwise rotation (from $\mathbf{t}_1$ to $\mathbf{g}$ ) is positive. . . . .	75
4.13	Determination of $\beta$ in the model. $\beta$ is the angle between gauge direction vector $d_g$ and the first principal strain $\varepsilon_{p1}$ . . . . .	76
4.14	First principal strain at rosette gauge point $R_1$ . Correspondence between model and experimental results is good for both $\phi - \theta$ configurations. Experimental results show largest positive strains at extreme high and low $\alpha$ angles. . . . .	77
4.15	Second principal strain at rosette gauge point $R_1$ . Good correspondence between model and experimental results at low $\alpha$ angles, deviation begins at $90^\circ$ degrees for both $\phi - \theta$ configurations. Experimental results show largest negative strains at low $\alpha$ angles. . . . .	78
4.16	First principal strain at rosette gauge point $R_2$ . Good correspondence between model and experimental results at low $\alpha$ angles, deviation starts at $110^\circ$ for $\phi = 5^\circ$ , $\theta = 9^\circ$ , $120^\circ$ for $\phi = 10^\circ$ , $\theta = 4^\circ$ . Experimental data show largest positive strain at high $\alpha$ angles . . . . .	78
4.17	Second principal strain at rosette gauge point $R_2$ . Good correspondence between model and experimental results for both $\phi - \theta$ configurations. Experimental data show largest negative strain at low $\alpha$ angles. . . . .	79
4.18	Strain at single gauge point $S_1$ . The agreement between model and experimental results is visibly poor. Experimental data show highest negative strains at low $\alpha$ angles, and highest positive strains at high $\alpha$ . . . . .	79

4.19	Strain at single gauge point $S_2$ . As with the results from the $S_1$ gauge, the agreement between model and experimental results is poor. Experimental data show highest positive strains at low $\alpha$ angles, and switches to negative once $\alpha$ exceeds $100^\circ$ ( $\phi = 10^\circ, \theta = 4^\circ$ ) and $110^\circ$ ( $\phi = 5^\circ, \theta = 9^\circ$ ) . . . . .	80
4.20	Angle between first component of strain gauge and first principal strain, calculated from experimental and model results. There is deviation between data sets than is the case for the strain/load data, suggesting that difference between the model and the experiment have little effect on the direction of the principal strains. . . . .	82
5.1	The two load cell attachments used in the experiments with the sheep's femur: machined from perspex (left) and PTFE (right). The PTFE attachment was machined from a cylinder, the full $100 \times 65$ mm base could not be included. It has a large enough base to accommodate the four drill holes, so this does not compromise the structure.	88
5.2	Two greater trochanter protectors. Left: PMMA, right: foam. . . . .	89
5.3	Left: perspex attachment and PMMA cap. Right: PTFE attachment and foam. . . . .	90
5.4	a) Sample strain vs. time plot taken with foam greater trochanter protector. b) Load vs. time with foam protector. c) Comparison of load vs. vertical displacement of the load cell (measured by control software) for the different greater trochanter protectors. . . . .	92
5.5	Alignment of femur and load cell attachment with respect to coordinate axes. Highlighted boundaries in left image show fixed boundaries.	94
5.6	Load cell attachment is rotated about $z$ axis, stress perpendicular to top surface is integrated across plane. . . . .	96
5.7	Location of reference points used in trilateration (marked red) and the calculated gauge points (blue). . . . .	97
5.8	First principal strain measured experimentally and calculated with the finite element model at rosette gauge point $R_1$ . The simulated strain is considerably greater than the experimental strains for $\alpha < 120^\circ$ .	98

5.9	Second principal strain measured experimentally and calculated with the finite element model at rosette gauge point $R_1$ . The model results are closer to the experimental data than was the case for the first principal strain. . . . .	98
5.10	First principal strain measured experimentally and calculated with the finite element model at rosette gauge point $R_2$ . The strains calculated with the model are considerably larger than the experimental data. This is particularly visible at the high and low extremes of $\alpha$ . . . . .	99
5.11	Second principal strain measured experimentally and calculated with the finite element model at rosette gauge point $R_2$ . The simulated strains are again much larger than the experimental data, particularly at the high and low extremes of $\alpha$ . . . . .	99
5.12	Experimental strain and strain calculated with the finite element model at single gauge point $S_1$ . Simulated strains are typically significantly larger than the experimental strains, and feature a large change in strain from positive to negative between $\alpha = 60^\circ$ and $70^\circ$ . This is not seen in the experimental strains, which are exclusively negative. . . . .	100
5.13	Experimental strain and strain calculated with the finite element model at single gauge point $S_2$ . Simulated strains are significantly larger than experimental strains for $\alpha \leq 90^\circ$ . . . . .	100
5.14	Angle between first component of strain gauge and first principal strain, calculated from experimental and model results. As was the case for the results of the PVC study, there is less deviation between the data sets. This indicates that any differences between the model and the experiment have little effect on the direction of the principal strains. . . . .	101

5.15	First and second principal strains calculated from strains measured with rosette gauges, and strain measured with the single gauges. The largest strains measured at the first gauge point are positive, and measured at the lowest $\alpha$ angles. The strains measured at the second gauge point largest at the low (positive strain) and high (negative) extremes of $\alpha$ . The strain at the first single gauge point is largest at the lowest $\alpha$ angles, and is negative. The strain at the second single gauge point peaks at $\alpha = 90^\circ$ , and is negative. . . . .	105
5.16	Young's modulus plotted along a line through neck of femur, and plotted onto a plane. The "arc length" plotted on the $x$ -axis is the length of the line running from point a (the location of $R_2$ ) to point b.	106
5.17	First and second principal strain/load measured at each rosette gauge points, calculated from models using the original tetrahedral mesh and the mesh with a finer triangular surface mesh. Solutions were not found with the refined mesh for $\alpha = 50^\circ$ and $60^\circ$ . Largest deviations are seen where the change in strain as a function of $\alpha$ is largest, and at $\alpha = 130^\circ$ . . . . .	108
5.18	First and second principal strain measured at each rosette gauge point, as a function of the multiplication coefficient $A$ . Results of the finite element model are plotted (points), as are the power functions fit to the points (solid line), and the mean values of the principal strains measured in the experiment (dashed line). . . . .	110

# Chapter 1

## Introduction

Falls among older people are a common problem, with devastating consequences for many people. 3.4 million people in the UK over the age of 65 fall every year, incurring an estimated daily cost to the NHS of £4.6 million [1]. 65,000 of these falls result in hip fracture [2]. By simulating the process of hip fracture we can analyse it, and make steps towards determining the conditions that cause fracture and avoiding them. The aim of this project is to use a finite element model and experimental testing to simulate the loading conditions caused by a fall scenario, and investigate how changes to the loading conditions can affect the strains measured in the proximal femur. The results of the model and experiment will be compared against one another to assess the accuracy of the finite element simulation.

Human tissue samples are not available for use in this investigation due to time constraints. A polymer model of a human femur will be used as a surrogate femur sample for carrying out experimental tests to provide the geometry for a finite element model. Following this, the same process will be carried out with a sheep's femur. A sheep's femur was chosen as it is easily available and fairly comparable to a human femur in size and bone structure [3]. In spite of this, the sheep's femur does not have the same morphology as that of a human. Using the polymer human femur surrogate ensures that the apparatus and modelling techniques can be proved to be capable of being used for samples with the size and geometry of a human femur. This will allow for the development of experimental and computational techniques which could be applied to investigations using human tissue at a later time. The

effect of changing the orientation of the femur will be assessed in this thesis, with the inclusion of contact mechanics between the acetabulum and femoral head.

## 1.1 Falls and Hip Fracture

Hip fracture is associated with high mortality rates [4], and frequent consequences are loss of mobility, loss of independence, and increased fear of experiencing more falls in the future. The cost of treating hip fracture patients is significant, as is the cost of social care to the fallers, their families, and the state. The population over the age of 65 is predicted to rise over the next decade at a faster rate than other age groups [5], so the incidence rates of falls and hip fracture are very likely to also increase.

Falls are more frequent in older people due to a number of health problems, including poor balance, reduced muscle strength, and diseases affecting the bones and joints. The reflexive use of the hands to break the fall lessens the magnitude of the impact on more fragile parts of the body such as the hip. The slowing of reaction speed associated with ageing means that older people are less able to break their fall. Falls in older people are generally falls to the side, so the hip is the first point of contact with the ground. These factors mean that a fall often causes a large force in the hip joint.

A hip fracture is a fracture occurring in the proximal end of the femur, the portion of the femur near to the hip joint. Half of all fractures among older people affect the hip [6]. The likelihood of a fall resulting in a hip fracture is increased by the presence of osteoporosis, a disease causing fragility and reduced strength in bones. People who have suffered from hip fracture have been found to have, on average, less subcutaneous soft tissue protecting the hip joint than a healthy person [7]. This tissue provides protection to the hip joint and reduces the force of the impact delivered to the joint.

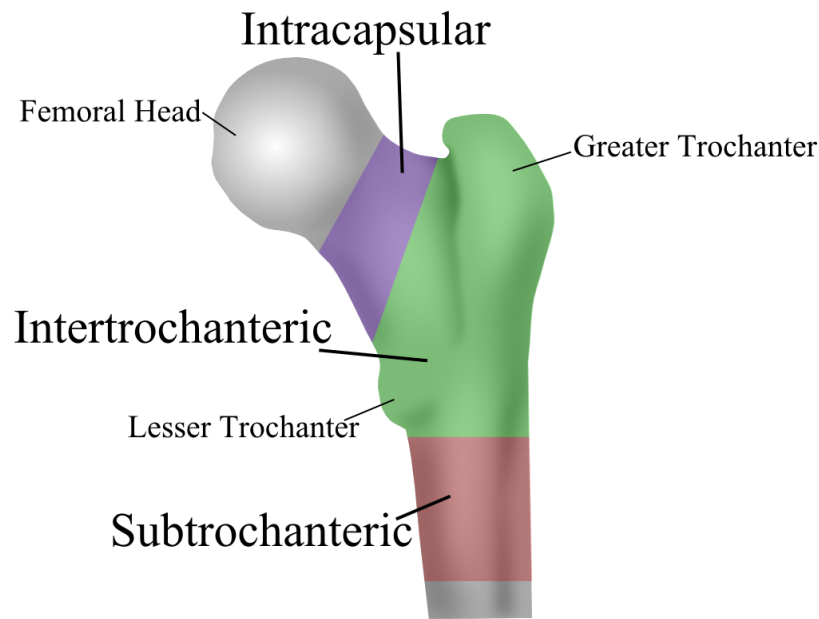


Figure 1.1: Categorisation of hip fractures based on the region of the femur where they occur.

Figure 1.1 shows how hip fractures are categorised by their location on the femur. The location of the fracture can have a great effect on the severity of the injury and the recovery of the patient. Intracapsular fractures, which occur on the part of the femur which lies inside the hip joint, can disrupt the blood supply to the femur, which can cause tissue death and delay healing [6]. Intertrochanteric fractures occur between the greater trochanter and the lesser trochanter, two bony protrusions whose location are seen in figure 1.1. Subtrochanteric fractures occur in the 5 cm portion of the shaft of the femur below the lesser trochanter. 54% of all hip fractures are intracapsular, 35% intertrochanteric, and 6% subtrochanteric [8].

The likelihood of a fall leading to hip fracture can be reduced by reducing the force transmitted to the hip joint. This can be done by placing a barrier between the faller and the surface onto which they fall, or by modifying the surface. Hip protectors are devices worn over the hip to absorb energy and transfer the energy from the bone to the surrounding soft tissue in the case of a fall. Hip protectors reduce the magnitude of the force delivered to the femur in a fall [9], and they have been proven to reduce the likelihood of hip fracture [10]. The effectiveness of hip protectors depends upon the user's agreement to wear them at all times, uptake has been found to vary from 37% to 72%, and compliance between 20% and 92% [11].

Changes to floor surfaces may have the potential to reduce injury rates. There is some evidence that carpeted floors are associated with fewer fall injuries than vinyl floors [12].

## 1.2 Finite Element Modelling and Experimental Investigation of Hip Fracture - A General Review

The finite element method is a numerical analysis technique which is widely used in many areas of physics and engineering. It can be used to approximate the solution to any problem characterised by a boundary value problem. It is particularly useful for systems with complicated geometries, where it is impossible to derive a continuous solution for the entire system. Instead, the structure is split into a mesh of small elements in which it is possible to solve the equation. The finite element method has been used frequently in simulations of the proximal femur, where it is used as a non-invasive way of measuring strain and simulating fracture mechanics [13–23].

The benefit of using a simulation is that mechanics of the problem can be calculated at any point on the surface or within the volume of the femur. The structural complexity of the femur, along with the complicated microstructure and variable material properties within the bone, mean that the reliability of a finite element model cannot be assumed automatically. Data gathered from the model can be compared against strains measured in an analogous experiment to verify whether the model is providing an adequate simulation of the mechanics of the problem.

Finite element modelling was first used to characterise the mechanical response of femurs to loading by Brekelmans et al. in 1972 [24]. The finite element method requires the user to define the geometry of the simulated object. Brekelmans study was carried out with a 2D geometry based on radiography images. Some 3D studies

have been done using geometry built by computed aided design [25]. The use of computed tomography scans to characterise the geometry of the femur in 3D was introduced by Basu et al in 1986 [26].

Quantitative micro X-ray computed tomography (CT) is a technique frequently used to create three-dimensional surface geometry images of the proximal femur [15, 20], as well as provide a measurement of the material properties of the bone [13, 18, 19, 27]. The finite element software also requires the user to input the material properties of the objects. In the case of the structural mechanics problem, the relevant material properties are the Young's modulus and Poisson's ratio. Studies have confirmed a correlation between CT attenuation coefficients and the material properties of bone [28–30].

A bone density imaging phantom, such as the potassium phosphate liquid phantom developed by Cann and Genant [31], can be scanned alongside the bone sample to calculate its ash density. The phantom consists of a number of solutions of varying concentrations, and so the linear attenuation of the phantom samples can be used to calibrate the equivalent potassium phosphate concentration within the bone sample, from which it is possible to determine the ash density of the bone [32]. Mathematical relationships between the ash density and the material properties of bone have been determined by a number of studies [17, 18, 33].

The forces involved in a fall are caused by an impact, meaning that the structural mechanical problem is time-dependent. All of the finite element analyses of hip fracture mechanics discussed in this chapter are static or quasi-static. The models and experiments designed in this project will only involve static loading. The mechanical problem of dynamic impact is significantly more complex to solve than static loading. Although the solution to the dynamic problem cannot be accurately solved by a static simulation, the aim of this process is to estimate the effect of altering the loading conditions on the scale and distribution of the strain induced in the bone. Several experimental investigations have been carried out into falls. These studies generally used a pendulum [9, 34–36], or drop test [37, 38] to apply

the impact load. Many of these tests were done to assess the forces associated with falling, particularly the effect of hip protectors in damping the impact of the fall [9, 36–38]. Synthetic materials have been used in dynamic testing experiments to simulate the soft tissue covering the hip joint [34–38]. Surrogate femurs are often used in place of real bone samples. They are designed to mimic the shape of the femur, and have been constructed out of materials such as wood [36], steel [38], or polymers [34, 35, 37]. This would not provide a good estimate of strains induced in a real human femur, but is adequate for measuring applied force using a load cell [34–38]. The advantage of using a surrogate femur as opposed to a bone sample is that it can be constructed from a material which does not decay. The surrogate can be designed to have homogeneous material properties which are easier to define than those of bone, and there is the potential to make it more resilient than real bone. This means that techniques can be tested out and refined without worrying about damaging a real bone sample, and that it is easier to compare the results of the experiment and model because the sources of error associated with estimating the material properties of bone tissue are not included. Full-scale polymer models of human bones, designed for educational use, are readily available.

A direct way of assessing hip fracture mechanics using finite element modelling is to use a failure criterion to indicate whether a fracture would occur under the simulated conditions. The initiation and propagation of fractures has been found to be highly dependent on the distribution of the microstructural constituents of the bone [39, 40]. One way of testing whether failure has occurred in each element of the model by comparing the stress induced with the strength of the material in that element [18]. This technique can be used to predict the minimum forces required to cause fracture. Other studies compare the strain simulated in the model with strains induced in experimental testing measured by strain gauges bonded to the surface of the bone under the same loading conditions [14, 20, 22]. This allows for comparison of results with small forces, and does not rely on the reliability of any fracture criteria. Experimental testing of bone samples can be performed with much smaller loads than would be present in a real fall, ensuring that the sample is not damaged and can be used for further studies.

Some studies have been carried out to investigate how the way in which a person falls affects the forces induced in the hip and the likelihood of hip fracture. Groen et al. showed that the force of impact depends on falling technique, such as blocking with the hands and arms [41], and Lo and Ashton-Miller studied pre-impact movement strategies [42]. These studies show that how the body is positioned at time of impact has an effect on the force transmitted to the hip.

Keyak, Skinner and Fleming used a finite element model derived from CT data to quantify the effect of force direction on fracture load in both fall and stance configurations [23]. They varied the force directions three-dimensionally by applying a load to the head of the femur, and quantifying angles of rotation of loading direction about shaft and away from the shaft. They found that the lowest fracture loads correspond to falls onto posterolateral aspect of greater trochanter. In an earlier paper, Keyak experimentally compared the static forces required to cause fracture in femurs in the stance position and in a fall position [16]. They found that the fracture loads in the two configurations are linearly related, but correlation is not good enough to reliably predict one from another.

Wakao et al. used a finite element model derived from CT data of healthy people, people who have suffered hip fracture, and people who have osteoporosis but have not suffered fractures to investigate the effect of the angle of the loading direction by rotating the femur about the shaft and applying forces to the appropriate boundaries according to rotation angle [21]. They found a significant relationship between loading direction and fracture load, and that the effect of altering the direction was larger in models derived from scans of fracture patients obtained from the intact (contralateral) femur and people with osteoporosis than in healthy people. They also found that the fracture load was lowest in falls onto the posterior aspect of the femur.

Bessho et al. used a finite element model created with CT scans of the contralateral femurs of people who have suffered from hip fracture to assess the load

required to cause fracture as well as the location of the fracture [13]. The findings of the models were compared with the real fractures. They compared a stance configuration with four fall configurations and used a fracture criterion to assess the minimum load necessary to cause fracture under each loading condition. Like Keyak et al. and Wakao et al., they found that the smallest fracture loads were associated with a fall onto posterolateral aspect of the femur.

It is clear from the results of the above mentioned papers that the loading direction has a significant effect on the strains induced in the femur and the forces required to cause fractures. A factor which has not been included in any of these studies, however, is the way in which the femoral head interacts with the acetabulum, the concave surface of the pelvis in which the femoral head sits to form the hip joint. The contacting faces of these two objects are not perfectly smooth or spherical, so the size of the force delivered through the pelvis to the femur, as well as the size of the contact area and its position on the femoral head, will depend on the contact mechanics between the two surfaces under the given loading configuration.

### 1.3 The Structure of This Thesis

The purpose of the work presented in this thesis is to develop the techniques necessary to create a valid simulation for human bone, and to analyse the effect of changing the orientation of the femur on the strain distribution and intensity. The aim is to simulate separately the shape of the femur (using a PVC femur model), and the distribution of Young's modulus within a bone sample (with a sheep femur).

A finite element model will be created to simulate strain in the femur under different loading angles. The results of this model will be verified by carrying out an analogous experiment on a femoral sheep bone sample, and comparing strains measured with strain gauges.

Thesis structure:

- Chapter 2 will deal with developing techniques for creating the finite element model. Techniques for using CT scan data to derive geometry and material properties will be tested and used to create simple models of the PVC femur and sheep's femur without contact mechanics to assess how changing direction load affects strain distribution. This will be useful in the design of the experiments.
- Chapter 3 will include an assessment of experimental techniques used for bonding gauges to bone samples and fixture of samples within apparatus. The effect of freezing and thawing the sample multiple times will be tested.
- Chapter 4 will describe the design of the experimental apparatus, which will be used to test the effect of loading orientation on the strain measured on the surface of the PVC femur. The results of the experiment will be used to test the validity of a finite element model which will be based on the polymer preliminary model described in chapter 2, with the addition of contact mechanics and designed to mimic the conditions of the experiment.
- Chapter 5 will report on an experiment where the apparatus described in chapter 4 is used to test the sheep femur. The experimental techniques will be refined based on the outcomes of the previous chapter. A finite element model of the sheep's femur will be created, with contact mechanics, and results of the model and the experiment will be compared.
- Chapter 6 will consist of a conclusion, summarising the findings of the project and considering potential future developments of this work.

## Chapter 2

# CT Characterisation of Femoral Bone and Finite Element Modelling of Bone Tissue

### 2.1 Introduction

In order to build a reliable finite element model of the proximal femur, the morphology and the material properties must first be characterised.

The proximal portion of the femur can be thought of as a combination of two types of osseous tissue: cortical bone and cancellous bone. Cortical bone is a hard, dense tissue which forms a shell on the outside of the bone. Cancellous bone is a porous tissue consisting of a framework of trabeculae, hard rod-like structures which grow in alignment with the typical load direction that the bone is subjected to [43, 44].

Finite element modelling software requires the user to input the material properties of any objects being modelled, in the case of structural mechanics modelling this is the Young's modulus and Poisson's ratio. These properties are not uniform throughout the structure of a femur. There are many complex microstructures throughout the structure of the bone which cause inhomogeneous response to stress. The most reliable way to characterise the geometry and material properties of the

tissue is to use X-ray computed tomography. The purpose of the work presented in section 2.2 is to use this technique to create a geometry file for each of the samples used in this study, as well as a spatially varying function for the Young's modulus of the sheep bone sample, which can be imported into the finite element software.

The geometry of a PVC femur determined in section 2.2 was used to create a simple finite element model which simulates the effect of changing the loading direction on the strain distribution. It was used to determine the locations on the surface of the femur which experience the largest strains. Two models of a sheep's femur were also created, one with a spatially varying Young's modulus function through the volume of the bone, the other with a constant modulus throughout. This was done to investigate the effect of the spatially dependent Young's modulus on the strains induced in the femur. These models also simulated loading under different loading angles. All finite element analysis performed in this project was carried out in COMSOL Multiphysics. This information will be useful when designing the experiment in later chapters.

## 2.2 Modelling bone tissue

### 2.2.1 Computed Tomography

Quantitative micro X-ray computed tomography (CT) is a technique frequently used in the development of finite element models of biological materials. CT has been widely used to create three-dimensional surface geometry images of the proximal femur bone structure [15,20], and it has also been used to provide a measurement of the material properties of the bone [13,18,19,27].

#### 2.2.1.1 Geometry

A micro CT scan provides a measure of the average linear attenuation coefficient of X-rays within each voxel of the image. Micro CT scanners provide the absolute linear attenuation coefficient (SI units  $\text{m}^{-1}$ ), unlike medical CT scanners which use

the Hounsfield scale. Assuming that the linear attenuation of the sample differs sufficiently from that of the surrounding air, a three-dimensional surface can be formed by using a threshold linear attenuation value to split the space in the scanned volume into that which lies above the threshold (within the object) and that which lies below (the air surrounding the object). This information is imported into finite element analysis software to define the geometry of the object.

A CT scan was used to provide an STL mesh geometry file compatible with Comsol of a right PVC femur model (3B Scientific LTD., Weston-super-Mare, United Kingdom). The femur, a full size human simulant, was approximately 40 cm long. The scanner (Nikon Metrology XT H 225) has a scanning platform with a diameter of approximately 170 mm, so a handsaw was used to cut the femur to approximately this length. Hip fractures occur in the proximal part of the femur, so it is not important that the distal part of the geometry is present in mechanical tests. Many studies, involving both finite element modelling and experimental testing, have used just the proximal portion of the femur [14, 16, 20–22].

The femur CT scan was obtained (105 kVp, 295 mAs, 0.0991 mm voxel size,  $1879 \times 1064$  pixel slice area, 780 slices), and the data was processed in VGStudio MAX (version 2.1). The surface was exported in an STL mesh file with 25,000,000 vertices. The STL file exported by VGStudio MAX was too large to be processed by Comsol, so the number of vertices in the mesh had to be reduced in Meshlab v1.3.0b to 2800 vertices. Images of the PVC mesh are shown in figure 2.1. The reduced STL file was imported into Comsol, where the triangular framework formed by the mesh was automatically partitioned into faces. The import settings were altered manually to ensure that the face partitioning appeared realistic and there were no gaps in the surface of the geometry.

### 2.2.1.2 Material Properties

As noted in section 2.1, the bone tissue of the proximal femur is a complicated, inhomogeneous material consisting of many small microstructures. While it is ac-

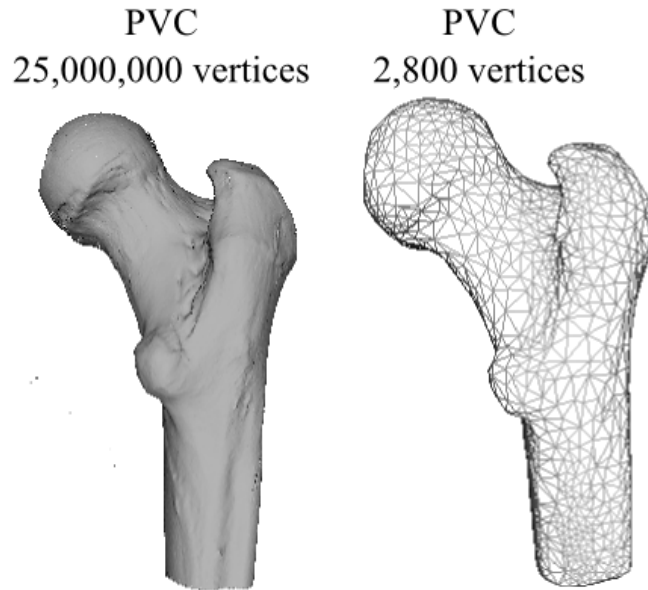


Figure 2.1: Images of both the PVC femur meshes before and after reduction.

ceptable to apply constant mechanical properties to the PVC femur model, the properties of bone are better defined by a spatially dependent function. Instead of modelling the microstructure of the bone, which would require an impractically fine mesh, the material properties are averaged across small unit volumes across the geometry of the bone [14, 18–22].

The Young's modulus of bone can be determined from the ash density [13, 17–22, 32, 33, 45]. The ash density is calculated by scanning alongside a CT bone density phantom, an object designed to have a similar X-ray opacity to bone, and consisting of a number of objects with known equivalent bone ash densities. When the phantom is scanned alongside a sample, a calibration equation can be determined in order to calculate bone ash density from the linear attenuation within each voxel.

A number of different materials have been used to make bone density phantoms. Solid hydroxyapatite phantoms are commercially available, and are frequently used to measure bone density for femoral hip fracture finite element analysis [13, 19, 21]. Another commonly used phantom is potassium phosphate ( $K_2HPO_4$ ), dissolved into distilled water at different concentrations to provide a varying mineral density [17, 18, 33, 45].  $K_2HPO_4$  is a good choice because it is inexpensive and easy to make, and has been shown to be as effective as a commercial phantom [32]. A

$K_2HPO_4$  phantom was chosen for this project for these reasons.

Nazarian et al. [32] provided an equation for calculating ash density from the equivalent  $K_2HPO_4$  concentration of bone,  $C$ ,

$$\rho_{\text{ash}} = 1.48C - 0.8. \quad (2.1)$$

All densities and concentrations are expressed in  $\text{g cm}^{-3}$ .

In order to characterise the Young's modulus of bone samples, Keyak et al. (1998) [18] used two separate equations (determined by Keller [33] and Keyak et al. (1994) [17]) which predict the modulus each for a different range of ash density. Keller's study provides an equation for cortical bone samples with an ash density of  $\rho_{\text{ash}} \geq 0.6 \text{ g cm}^{-3}$ ,

$$E_{\text{cort}} = 10.2\rho_{\text{ash}}^{2.01} \quad \text{if} \quad \rho_{\text{ash}} \geq 0.6 \text{ g cm}^{-3}. \quad (2.2)$$

All moduli are expressed in GPa. Keyak et al. (1994) provide an equation for cancellous bone samples with an ash density of  $\rho_{\text{ash}} \leq 0.27 \text{ g cm}^{-3}$ . Separate equations were provided for the elastic modulus of cancellous bone along the superior-inferior, mediolateral, and anteroposterior directions, as this property varies with loading direction depending on the direction of growth of the trabeculae. As hip fractures are primarily caused by sideways falls, the femur was primarily loaded along the mediolateral axis, and the appropriate relationship was used,

$$E_{\text{canc}} = 7.330\rho_{\text{ash}}^{2.07} \quad \text{if} \quad \rho_{\text{ash}} \leq 0.27 \text{ g cm}^{-3}. \quad (2.3)$$

Keyak et al. (1998) used a model combining these two relationships, along with a linear interpolation applied to ash densities between  $0.27 \text{ g cm}^{-3}$  and  $0.6 \text{ g cm}^{-3}$ . Keyak et al. (1998) used the equation for the superior-inferior direction, so the same method was used here but incorporating the mediolateral equation instead, as this

is the principal direction along which the bone was loaded.

$$E_{int} = 9.59\rho_{ash} - 2.10 \quad \text{if} \quad 0.27 \leq \rho_{ash} \leq 0.6 \text{ g cm}^{-3}. \quad (2.4)$$

A Poisson's ratio of 0.4 is assumed for all ash densities [18].

## 2.2.2 Densitometry of sheep femur

Nazarian et al. [32] used four concentrations of  $\text{K}_2\text{HPO}_4$  solution: 0.05 g/ml, 0.15 g/ml, 0.5 g/ml, and 1 g/ml. The same concentrations were chosen here, but with the addition of a pure distilled water sample ( $C = 0$  g/ml).  $\text{K}_2\text{HPO}_4$  (Sigma-Aldrich, Gillingham, United Kingdom) calibrations were prepared by serial dilution with distilled water in plastic bottles. The solutions were transferred to plastic 0.25 ml microcentrifuge tubes (Alpha Laboratories, Eastleigh, United Kingdom).

A left sheep femur was acquired from a local butcher (Joseph Morris, Wigston, United Kingdom). The distal part of the femur was removed with a handsaw approximately 140 mm from the head to the sawn end. The femur was acquired with most of the muscle tissue removed, and as much as possible of the remaining soft tissue was removed from the surface of the bone with a number 10 scalpel blade. The femur was scanned and the data was processed in VGstudio (110 kVp, 326 mAs, 0.0892 mm voxel size,  $1006 \times 1033 \times 1470$  volume). The femur was placed in a plastic flowerpot and supported with pieces of foam so that it could be held vertically in the scanner. The foam had a very low linear attenuation so did not appear in the scan data. The five calibration phantom vials were pressed into the foam along the axis of the bone. The flowerpot and the calibration vials did not touch the femur directly, so they could be easily removed from the STL file.

Figure 2.2 illustrates the process undertaken to generate a surface mesh and spatially varying Young's modulus function within the finite element model using the scan data. An STL file containing the mesh of the surface geometry of the femur (186,582 vertices) was exported and reduced in Meshlab (2000 vertices). Figure 2.3

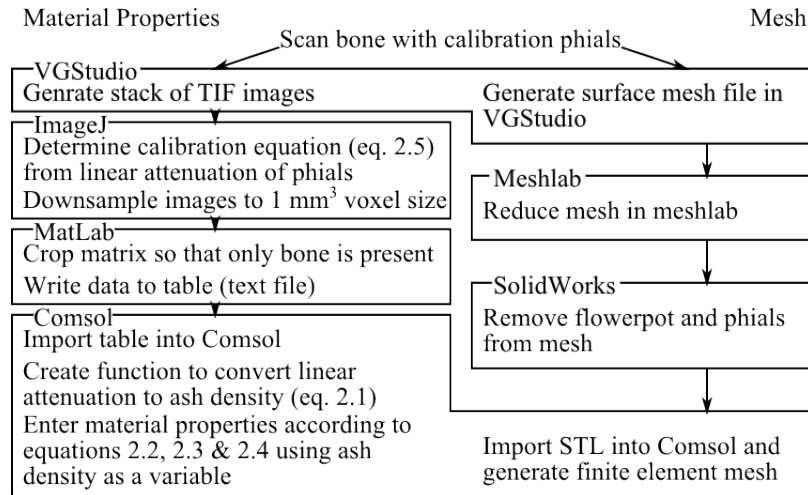


Figure 2.2: The process of generating a mesh and spatially varying Young’s modulus function within the finite element model. The left hand column shows the process used to import the linear attenuation data obtained during the scan, calibrate it to determine ash density, then calculate the Young’s modulus. The right hand column shows the process used to generate the surface mesh for the femur.

shows the original mesh including parts of the flowerpot and calibration vials. These were removed from the mesh in Solidworks after the mesh was reduced. The CT data was also exported from VGStudio MAX as a stack of TIF image files, with each image representing one voxel layer in the  $z$ -direction. The grey value of each pixel scales linearly with the linear attenuation in the corresponding voxel. All TIF image analysis and manipulation was carried out in ImageJ 1.48v. The extent of the  $K_2HPO_4$  solution in the calibration vials in the  $z$ -direction was determined to range from 184 to 248 slices. For each vial, image slices were taken at five 50 slice intervals, covering 180 slices starting from the approximately lower extent of the vial, and linear attenuation values were sampled from a manually selected rectangle. An example of a sample rectangle from the 1 g/ml phantom vial is shown in figure 2.4. The sampling areas were taken from the centre of the cross section of the vial, and care was taken to avoid artificial lowering of the measurement due to partial volume effects caused by inclusion of any voxels containing plastic or air. The mean and standard deviation of the grouped data from each of the five slices are plotted in figure 2.5 against the equivalent  $K_2HPO_4$  concentration.

The calibration equation for calculating equivalent  $K_2HPO_4$  concentration  $C$  for a given linear attenuation  $\mu$  was determined by generating a line of best fit of the

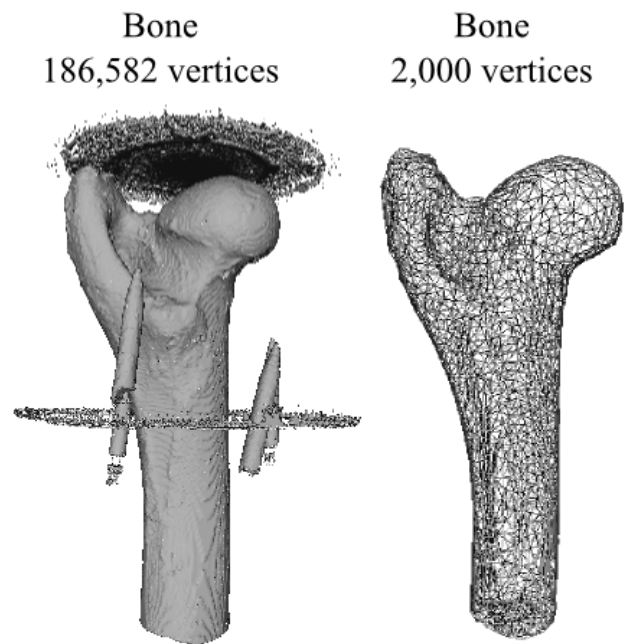


Figure 2.3: Images of the sheep bone meshes before and after reduction. Parts of the plastic pot and calibration vials were present in the original file (visible in the left-hand image) and removed after reduction.

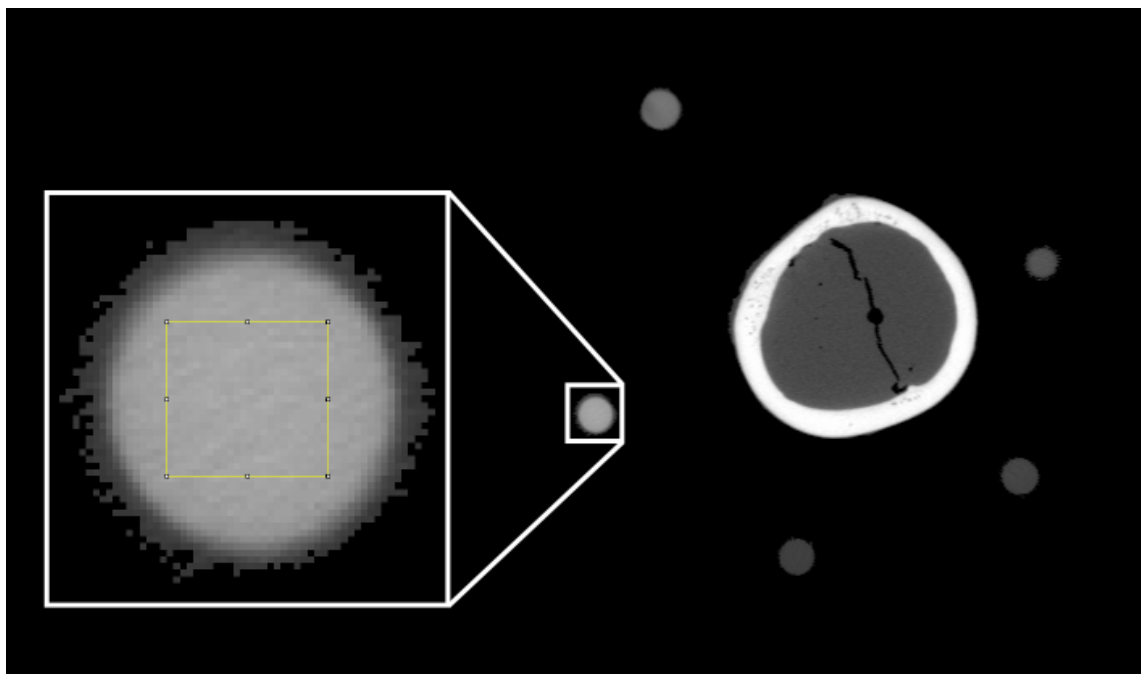


Figure 2.4: Sample slice (slice number 687) taken from scan of sheep femur and  $K_2HPO_4$  calibration vials. All five vials are visible, along with a cross-section through the shaft of the femur. Expanded image shows  $C = 1$  g/ml phantom vial. Pixels within the yellow box (24 by 23 pixels) were sampled along with data from 4 other slices to generate a mean and standard deviation for the linear attenuation of the contents of this vial.

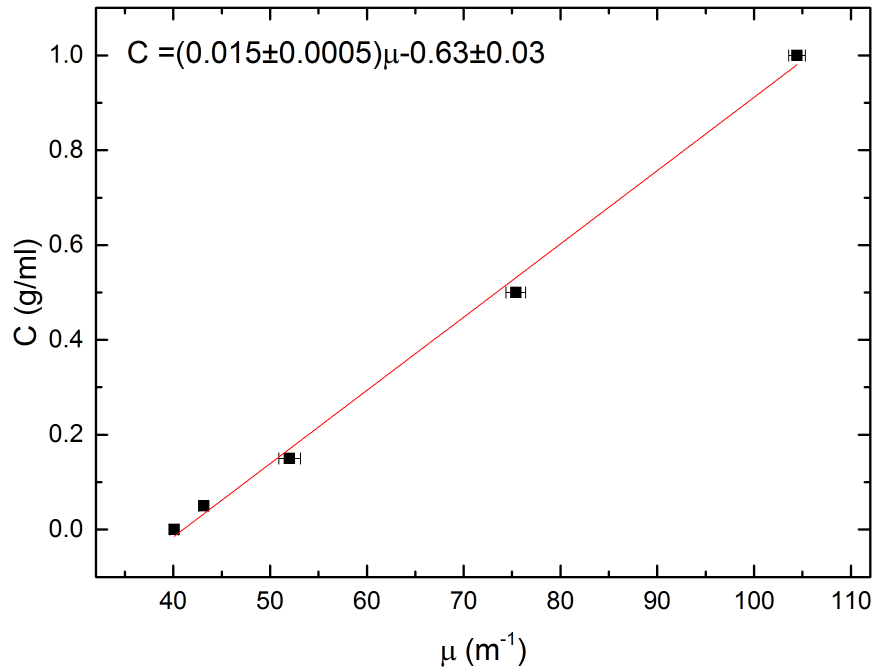


Figure 2.5: Calibration graph of  $\text{K}_2\text{HPO}_4$  concentration  $C$  plotted against mean linear attenuation  $\mu$  in each of the five phantom tubes. Error bars are the standard deviation in  $\mu$  for the samples taken from each vial.

data (using graphing software Origin (OriginLab, Northampton, MA, USA)):

$$C = 0.0155\mu - 0.63. \quad (2.5)$$

The images were downsampled using ImageJ's bilinear interpolation tool so that each voxel contained the mean linear attenuation in  $1 \text{ mm}^3$ , and the stack was saved in an Analyse format. A MatLab program was written to read the Analyse image and save its contents into a text file containing a four-column table of coordinates and linear attenuation values. Comsol's interpolation function allows the user to enter values at discrete points on a three-dimensional grid, and interpolates the values across the whole geometry. Linear attenuation values were entered at 1 mm intervals across the volume of the geometry of the femur. A function was created to convert linear attenuation values to ash density, using equations 2.5 and 2.1. The interpolated concentration function was then used in equations 2.2, 2.3, and 2.4 to compute the Young's modulus. Figure 2.6 shows a sample image from the scan before and after downsampling, along with the Young's modulus calculated in Comsol

on the same plane.

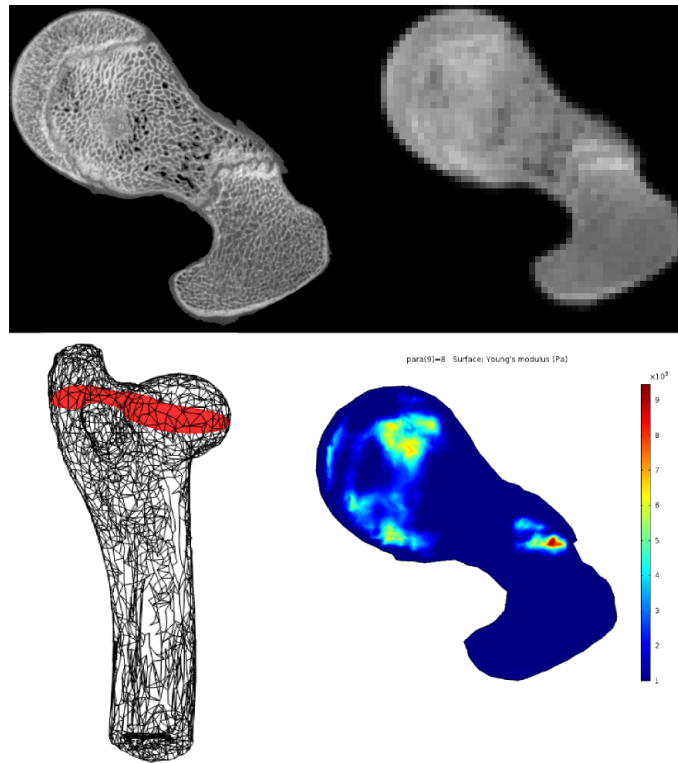


Figure 2.6: Clockwise, from top left: a sample image slice; the same slice after downsampling; the elastic modulus (GPa) plotted on a cut plane at the same z value as the image slices; the location of the cutplane in the geometry of the proximal femur geometry.

## 2.3 Preliminary Finite Element Model - PVC

Throughout this project, the surface strains calculated by finite element analysis was compared with strains measured with strain gauges bonded to the surface of a femur. The number of points where strain can be measured is therefore restricted by the number of available strain gauge amplifier channels. It is important to select points on the surface of the femur which experience a significant strain dependence on loading condition. The positioning of the gauges is constrained by the surface geometry, the surface that the gauge is bonded to needs to be sufficiently flat and smooth, as surface defects could cause unpredictable localised strain concentration. It is therefore critical to understand the strain distribution on the surface of the femur so that the areas with the largest strain can be predicted. It is also important to select a range of loading conditions which result in a significantly varying strain

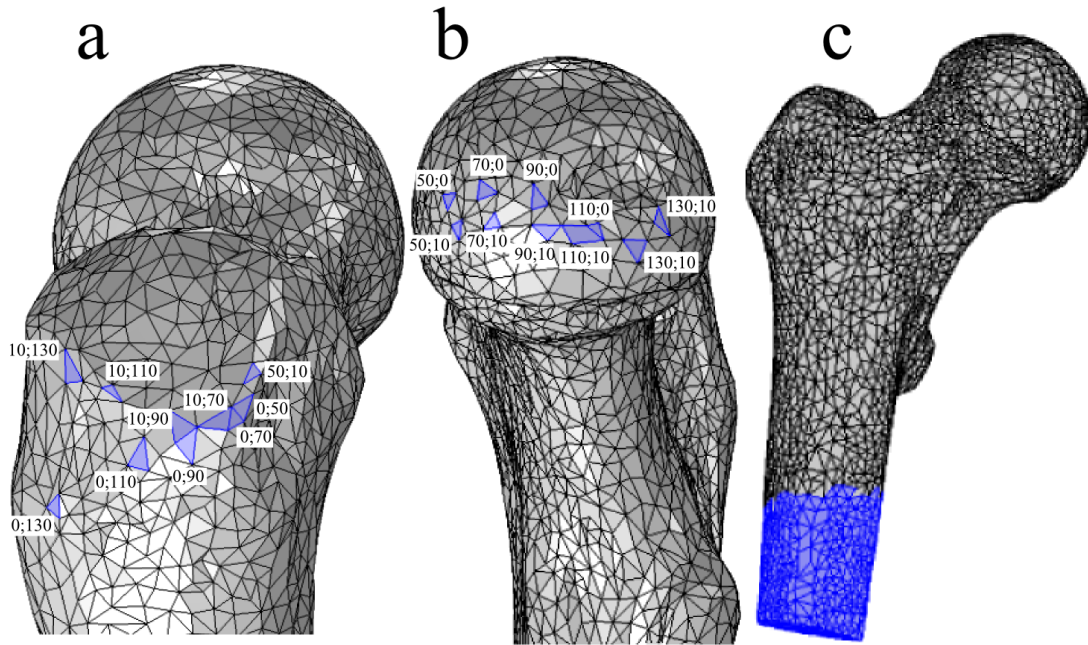


Figure 2.7: Position on the PVC femur of a) boundary loads and b) fixed boundaries for each loading condition. c) the fixed boundaries for all loading conditions at the distal end of the femur

distributions.

A finite element simulation was run to observe how loading angle affects strain distribution. In chapter 1, it was stated that the loading conditions will be changed by altering orientation of the femur, thus changing the the point of contact with the load cell and the floor. While the aim of this project is to produce a model where the load applied to the femur is governed by simulation of contact forces, the simulation reported in this chapter is a preliminary model which does not require this level of complexity or accuracy. Normal loads will be applied through small, single facet boundaries. The purpose of this simulation is to provide a qualitative assessment of the strain distribution on the proximal femoral geometry.

### 2.3.1 Model

The STL file of the PVC proximal femur portion was imported into Comsol. The material properties of PVC were applied ( $E = 2.7 \text{ G Nm}^{-2}$  [46], and the Poisson ratio  $\nu = 0.4$  [47, p.278]). All boundaries at the distal end up to approximately 3 cm from the sawn end were fixed in space (figure 2.7c). Bone cement is used in the

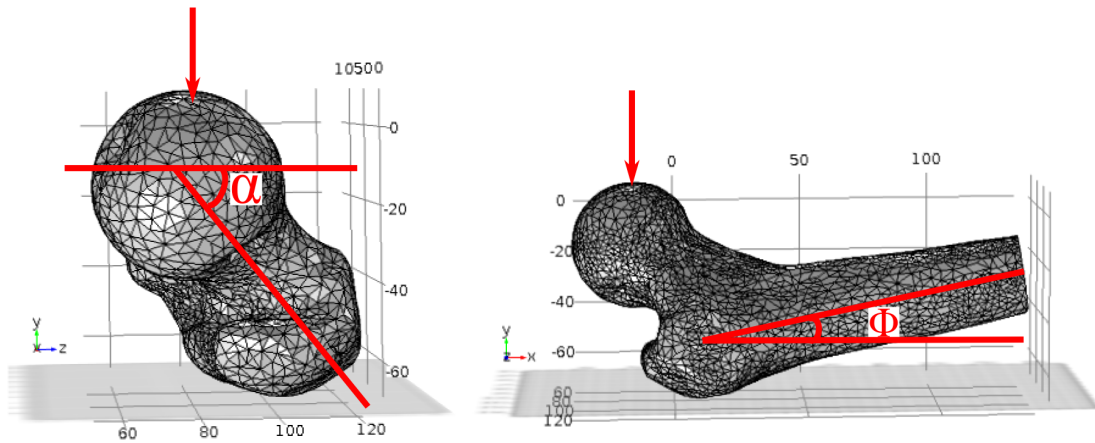


Figure 2.8: Loading configuration of model depends on two angles:  $\alpha$  - the angle of rotation about the shaft, and  $\phi$  - the angle between the shaft and the floor. The point and direction of the applied 1 N load is shown with an arrow, and the floor is represented by a workplane.

experiments described in this thesis to hold the distal end of the PVC and bone samples in the apparatus. The decision was made to not model the displacement of the boundaries in contact with the cement, as they were considered to be at a sufficient distance from the proximal end of the loaded boundaries, and the proximal end of the femur where hip fractures frequently occur.

The geometry was rotated so that the bone shaft (proximal-distal axis) pointed roughly along  $x$ -axis of Comsol's coordinate system, and the medial-lateral axis pointed along the  $y$ -axis. This was done by plotting a line through the anatomical axis in the Comsol geometry using the coordinates of two nodes estimated to be at either extent of this axis on the surface of the femur, and calculating the angles between this line and each Cartesian axis. The load was applied roughly along the  $y$ -axis, this was achieved by using two workplanes in the  $x - z$  plane and selecting the positions on the  $y$ -axis to bring them in to contact with the femur. The first boundary met by the workplane was selected as the boundary of application of the load (boundaries on the femoral head) or the fixed boundary (greater trochanter).

Two rotations of  $\alpha$  and  $\phi$  were applied around the  $x$ - and  $y$ -axes respectively (Figure 2.8). The angles were set so that  $\alpha = 90^\circ$  and  $\phi = 0^\circ$  described the configuration described in the previous paragraph, representing an exclusively sideways fall with the femur parallel to the ground.  $\alpha < 90^\circ$  represents the case where the impact site

is rotated towards the posterior side of the greater trochanter, and when  $\alpha > 90^\circ$  the impact is rotated towards the anterior side. In configurations where  $\phi > 0^\circ$ , the femur is no longer parallel to the floor, representing a situation where the knee is turned away from the ground at the time of impact.

The position of the femur relative to the parallel workplanes could then be defined by the angles  $\alpha$  and  $\phi$ , and the workplanes moved along the  $y$ -axis to meet the femur and determine the loading and fixed boundaries for each loading condition. Ten loading conditions were used, five  $\alpha$  values and two  $\phi$  values (figure 2.7a and 2.7b).  $\alpha$  was varied from  $50^\circ$  to  $130^\circ$  with an interval of  $20^\circ$ . A study by Courtney [48] used an angle of  $10^\circ$  between the diaphysial axis and the ground, equivalent to the angle  $\phi$  in this study, based on loading conditions associated with producing realistic fractures [49]. This choice of angle has also been used by Wakao et al. [21] and Pinilla et al. [50]. The simulation was run at the range of  $\alpha$  angles with both  $\phi = 10^\circ$  and  $0^\circ$  degrees so that the effect of altering  $\phi$  can be observed.

The boundaries selected for loading were prescribed a normal compressive load of 1 N, this was achieved by applying a pressure equal to the inverse of the surface area of the load boundary. A sweep parameter was used to activate each loaded and fixed boundary pairing in turn, and a parametric solver was used to sweep through the 10 loading conditions.

### 2.3.2 Results

The principal strain with largest magnitude was plotted on the surface of the femur for each of the loading conditions (figure 2.9). This plot shows the largest strain regardless of its sign, but also shows whether the surface is extended (red) or compressed (blue).

Highly localised areas of high strain can be observed around the fixed and loaded boundaries. These local high strain concentrations are caused by small discrete loading areas, and are not seen in real hip fractures, as the bone is surrounded by soft

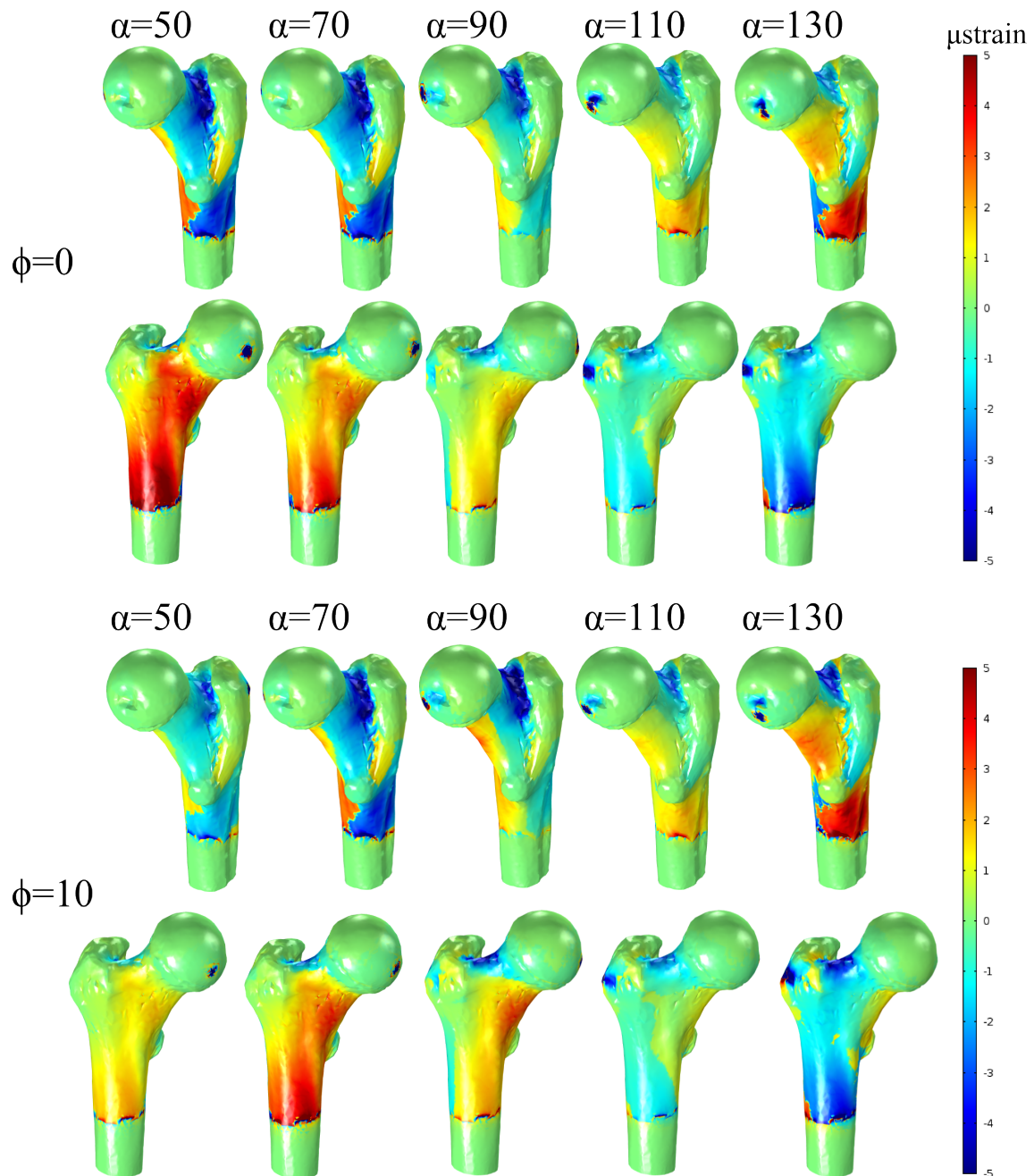


Figure 2.9: Maximum surface principal strain induced on the surface of the PVC femur under 1 N load for each combination of  $\alpha$  and  $\phi$ : posterior (top row) and anterior (bottom row) view. The range of strains mapped was limited to  $\pm 5 \mu\text{strain}$ .

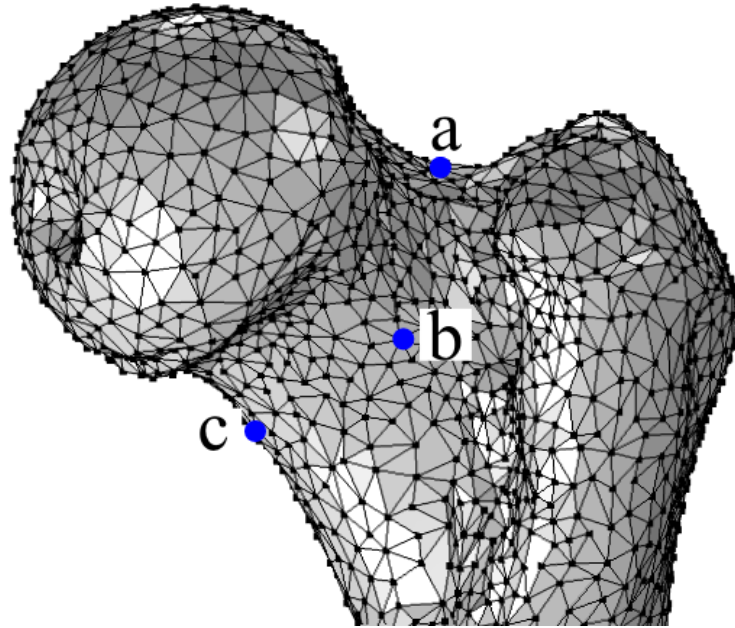


Figure 2.10: Location of the three sampled test points. Suitable locations were selected by observation of the strain distribution, and under the condition that the femoral surface must be relatively smooth.

tissue which reduces the pressure caused by impact. The force of the bodyweight passed to the femur in a fall is transferred through the acetabulum, which provides a large area over which to spread the force. Measures taken in experiments done with the bone sample to avoid the localised high pressure seen in this simulation will include the use of PMMA bone cement (see chapter 3), a plastic acetabular cup simulant (chapter 4), and foam soft tissue simulant (chapter 5). These will eventually be included in future finite element models. Highly strained areas are observed on the shaft immediately above the fixed boundaries. The proximity of this highly strained region to the fixed boundary indicates that these too are a result of an unnaturally rigid constraint on the distal end of the femur. The purpose of this model is to investigate strains in the proximal femur. The high strains caused by the fixed constraints at the distal end are not near the strained areas in the proximal part of the femur, indicating that the strain induced in the proximal femur is not sensitive to the boundary conditions at the distal end.

Highly strained areas are seen along the neck of the femur, most noticeably on the posterior side. The highest magnitude principal strains were sampled from three points on the neck, the superior (a), posterior (b), and inferior (c) sides (figure

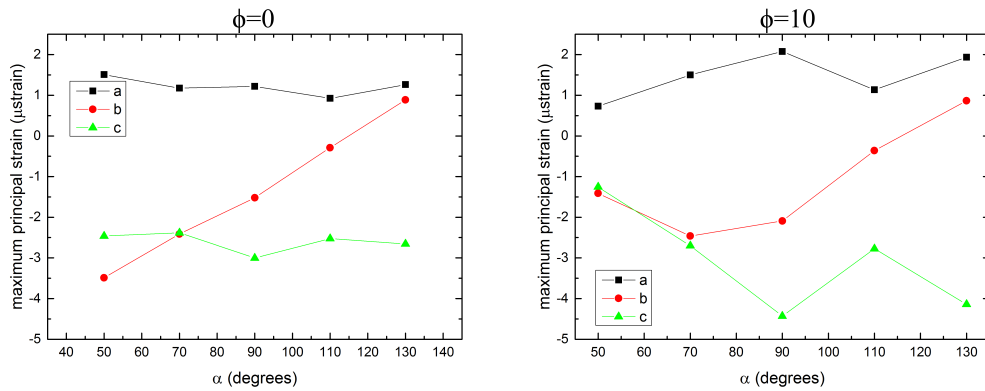


Figure 2.11: Maximum principal strain vs.  $\alpha$ : PVC model.

2.10). These points were selected in areas where the surface geometry was fairly flat, and it was feasible that a strain gauge could be applied here. The largest magnitude principal strain is plotted in figure 2.11. Point a is in compression for all loading conditions. Point b is in compression for lower values of  $\alpha$ , but crosses into extension between  $\alpha = 110^\circ$  and  $\alpha = 130^\circ$  (for both  $\phi = 0^\circ$  and  $\phi = 10^\circ$ ). Under all loading conditions, point c is in extension. Point b experiences the largest range in strain ( $4.3764 \mu\text{strain}$ ), followed by point a ( $3.1714 \mu\text{strain}$ ) then point c ( $1.3439 \mu\text{strain}$ ). Point a sees the largest strain ( $-4.4284 \mu\text{strain}$ ), followed by point b ( $-3.4874 \mu\text{strain}$ ) then point c ( $2.0764 \mu\text{strain}$ ).

## 2.4 Preliminary Finite Element Model - Bone

The morphology of the proximal femur of a sheep is quite different from that of a human. This, along with the spatially-varying Young's modulus of the bone sheep's bone sample, means that the dependence of strain distribution upon loading angle cannot be assumed to be identical in the PVC and sheep's bone samples.

A preliminary model investigation, similar to that of the PVC model described in the previous section, was carried out with the sheep's femur. This time, there is the additional complexity of the spatially dependent Young's modulus. Two models were created, one with a spatially dependent modulus function, the other homogeneous. The models were otherwise identical. The Young's modulus used for the

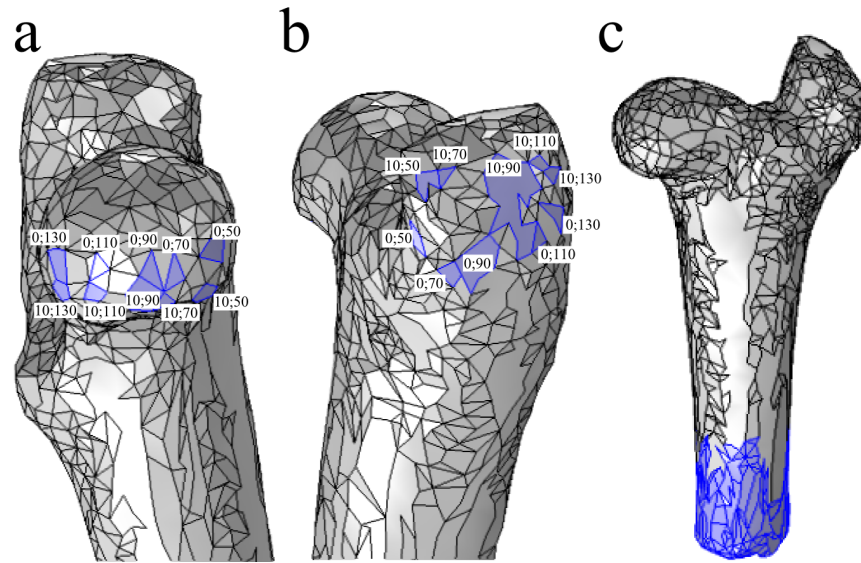


Figure 2.12: Position on the sheep femur of a) boundary loads and b) fixed boundaries for each loading condition. c) the fixed boundaries for all loading conditions at the distal end of the femur

homogeneous model was the mean modulus found by integration over the volume of the spatially dependent model.

### 2.4.1 Model

The sheep’s femur STL file was imported into Comsol. For the spatially dependent model, the modulus was entered through a linearly interpolated function using the method described in section 2.2. The ash density was limited to a minimum of  $\rho_{\text{ash}} = 0.05 \text{ g cm}^{-3}$ . The upper and lower limit of ash density values present in the model, and the corresponding Young’s modulus calculated from equations 2.3-2.4 are found in table 2.1. The Young’s modulus of the homogeneous model was set to 1 GPa. Rotations were applied as in the PVC model to align the femur along the coordinate axes. Fixed boundaries were applied to the distal 3 cm (figure 2.12c).

	Minimum	Maximum
$\rho_{\text{ash}} \text{ (g cm}^{-3}\text{)}$	0.05	1.1
$E \text{ (GPa)}$	0.015	12

Table 2.1: Minimum and maximum values of ash density and Young’s modulus.

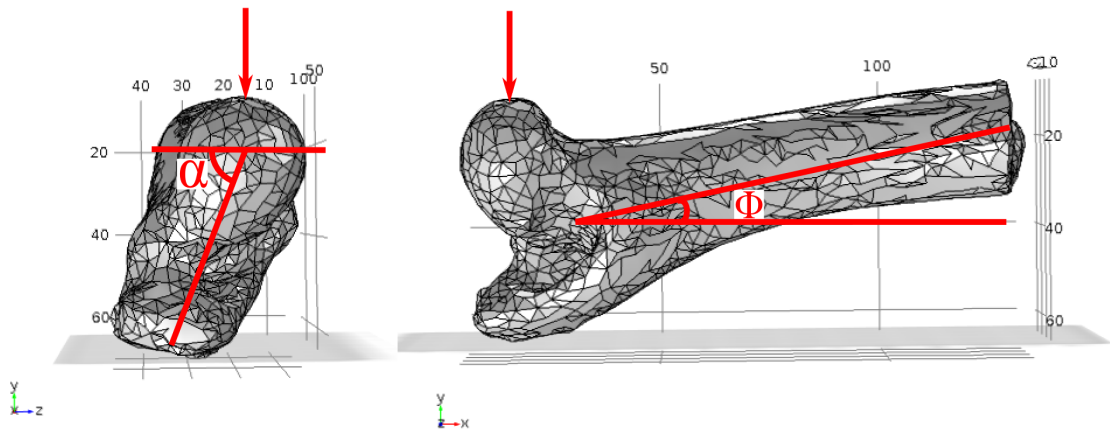


Figure 2.13: Angles  $\alpha$  and  $\phi$  defining the loading conditions of the sheep bone model. Arrow shows point and direction of application of 1 N load. A workplane touching the greater trochanter represents the floor.

The same range of  $\alpha$  and  $\phi$  angles were used as in the PVC model, with the same method of using workplanes to select the load and fixed boundaries (figure 2.12a and 2.12b). As these models used the geometry acquired from a left femur, as opposed to the right femur used in the PVC model, the direction of  $\alpha$  was reversed. The convention used was that  $\alpha = 0$  when the lesser trochanter is pointing towards the floor. Figure 2.13 shows both angles, with the workplane representing the floor and the arrow showing the point of application of the load. Again, a load of 1 N was applied to each of the load faces in turn.

## 2.4.2 Results

The maximum principal strains were mapped onto the surface of the femur for each set of loading condition for homogeneous model (figure 2.14) and spatially dependent model (figure 2.15). High strains are found around loading and fixed boundaries, similar to those calculated by the PVC model. Highly strained areas are found on the neck of the femur. This was also the case for the PVC model, so three sample points were taken on the superior, posterior, and inferior sides of the neck.

The strain distribution is broadly similar to that of the PVC femur, with high

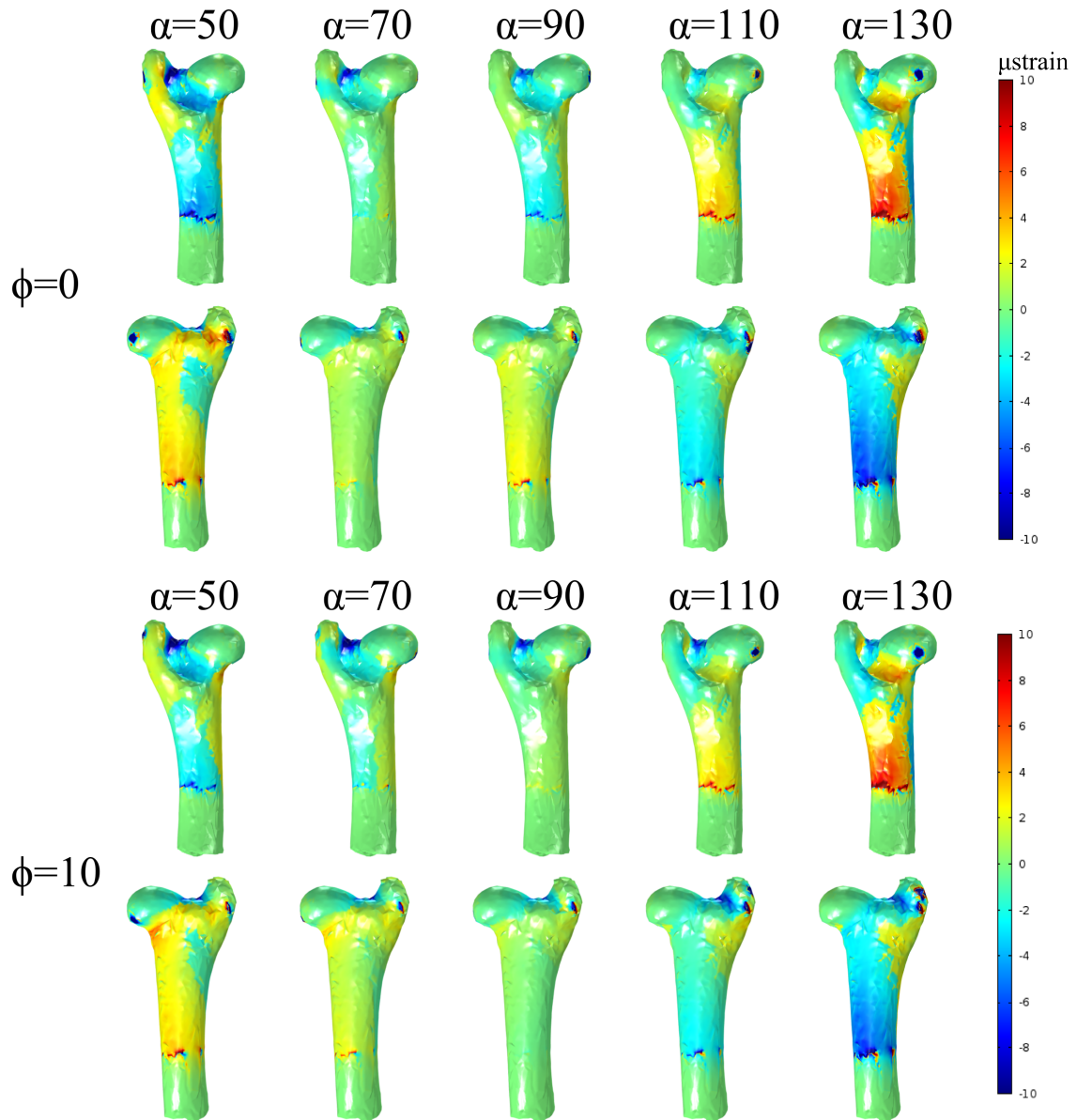


Figure 2.14: Maximum surface principal strain for each combination of  $\alpha$  and  $\phi$  for the homogeneous sheep femur model under 1 N load. The range of strains mapped was limited to  $\pm 10 \mu\text{strain}$ .

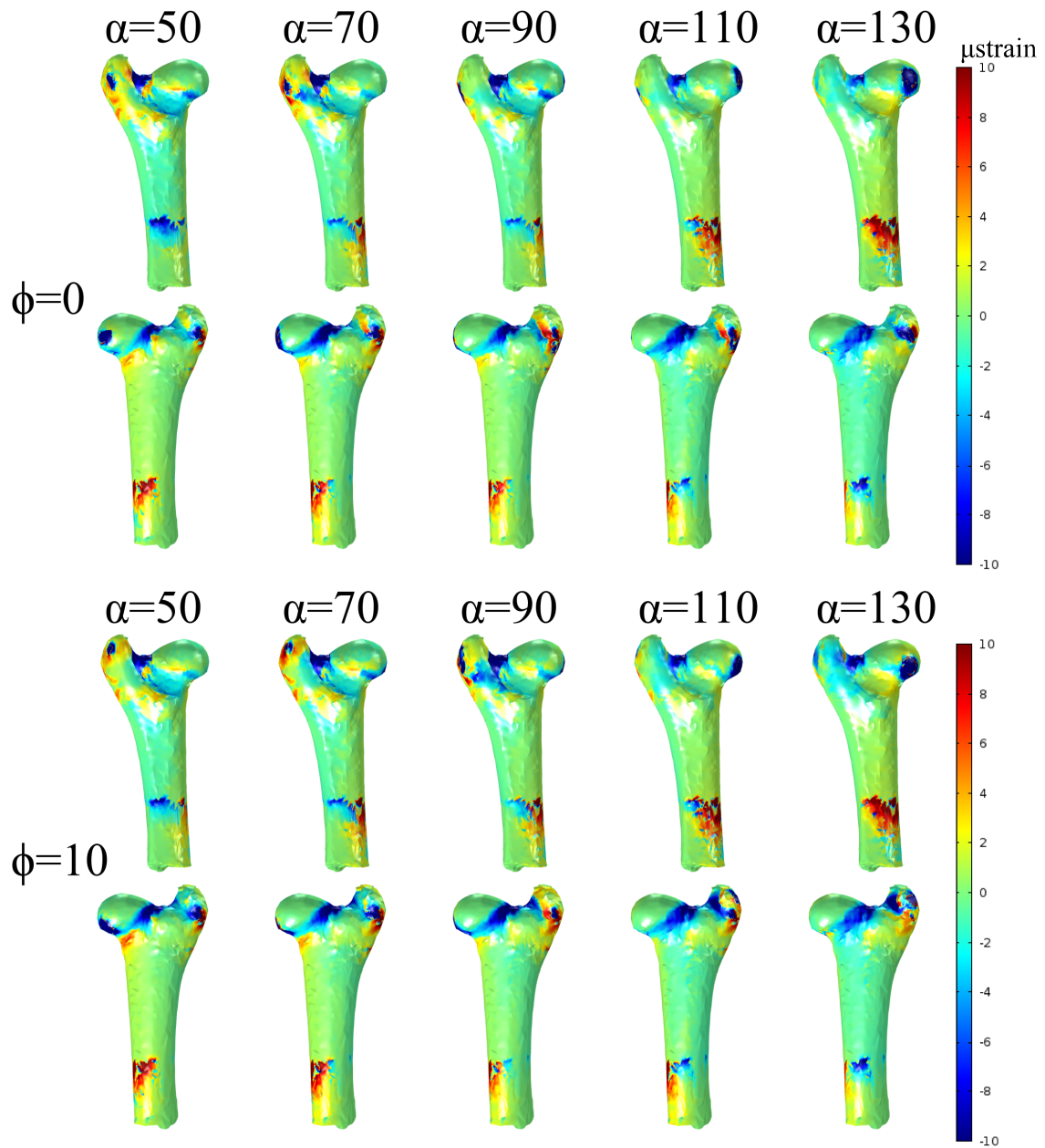


Figure 2.15: Maximum surface principal strain for each combination of  $\alpha$  and  $\phi$  for the spatially dependent sheep femur model under 1 N load. The range of strains mapped was limited to  $\pm 10 \mu\text{strain}$ .

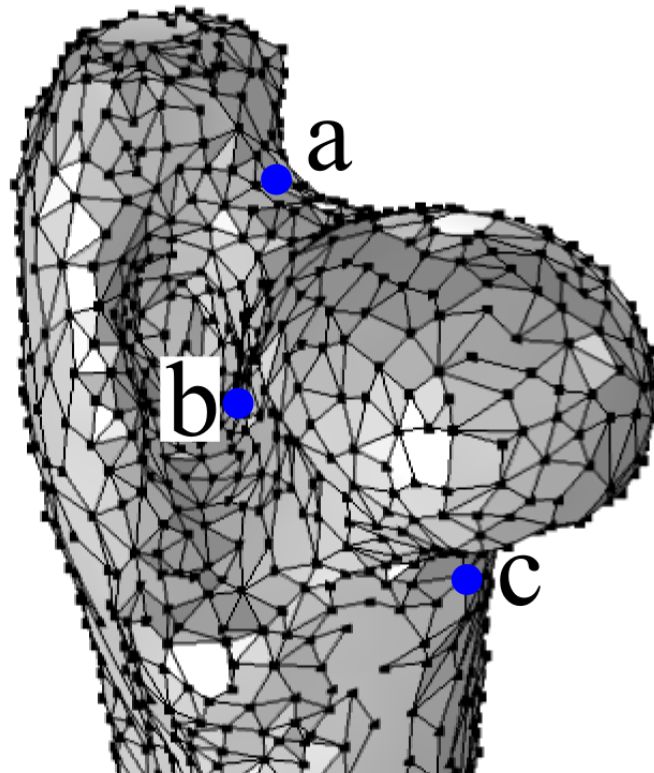


Figure 2.16: Location of the three sampled test points on both sheep bone models.

strain concentrations around the neck. Three strain sampling points were applied in a roughly analogous position to the sampling points in the PVC model (figure 2.16). The maximum strain is plotted for each loading condition for each of the two models is shown in figure 2.17.

For both models, the strain calculated at point a is always compressive. Point b is in compression at low angles and switches to extension between  $\alpha = 110^\circ$  and  $130^\circ$  in both models for both  $\phi = 0^\circ$  and  $10^\circ$ . Point c is always in extension in the homogeneous model, whereas it switches from extension to compression between  $\alpha = 110^\circ$  and  $130^\circ$  for both  $\phi$  values in the spatially dependent model.

In the homogeneous model, point a has the largest range of strains ( $6.1821 \mu\text{strain}$ ), followed by b ( $4.0395 \mu\text{strain}$ ) then c ( $1.7426 \mu\text{strain}$ ). The largest maximum strain is calculated at point a ( $-8.0440 \mu\text{strain}$ ), then b ( $-3.6264 \mu\text{strain}$ ), and the lowest at point c ( $1.9016 \mu\text{strain}$ ).

Point b shows the the largest range in strains calculated in the spatially depen-

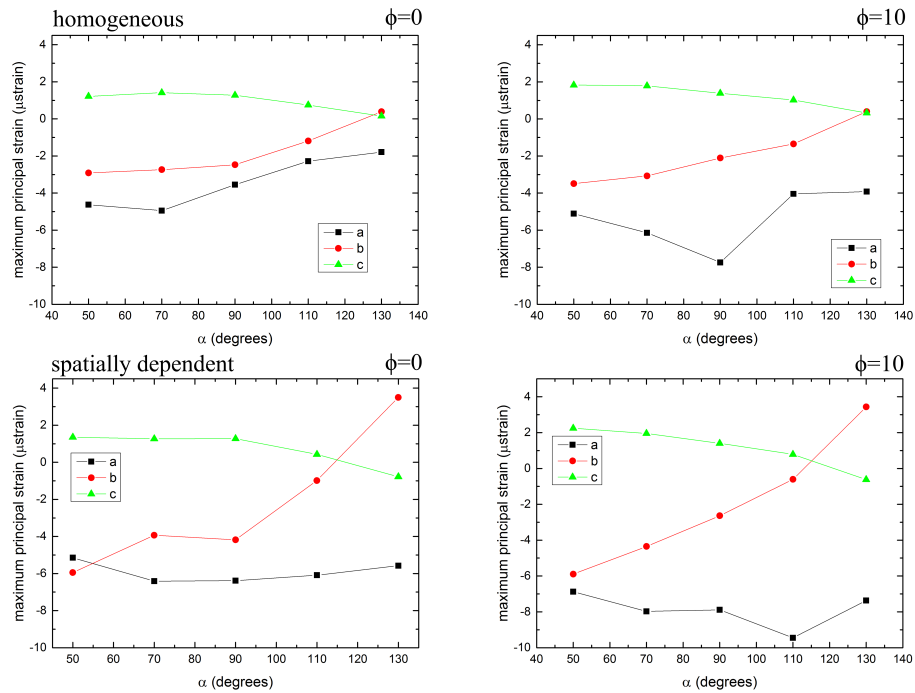


Figure 2.17: Maximum principal strain vs.  $\alpha$ : bone models.

dent model (9.4505  $\mu\text{strain}$ ), followed by a (4.3022  $\mu\text{strain}$ ) then c (3.019 46  $\mu\text{strain}$ ). The largest maximum strain is calculated at point a ( $-9.4514 \mu\text{strain}$ ), then b ( $-5.952 \mu\text{strain}$ ), and then c (2.2427  $\mu\text{strain}$ ).

## 2.5 Discussion

The results of this simulation have shown that loading the femur between the femoral head and the greater trochanter causes a highly strained area on the posterior side of the neck of the femur. This is in keeping with the expected location of hip fracture initiation.

Changing the orientation of the femur has a significant effect on the size of the strains observed. Rotation about the shaft can cause strains to change from compression to extension. Changing the angle between the shaft and the ground also has an affect.

Sampling strain data from the three test points in this model has shown that the

superior and posterior sides of the neck see the largest ranges in strain measurement across the simulated loading conditions, with the inferior side of the neck seeing a smaller but still significant range in strain.

The strains simulated in these models are not expected to match real fall situations, as 1 N is an unrealistically small impact load. The purpose of these models is to assess how strain distribution is affected by loading angle, and to eventually be able to compare with experimental results.

## 2.6 Conclusion

Computed tomography has been used to generate a geometric mesh of both a PVC proximal femur model, and the proximal portion of a sheep's femur. A  $K_2HPO_4$  CT phantom was created and used to calculate ash density in bone samples, which was used to develop a linear interpolated spatial function for Young's modulus for the sheep's femur.

Preliminary models were created for the both the PVC and sheep's femur to give an idea of how strain distribution is affected by loading angle, and to help determine where the largest strains are found on the surface of the femur. This will be a useful resource when designing experiments, for both deciding how to load the bone, and where to attach the strain gauges. Two sheep bone models were used to investigate the effect of the interpolated Young's modulus function determined from the CT scan. The data collected from these two models show that, while the strain distribution is largely determined by the geometry of the femur, the spatial variation of the Young's modulus has an effect on the strains. Although the morphology of the sheep's femur is quite different from the human femur, the strain distribution is similar, and the strains are largest around the neck. Strain gauges are best applied around the neck in both cases. A sensible choice would be to apply strain gauges to analogous points on the PVC and the sheep's femur. The sheep's femur is much smaller than the PVC femur, which will have a factor in where gauges can be placed.

This will be considered in chapter 5.

# Chapter 3

## Strain Measurement Techniques for Femoral Bone

### 3.1 Introduction

A central part of this project involves measuring strain in a bone sample. This needs to be done reliably, reproducibly, and without damaging the bone. The methods used to measure strain will be discussed in this chapter, including the choice of strain measurement configuration, the gauges used, and the procedures used to bond the gauges to the sample.

The way in which the samples will be attached to any loading apparatus will also be considered. Only the proximal portion of the femur is used, so the fixture of the distal end must be considered.

It is not known whether repeatedly freezing and defrosting strain gauged-bone has an effect on the reliability of the strain measurements. If the freeze-thaw cycles do cause the measurements to become unreliable, an upper limit will have to be placed on the number of times the bone is frozen and defrosted after the application of the strain gauges, potentially restricting the possibility of repeating measurements. An experiment was devised to assess the reproducibility of strain measurements taken after multiple freeze-thaw cycles.

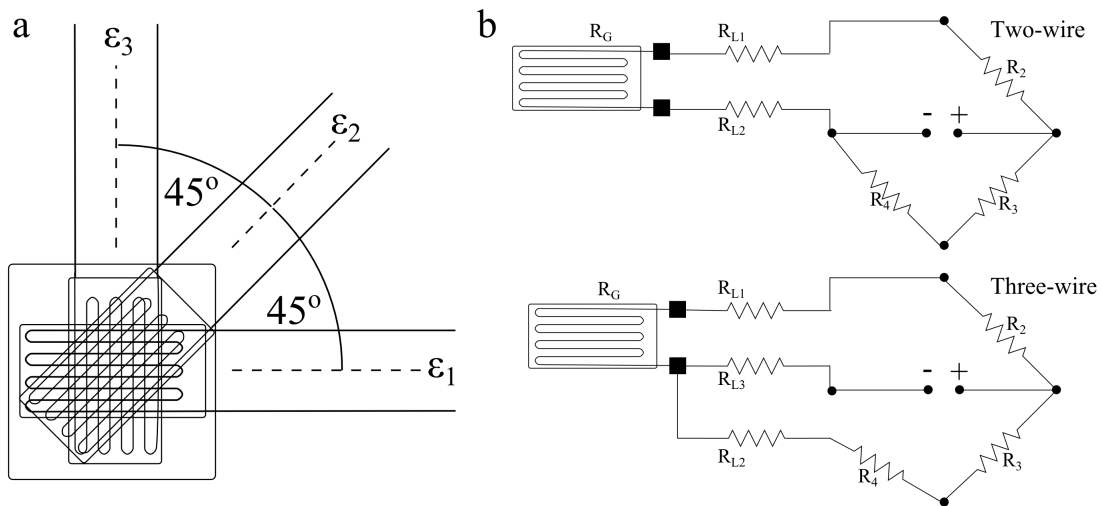


Figure 3.1: a) The rosette gauges used in this project consist of three single strain gauges stacked a single backing foil. The gauges are aligned at  $0^\circ$ ,  $45^\circ$ , and  $90^\circ$ . b) Circuit diagram of the strain gauge quarter-bridge circuit in the two-wire and three-wire arrangement. Both lead wires are connected to the same arm of the bridge, resulting in an increased resistance in this arm and causing the bridge to become unbalanced. In the three-wire circuit, the lead wire resistances  $R_{L1}$  and  $R_{L2}$  are joined to separate arms of the bridge, one either side of the output sensor. If  $R_{L1} = R_{L2}$ , the bridge will be balanced when  $R_G = R_2 = R_3 = R_4$ .

## 3.2 Strain Measurement

### 3.2.1 Apparatus

As stated in chapter 2, strain gauges will be used to take the experimental surface strain measurements. Strain gauges measure strain along one axis. In a system with changing load positions and directions, the direction of the largest surface strain at the gauge location is liable to change, meaning that a change in strain direction could be misinterpreted as a change in strain magnitude. Tri-axial (rosette) strain gauges consist of three single gauges laid on top of each other, aligned along three different directions (figure 3.1a). This allows for the measurement of the two linear strain components as well as the shear strain. This means that the largest measurable surface strains can always be measured, regardless of their direction.

An eight channel strain amplifier (Fylde Electronic Laboratories Ltd, Preston, United Kingdom) was used to provide strain measurements. The amplifier was connected to a PC where the data was acquired with Madaq, a labview executable file designed by Fylde for use with the Fylde amplifier. Each channel can be used to record the data from one single strain gauge when attached in quarter-bridge con-

figuration. Rosette gauges require one channel per component gauge, so this allows for the use of a maximum of two rosette gauges and two single gauges. In chapter 4, the positioning of the four gauges will be considered.

Two  $120\ \Omega$  single strain gauges (RS Components Ltd., Corby, UK) and two  $120\ \Omega$  rosette gauges ( $0^\circ/45^\circ/90^\circ$ , Omega Engineering Limited, Manchester, United Kingdom) were bonded to each sample. The gauges were acquired pre-wired. The single gauges are sold with adhesive contact pads to provide a point to solder gauge wires and lead wires to. The pads allow the lead wire to be secured to the surface of the sample, this avoids putting large tensions through the delicate gauge wires. Terminal pads (Omega) were glued to the samples to perform the same task for the rosette gauges. The strain gauges were connected to the strain gauge amplifier channels in a quarter bridge arrangement. A three-wire arrangement was used to help eliminate lead wire resistance (figure 3.1b). In a two-wire circuit, the resistances of the lead wires are both connected to one arm of the bridge, causing an imbalance in the bridge which could be misread as strain. In the three-wire case, one arm of the strain gauge is soldered to two leads, one connected to the bridge circuit and the other to the sensor. The other gauge arm is connected to another arm of the bridge circuit. If the resistances of the two lead wires connected to the bridge are assumed to be identical, they cancel one another out. In reality, the resistances of the lead wires are not identical and so do not cancel out perfectly, but the three-wire arrangement helps to reduce the imbalance. The third wire acts only as a voltage sensing wire, and does not contribute to the resistance of the bridge circuit.

The strain measured by a strain gauge is affected by thermal expansion of the material to which it is bonded. Strain gauges are frequently designed to compensate for the thermal expansion matched to aluminium or steel samples. The thermal expansion coefficient of bone is  $27.5 \times 10^{-6}/^\circ\text{C}$ , [51], and the coefficients listed by RS for aluminium and steel matched gauges are  $23.4 \times 10^{-6}/^\circ\text{C}$  and  $10.8 \times 10^{-6}/^\circ\text{C}$  respectively. The aluminium matched gauge has the closest coefficient to bone, so this one was used. As this is not a perfect compensation, it is important prevent the temperature of the bone from changing drastically. Any bone samples stored

in a freezer will be allowed to reach thermal equilibrium for 30 minutes before any measurements are taken. A large excitation voltage can cause an increase in gauge wire temperature. The strain amplifier was set to the smallest possible excitation voltage, 2.5 V, to minimise this effect.

The principal strains are the components of the strain measured at an angle where the shear strain is zero. They are the maximum measurable strains at that specific point. As the principal strains do not depend on the direction in which the gauge is aligned along, they were chosen as a suitable variable to use for comparison between the experimental data and the finite element analysis. Strain measurements from each of the three components gauges of a rosette gauge,  $\epsilon_1$ ,  $\epsilon_2$ , and  $\epsilon_3$ , can be used to compute two principal strains on the surface of a sample [52],

$$\epsilon_{p1} = \frac{\epsilon_1 + \epsilon_3}{2} + \frac{1}{\sqrt{2}} \sqrt{(\epsilon_1 - \epsilon_2)^2 + (\epsilon_2 - \epsilon_3)^2} \quad (3.1a)$$

$$\epsilon_{p2} = \frac{\epsilon_1 + \epsilon_3}{2} - \frac{1}{\sqrt{2}} \sqrt{(\epsilon_1 - \epsilon_2)^2 + (\epsilon_2 - \epsilon_3)^2} \quad (3.1b)$$

### 3.2.2 Applying Strain Gauges to Bone

The surface of the bone must be prepared before bonding strain gauges to it. Uneven or greasy surfaces provide poor adhesion for the glue, so it is possible that the bond might fail if the surface is not prepared adequately. The exact technique implemented to do this varies, but most studies follow a procedure of stripping the bone of soft tissue, degreasing and then abrading the bone surface, before finally bonding the gauge.

Ota [20] used a knife and sandpaper to remove soft tissue from the bone and then cleaned it with isopropyl alcohol, before bonding the gauges with adhesive cyanoacrylate. Write [53] used multiple applications of a procedure that consisted of applying chloroform methanol to degrease the surface and then scraping with sandpaper. An ammonium solution was used to neutralise the surface, and cellophane tape was used to hold the gauge in place while an adhesive was used to bond it to the bone. Yosibash [22] used ethanol to degrease the bone, then sanded the the surface and cleaned it again with ethanol. Cyanoacrylate was used to bond the

gauges.

Cordey and Gautier [54] provide a guide for bonding pre-wired strain gauges to bone in-vivo. They recommend stripping the periosteum where the gauge will be applied, degreasing with chloroform and wetting with sterile water. Cyanoacrylate is applied to the underside of the gauge which is then placed on the prepared surface and pressed down for 30 seconds. Teflon foil is used to prevent gloves from sticking to the bone. Finally, cyanoacrylate is applied to the top of the gauge to prevent slipping.

The following procedure was used to stick both gauges and terminal pads to the bone:

1. Remove all excess soft tissue with number 10 scalpel blade. This step is described in section 2.2.2, as it is necessary to remove soft tissue before scanning.
2. Sand surface of gauge site with 40-grit sandpaper.
3. Apply isopropyl alcohol to the surface to remove any remaining grease.
4. Apply a small length of foil-backed tape to across the gauge to hold it in place on the surface of the bone. The foil is peeled back, along with the gauge, and cyanoacrylate is applied to the back of the gauge. The tape is pressed back down onto the bone, pressure is applied by hand for 30 seconds, then the tape is removed after 10 minutes.
5. A thin layer of cyanoacrylate is applied to the top of the gauge to protect it. The terminal pads need to provide a surface that solder will adhere to, so they are not coated in cyanoacrylate.

The same procedure is used when bonding gauges to the PVC femur model.

### 3.3 Distal Fixture

The apparatus which will be designed to load the PVC and bone samples will be constructed largely from steel and aluminium. In the body, bone is protected

by soft tissue which dampens impact and spreads load across a wide area to reduce pressure. The irregular morphology of bone means that, if an exposed bone is placed in a steel clamp or pressed against a steel plate, the contact area will be small so pressure will be comparatively high. The results of the preliminary models described in chapter 2 show that small discrete loading areas lead to a very high localised strain concentration, which could potentially cause damage to the bone. If a sample is damaged during testing, it will not be possible to compare results from before and after the damage occurred. Any method used to hold the sample in the apparatus must use a sufficiently large surface area to avoid damaging the bone. Section 2.2 stated that both the bone and PVC samples needed to be cut down to fit in scanner. The distal end of the femur must be fixed in the loading apparatus without being damaged.

A frequently used solution is to embed the distal end of the proximal femur in polymethyl methacrylate (PMMA) bone cement [16,20,22]. The PMMA is moulded to the surface of the bone, so the force can be applied through a large contact area. It also seals the cut face, helping to prevent water and mineral loss. PMMA (or similar materials) is often used to make a cap through which a compressive load is applied, spreading the load across a greater surface area than would be achieved by a flat plate [14, 16, 20].

PMMA bone cement was used to fix the distal ends of the samples into metal cylinders, which could then be fixed to the loading apparatus. A 50 mm diameter aluminium tube was cut to 50 mm long. A 30 mm thick plate was cut to the same cross section as the tube and welded to one end to seal the cylinder. The end plate was thick enough that a threaded hole could be drilled into it so that it could be screwed into apparatus. The rest of the design of the apparatus will be discussed in chapter 4.

### 3.3.1 PMMA

Palacos R PMMA bone cement (Heraeus Medical, Newbury, United Kingdom) was used throughout this project. This cement is supplied as a monomer liquid and a polymer powder. A polymerisation reaction occurs once the two components are combined and the cement forms a paste which gradually hardens to a mouldable dough, and continues to harden into a hard solid. This cement comes with instructions for polymerisation by hand-mixing. The liquid component is to be put in the mixing vessel first followed by the powder, as reversing the order can result in powder nests. The quantity of powder in a sachet is matched exactly to the amount of liquid in an ampoule, so the entirety of one sachet and one ampoule are used. The components are hand mixed for 30 seconds, then left to harden for approximately 15 to 30 seconds (depending on the room temperature), or when it no longer adheres to rubber gloves.

The density of the mixed cement needs to be as high as possible, as the introduction of air into the cement could compromise the strength of the structure. It is desirable to achieve good contact between cement and bone, and cement and cylinder. The technique described above was tested with an aluminium cylinder (described above) and a 30 mm diameter aluminium cylinder to simulate the femoral shaft. An aluminium rod (diameter 3 mm) was used to stir the cement in an 8 cm diameter glass mixing vessel. The instructions given in the manual were followed, with rapid mixing. Following the waiting time, the cement was removed from the vessel and shaped into a cylinder of a similar diameter as the aluminium cylinder. It was pressed into the aluminium cylinder, ensuring that there were no air pockets at the base. A well was made in the centre of the cement, and the inner cylinder was pressed into it.

A CT scan was performed to investigate the internal structure of the cement (145 kVp, 310 mAs, 0.04477 mm voxel size,  $1920 \times 1920$  pixel slice area, 1536 slices) (figure 3.2a). Some large voids are present (of around 5 mm across), including one void which spans the entire width of the channel of cement which surrounds the side of the central cylinder.

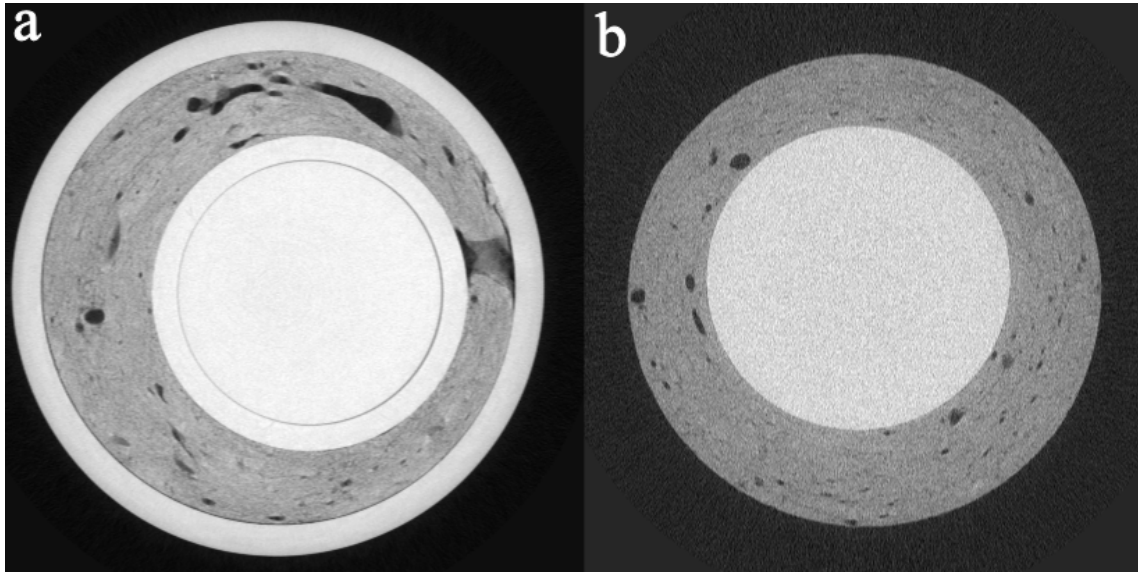


Figure 3.2: Images from the CT scans of the bone cements test using a) only the instructions supplied with the cement and b) the procedure recommended by Eyerer and Jin.

The outer cylinder was removed in order to inspect the voids present in the surface of the cement. PMMA bone cement does not chemically bond to surfaces, but it is held in place by friction. The relatively smooth surface of the aluminium meant that it was possible to twist the cement free from the outer cylinder using a vice. The void passing all the way through the cement at the side of the cement can clearly be seen in figure 3.3. It is clear that a refined method must be used to reduce the size and number of the air voids.

Eyerer and Jin [55] investigated the effect using different mixing techniques on the quality of a number of different cement brands, including Palacos R, specifically comparing density, hardness, and strength. They reported on an improved mixing technique. They recommend mixing the cement in a 6-8 cm diameter porcelain or plastic vessel with a rounded-off sheet-metal strips or plastic. The cement is mixed for 30 seconds at a rate of 10 rpm, as extensive and vigorous mixing leads to a higher porosity. After mixing, a kneading time of 20-30 seconds is recommended. Kneading bursts surface bubbles, reduces overall porosity.

Another test was performed using this method. An 8 cm diameter plastic beaker was used, along with a 5 mm wide length of aluminium sheet to stir. The sheet



Figure 3.3: The result of the first PMMA test, outer cylinder removed. The void spanning the entire thickness of the side of the cement is visible in the centre of the image.

provides a larger surface area than the rod, and helps to mix the cement more efficiently with less agitation. The powder and liquid were mixed together as gently as possible until the two were just combined. This is more practical than enforcing a strict time because it means that the point where the two are properly mixed can be determined by eye, but overmixing is still avoided. The cement was left for 15 seconds after mixing, then kneaded for 20 seconds. Care was taken to avoid introducing folds into the cement while kneading.

Eyerer and Jin also recommend applying force to the cement during polymerisation to increase the density. The femur was pushed firmly into cement by hand, and the aluminium mixing strip was used to press the cement around the femur down and towards the side of the femur to make sure there were no gaps at the sides.

A CT scan of the cement made with this method was performed (140 kVp, 287 mAs, 0.0335 mm voxel size,  $1920 \times 1920$  pixel slice area, 1536 slices), and the results of the scan were compared with those of the previous scan (figure 3.2b). This time, the outer cylinder was removed prior to scanning. Small voids are still present, up to around 1.5 mm in diameter, but none as large as those seen in the previous scan.

The method described by Eyerer and Jin will therefore be implemented in all future uses of the Palacos R bone cement.

## 3.4 Freeze-Thaw Cycling

Due to the short time frame at which organic tissue decays, it is useful to be able to store the bone samples in a freezer between uses. Studies have been done to show that patellar [56] and fibular [57] allograft bone samples can both be put through eight freeze-thaw cycles without significant change to the mechanical properties. The bones used in our experiments will have strain gauges bonded to them, so it is necessary to investigate whether the gauge-glue-bone bond will deteriorate during the freeze thaw cycles, thus affecting the strain readings. In order to test this, an experiment was designed that could be exactly replicated once a week for six weeks.

### 3.4.1 Freeze-Thaw Experiment

An experiment was designed to measure the strain response in a pig rib bone (Joseph Morris, Wigston, United Kingdom) under mechanical loading. A relatively straight rib was chosen to make loading and fixing easier. The experiment was designed to be repeatable, the aim is to observe whether the results change over time so it is important that the loading conditions are easily repeatable between repetitions.

Each end of the rib was set in PMMA bone cement. The cement was moulded around each end of the rib, covering approximately 10 mm along the length of the bone to ensure the cement would not slip off once it had set. Prior to hardening, each cemented end was pressed into a greased square aluminium mould. This gives the cement flat edges so that it can be easily held in a clamp.

The rib was loaded by suspending two weight holders off it. By using two points of application, the highly strained portion of the bone is distributed between the two weight holders. If a single holder was used, the strain would be concentrated in a

smaller area beneath the load point, making it more susceptible to fracturing. Two PMMA “saddles” were made for the weight-holders to rest on to ensure that they sit in the same place each time. The PMMA also serves to spread the stress across the surface of the bone, avoiding crushing due to high pressures. Two small pieces of PMMA were moulded against the surface of the rib, and the weight holders were used to press a groove into the PMMA. Care was taken to ensure that the PMMA was wrapped around the rib so that it would not come away from the bone once it was set, while also ensuring that the two saddles did not touch, and that space was left between them on the underside of the bone for a strain gauge to be attached. A single strain gauge was bonded to the underside of the rib using the technique described in section 3.2.2.

The load frame for this experiment is shown in figure 3.4. A frame was built consisting of two aluminium end bars which rested on either end of the rib. Each end bar was bolted to a separate steel sheet, which were bolted to a steel frame leaving 50 mm space between them, and 200 mm vertical clearance beneath them. One end bar was fixed in place and the other was bolted along two slots which allowed it to move towards and away from the other end bar, but remain parallel. Two holes were drilled into the moving bar, and a threaded rod was passed through each hole. The threaded rods were positioned so that their ends touched the other bar when the rib was in place. They were bolted into place so that the distance between the two bars could easily be replicated the next time the experiment was carried out. Each bar had two side bars bolted to it, one fixed and one movable, which held the sides of the PMMA in place.

The rib was placed between the bars and held in place with the side bars, all of which were then screwed into place. The bolts were adjusted so that they met the stationary bar, and the bolts were tightened. This ensures that the bars are the same distance apart each time the experiment is carried out.

The strain measurement was set to zero with the weight holders not suspended from the rib. The holders were placed onto the PMMA saddles with three 50 g

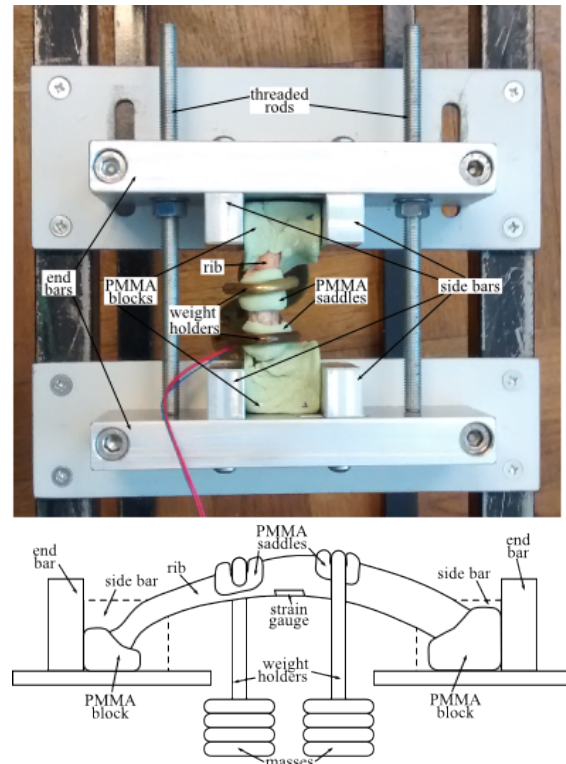


Figure 3.4: The loading frame, with loaded rib, shown from above (photo) and the side (diagram).

masses attached to each, and the strain was measured. The strains induced in this experiment are not time dependent, so it is not necessary to record them over time. The strains were read by eye from Madaq's display. After the strain was recorded, another 50 g mass was added to each holder, and the strain was recorded again. This process was continued until there were 10 masses on each holder. The holders were removed from the rib, and the rib was removed from the load frame. The rib was secured back in the frame and the process was repeated. This is to reduce the potential error caused by incorrectly clamping or loading the rib. After four loading cycles, the rib was wrapped in polythene again, with the PMMA, strain gauge, and lead wires still attached, and returned to the freezer for seven days. The experiment was repeated every week for six weeks.

### 3.4.2 Results

Data from each week is displayed in figure 3.5. A statistical test is required to compare the data from week to week to determine whether it can be considered consistent throughout the duration of the experiments or if there is a change. This

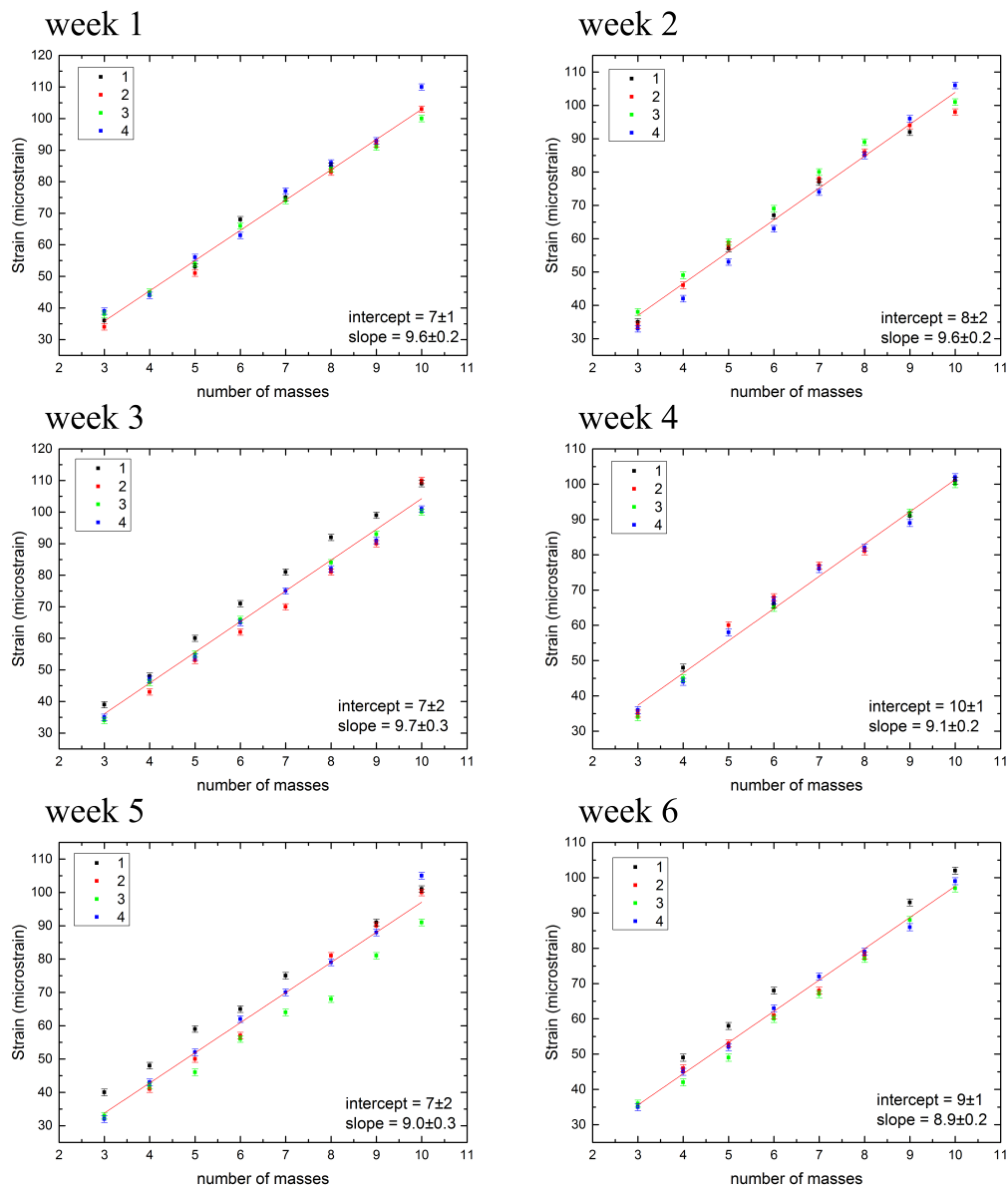


Figure 3.5: Strain vs. number of masses for the data collected from each week. The data taken in each of the four loading cycles is plotted separately, but the intercept and slope is calculated for the all the data taken that week pooled together. It is assumed that the strain response to leading is linear.

can be done by separately comparing the intercepts and slopes of the lines of best fit calculated for each week. If the results change over time, the possibility that the strain measurements are affected by frequent freeze-thaw cycles cannot be ruled out.

### 3.4.2.1 Statistical Data Analysis

The data taken across each iteration of the experiment was compared statistically to determine whether there was any variation from week to week. Analysis of covariance (ANCOVA) is a tool used to statistically compare dependent variables (in this case strain) which have an associated covariate (number of masses), and determine whether they are equal. A version of ANCOVA was used which consists of two tests of two separate null hypotheses. The null hypotheses associated with the first test is that the slopes of all datasets shown in figure 3.5 are equal, and the second is that the intercepts are all equal [58].

A test statistic is calculated from the strain data for each null hypothesis. If the test statistic lies below a threshold value (a critical value of the F-distribution determined by the degrees of freedom for this test and the desired threshold probability), the null hypothesis is not rejected and the data from each week can be considered to have the same slope (in the case of the first test) or intercept (in the case of the second test). If the test statistic exceeds the threshold, the variation in the data is considered to be statistically significant and unlikely to have happened by chance. In this case, the null hypothesis is rejected, and the strain is considered to differ between weeks.

The formula used to determine the test statistic,  $F_1$ , associated with the null hypothesis that all of the slopes are the same, requires the calculation of the pooled residual sum of squares,  $SS_p$ , and the common residual sum of squares,  $SS_c$ .  $SS_p$  is the sum of the residual sum of squares for each week  $j$ , over a total of  $k$  weeks. This is calculated from the deviations of  $x_{ji}$  (number of masses) and  $y_{ji}$  (strain) from

their respective week means  $(\bar{x}_j, \bar{y}_j)$ , and their cross product.

$$A_j = \sum_{i=1}^{n_i} (x_{ji} - \bar{x}_j)^2 \quad (3.2a)$$

$$B_j = \sum_{i=1}^{n_i} (x_{ji} - \bar{x}_j)(y_{ji} - \bar{y}_j) \quad (3.2b)$$

$$C_j = \sum_{i=1}^{n_i} (y_{ji} - \bar{y}_j)^2 \quad (3.2c)$$

$$SS_p = \sum_{j=1}^k \left( C_j - \frac{B_j^2}{A_j} \right), \quad (3.2d)$$

where  $n_i$  is the number of results gathered each week.

$SS_c$  is the residual sum of squares calculated from the sums of  $A_j$ ,  $B_j$ , and  $C_j$  across all weeks,

$$A_c = \sum_{j=1}^k \sum_{i=1}^{n_i} (x_{ji} - \bar{x}_j)^2 \quad (3.3a)$$

$$B_c = \sum_{j=1}^k \sum_{i=1}^{n_i} (x_{ji} - \bar{x}_j)(y_{ji} - \bar{y}_j) \quad (3.3b)$$

$$C_c = \sum_{j=1}^k \sum_{i=1}^{n_i} (y_{ji} - \bar{y}_j)^2. \quad (3.3c)$$

$$SS_c = C_c - \frac{B_c^2}{A_c}. \quad (3.3d)$$

The number of degrees of freedom associated with each of these residuals are

$$DF_p = k(n_i - 2) \quad (3.4a)$$

$$DF_c = kn_i - k - 1. \quad (3.4b)$$

The test statistic of the first null hypothesis is

$$F_1 = \frac{(SS_c - SS_p)/(k - 1)}{SS_p/DF_p} \quad (3.5)$$

with degrees of freedom  $k - 1$  and  $DF_p$ .

The second hypothesis requires the calculation of the total residual sum of

squares. This number,  $SS_t$ , is the residual sum of squares when all of the data has been pooled together. The test statistic for the second null hypothesis is

$$F_2 = \frac{(SS_t - SS_c)/(k - 1)}{SS_c/DF_c}. \quad (3.6)$$

The degrees of freedom are  $k - 1$  and  $DF_c$ . For the null hypotheses to be rejected, the test statistic must exceed a threshold value decided by a desired level of significance. The desired level of significance for both test statistics is 0.05.

All statistical calculations presented here were implemented in statistical programming language R, including the calculation of the thresholds for each  $F_1$  and  $F_2$  value. The calculations were initially run for the entire data set, with  $k = 6$  weeks and  $n_i = 8 \times 4 = 36$  data points for each week. The first test statistic was calculated to be  $F_1 = 2.183$ , which falls below the threshold value  $F_{1\text{thresh}} = 2.2643$ . The null hypothesis is not rejected and the slopes are considered to all be equal. The second test statistic is  $F_2 = 13.56$ , exceeding the threshold  $F_{2\text{thresh}} = 2.2629$ . The associated p-value for this statistic is  $2.8234 \times 10^{-11}$ . The null hypothesis is rejected, signifying a difference in intercept between weeks. This result indicates that there is statistically significant variation in the strain measurements as a response to loading between weeks. It does not include information about when this variation arises.

The ANCOVA tests were carried out five more times, this time including the data after each repeated week. The first test compared data from the first and second weeks ( $k = 2$ ), the next tests compared the first, second, and third weeks ( $k = 3$ ), and so on. The test statistics, along with their associated p-values ( $p_1$  and  $p_2$ , associated with the first and second null hypotheses respectively) and the threshold test statistics for a significance level of 0.05, are displayed in table 3.1.

$F_1 < F_{1\text{thresh}}$  after each repetition, confirming that there is no significant variance in the slopes.  $F_2$  is below the threshold after the second, third, and fourth weeks, and exceeds the threshold in weeks five and six. The second null hypothesis cannot be rejected after three freezing and defrosting cycles, but is rejected after four. There is no significant variation in the data collected within the first four weeks of

Week	2	3	4	5	6
$F_1$	0.005270	0.1694	1.422	1.528	2.183
$F_{1\text{thresh}}$	4.001191	3.097698	2.680168	2.431965	2.264310
$p_1$	0.94237	0.84444	0.23984	0.19674	0.058049
$F_2$	2.500	1.071	1.235	12.71	13.56
$F_{2\text{thresh}}$	3.998494482	3.095432750	2.678300858	2.430384512	2.262937383
$p_2$	0.11902	0.34690	0.29998	$5.8022 \times 10^{-9}$	$2.8234 \times 10^{-11}$

Table 3.1: Test statistic,  $p=0.05$  threshold test statistic, and  $p$ -value associated with the two null hypotheses calculated for data collected following each repeated week.

the experiment.

The results of this experiment imply that strain measurements taken after one, two, and three freeze thaw cycles will be reliable, but the reliability of measurements taken after any further cycles cannot be guaranteed. It cannot be concluded without further investigation that this result is definitely caused by a change in the strain gauge-bone bond, only that some change has occurred to change the results of the experiment over time. Although attempts were made to make the conditions of the experiment as similar as possible each week, it is possible that the inconsistency of the results was caused by a change to the set up of the apparatus, or to the bone itself. For the purpose of this project, however, this must be understood as a limitation on the number of allowable freeze-thaw cycles. The sheep femur can be refrozen a maximum of three times after the gauges are bonded, the results of any experiments taken after a fourth cycle cannot be considered reliable.

### 3.5 Conclusion

Single and rosette strain gauges have been selected for measuring surface strain in both the PVC and bone samples, as has a technique for preparing the samples and bonding the gauges.

A method for sealing the distal end of the femur and embedding it into an aluminium cylinder using PMMA bone cement was refined. This method employs the

gentle mixing and kneading of the cement to minimise the introduction of air into the mixture.

The PMMA cement was used with a pig rib in the design of a mechanical loading experiment to test the effect of multiple freeze-thaw cycles on strain measurement with strain gauges. Strain measurement was confirmed to be consistent after three freeze-thaw cycles, but the reliability of any measurements taken after four cycles could not be guaranteed. Although it is not possible to attribute the inconsistency of the strain measurements to the gauge-bone bond without further investigation, the freeze-thaw cycles limit must be adhered to in order to ensure that inaccuracies due to this factor are eliminated.

## Chapter 4

# Computational and Experimental Investigation of Strain in a PVC Femur Model

### 4.1 Introduction

One of the aims of the work presented in this thesis is to develop a finite element model to simulate strain in a femur under various loading conditions. The model will be validated by an experiment with results which will be compared with the model. The experiment and model will be designed and implemented with the PVC femur prior to any work being carried out with bone sample. The PVC femur has homogeneous material properties, making the model less susceptible to error than it would be for the sheep femur with its spatially dependent Young's modulus. PVC is an easier material to work with as none of the safety precautions associated with organic tissue are necessary, and, unlike bone, it does not decay over time. The amount of time that the bone sample can be kept at room temperature is limited. There is no limit to the number of readings which can be taken with the PVC femur. The information gathered from the PVC femur model and experiment can be used to select a subset of loading conditions to investigate with the bone sample.

The results of the experiment performed with the PVC model femur will affect the way that the bone experiment is designed. Carrying out this experiment with

the PVC femur will indicate any problems with the experimental design which can be remedied or improved before any experiments are carried out with the real bone sample.

This chapter will describe the design of the apparatus used to hold the distal end of the femur when it is loaded. This apparatus will be used with both the PVC and sheep femur samples. Many of the studies done on loading femoral bone have used a loading condition which replicates stance or gait. Often, the distal end of the bone is embedded into a fixture attached to the loading frame, and the load is applied to the femoral head through a moulded cap [14, 16, 20]. Depending on the purpose of the study, strain is measured as the load is increased slowly over time [14, 22], or the strain due to a static load is measured [20]. In some cases, the femur is tested to failure [14, 16, 20].

Keyak [16] compares fracture conditions in both the stance and fall configurations. In the latter case, the distal end is embedded in a fixture, and PMMA caps are moulded to the points of contact on the femoral head and the greater trochanter. A moulded PMMA cap provides a large contact area, but only to part of the surface of the femoral head. If the angle of the femur is to be altered, the point at which the femur contacts the apparatus will also change. It is preferable to use a socket more like a real acetabulum, in which the femoral head can rotate freely.

A quasi-static applied load was used for the experiment described in this chapter, the load was increased slowly and strain was measured at the same time. Keyak [16] reported an average failure load in the fall configuration of 2.4 kN, so the maximum load was much lower than this. Strain per Newton of applied force was measured at each of the gauge sites, this was calculated from the gradient of the strain measurement. This is preferable to setting a static load and measuring strain, as the strain can be calculated from all of the data sampled by the strain gauge amplifier rather than a single strain reading, thus reducing the effect of any errors. The application of a static load can be unreliable and difficult to carry out precisely, as the load applied to the bone tends to decrease as soon as it is applied due to compliance in

the system [20].

A load frame was designed and manufactured to hold the femur inside the aluminium cylinder in a sideways fall position, and allow the bone to be held at a range of angles. The load was applied to the femoral head through a load cell attachment designed to simulate the contact conditions of the acetabulum. The femur was able to rotate freely inside the attachment, as it would in the hip joint.

A finite element model similar to the preliminary model reported in section 2.3 was built, but with forces applied by contact simulation instead of boundary loads. The preliminary model shows where the areas with the largest strain concentration are, the selection of the gauging points was based on this information. Trilateration was used to match the location of the gauges to the corresponding strain measurement points on the model. This technique, which has not been used for this purpose before, was used to compute the model coordinates corresponding to each strain gauge location from the distances between each gauge and a number of easily identifiable reference features on the surface of the femur.

## 4.2 Experiment

### 4.2.1 Design

The results of the finite element model reported in Chapter 2 show that the orientation of the bone has an effect on the magnitude and distribution of the strain induced in the femur. This information influenced the decision to carry out an experiment where the femur is held at various loading angles with respect to the load cell and loading platform.

A Hounsfield tensometer (Instron 3300) with a 500 N maximum load cell was used to apply compressional force to the samples. The loading frame is connected to a PC running Instron's testing software, Bluehill, which allows the application of the load to be automated by entering the rate of increase of load per minute, along

with a maximum load. Any apparatus designed to hold the femur must be bolted to the loading frame of the tensometer. The interface used to apply the load to the must be attached to the tensometers load cell, which has a clevis attachment.

In section 2.3, two angles,  $\alpha$  and  $\phi$ , were used to categorise each loading condition. The same two angles will be used for this experiment, with the addition of a third angle,  $\theta$ , measuring the angle between the load cell and the surface of the apparatus in contact with the greater trochanter.

A right femur model was initially used for this project, and was used to provide the geometry for the preliminary model described in section 2.3, however a broken gauge resulted in this sample being unusable for the experiment. Pre-wired gauges were not used for the right femur, and wires had to be soldered directly to the solder pads on the gauges. The small size of these pads meant that the solder joint was not strong enough for the gauge to be soldered prior to bonding to the surface of the femur, and the irregular geometry of the femur made it difficult to solder once it was bonded to the surface. As a result, one of the solder pads became damaged, and the sample was unusable. A left PVC femur acquired from the same source was obtained, as a right model was not available. The femur was identical apart from the geometrical reflection. Pre-wired gauges were acquired from the same source as the wireless gauges, and proved to be much easier to use. The convention used in chapter 2 of labelling  $\alpha = 0^\circ$  when the lesser trochanter is pointing down is used. The PVC left femur was sawn to 17 cm long and scanned just as the right PVC femur was in section 2.2. The distal end was set in PMMA using the method detailed in section 3.3.

#### 4.2.1.1 Load Cell Attachment

A load cell attachment was designed to to act as an acetabulum surrogate in which the femoral head can freely rotate. It had a slightly larger radius than the head to allow free movement. An object was designed in CAD software SolidWorks which could be bolted to a steel plate on the upper side and attach to the load cell,

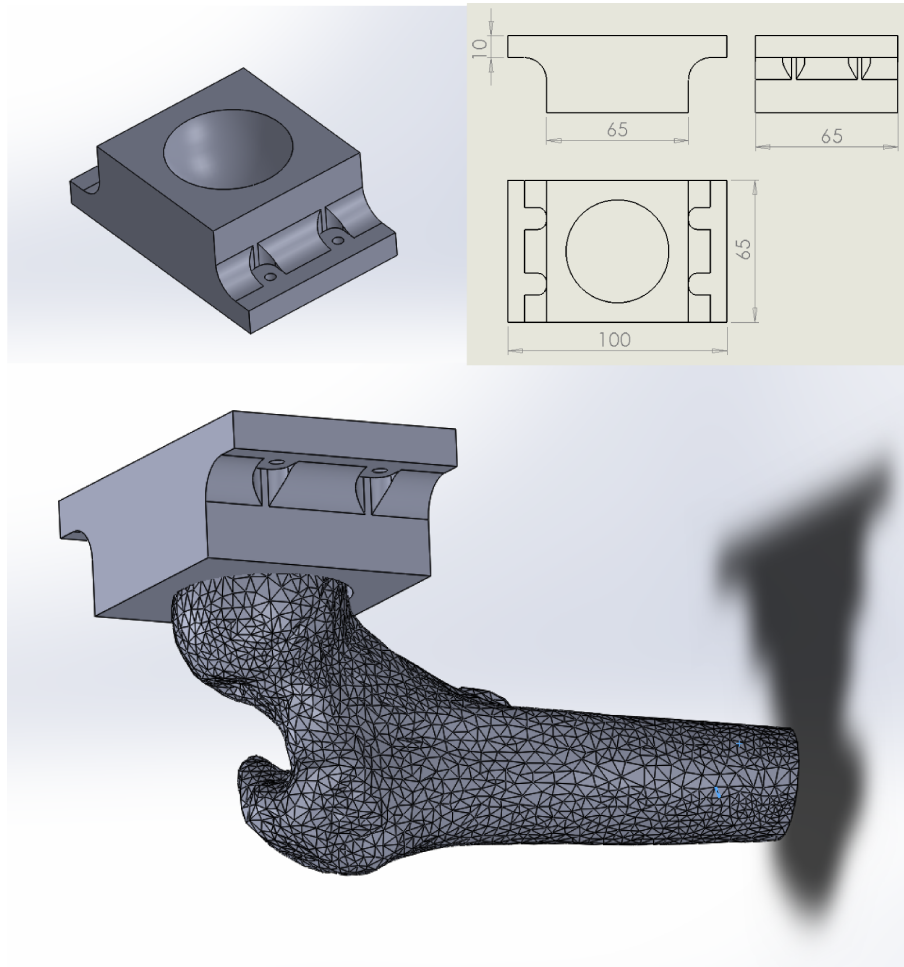


Figure 4.1: CAD drawing of load cell attachment.

and had the simulated acetabulum on the lower side, which would be the point of contact with the femur. The design of this object is shown in figure 4.1.

The STL file of the PVC proximal femur was imported into the SolidWorks environment, and a sphere was laid over the femoral head. The radius of the sphere was adjusted until it closely matched the size of the femoral head at a 23 mm radius. It is not easy to measure the dimensions of the femoral head directly as it is not a perfect sphere, so this method provided an estimate of the radius with visual confirmation of its accuracy. The femoral surface was removed and the sphere was centred 5 mm below the lower face of the object. The radius of the sphere was increased by 2 mm and the overlapping spherical sector was removed from the object. Figure 4.1 shows the 3-dimensional object in contact with the proximal femur, along with the CAD drawing showing the dimensions of the attachment.

The CAD design was manufactured with a rapid prototyping machine from acrylonitrile butadiene styrene (ABS,  $E = 2.3$  GPa,  $\nu = 0.3$  [59]). The hollow spherical surface was polished to remove the stepped surface which is an artefact of the prototyping process. Four holes were drilled into the attachment, and it was screwed onto a 2 mm thick steel plate cut to match the surface area of the upper face of the attachment. A clevis pin was welded to the steel plate so that it could be attached to the tensometer's load cell.

#### 4.2.1.2 Tower

Apparatus was designed and manufactured to support the distal end of the femur in a range of different angles, and provide an angled surface to contact the greater trochanter. The design of the apparatus can be seen in figure 4.2. A tower consisting of four threaded rods and a bracket is used to support the distal end of the femur. The bracket includes an aluminium tab resting on a pivot, which is bolted to the aluminium cylinder containing the femur. The bolt can be rotated within the tab and screwed into place, changing the angle  $\alpha$ . The pivot allows the femur to be rotated, thus altering  $\phi$ . The bracket rests on four nuts which are moved along the threaded rods to compensate for this rotation and keep the greater trochanter in contact with the surface. The tower is welded to a steel plate ( $E = 205$  GPa,  $\nu = 0.28$  [46]), which provides the contact surface for the greater trochanter. This plate is supported at an angle by two nuts on threaded rods, which are welded to a steel base plate. Changing the height of the bolts changes the angle  $\theta$  of the contact surface with respect to the load cell. A 3 mm sheet of steel was used for the angled plate to ensure that it does not bend under the force applied to the femur. The base plate is clamped to a third steel plate which is bolted to the load frame. The bolted plate and the base plate was designed to extend over the edge of the load frame to provide a point to clamp them together. This is so that the base plate can be secured to the load frame, but it can also be moved so that the femoral head lies directly below the hemispherical surface of the load cell attachment.

The method used to embed the distal end of the femur into an aluminium cylin-

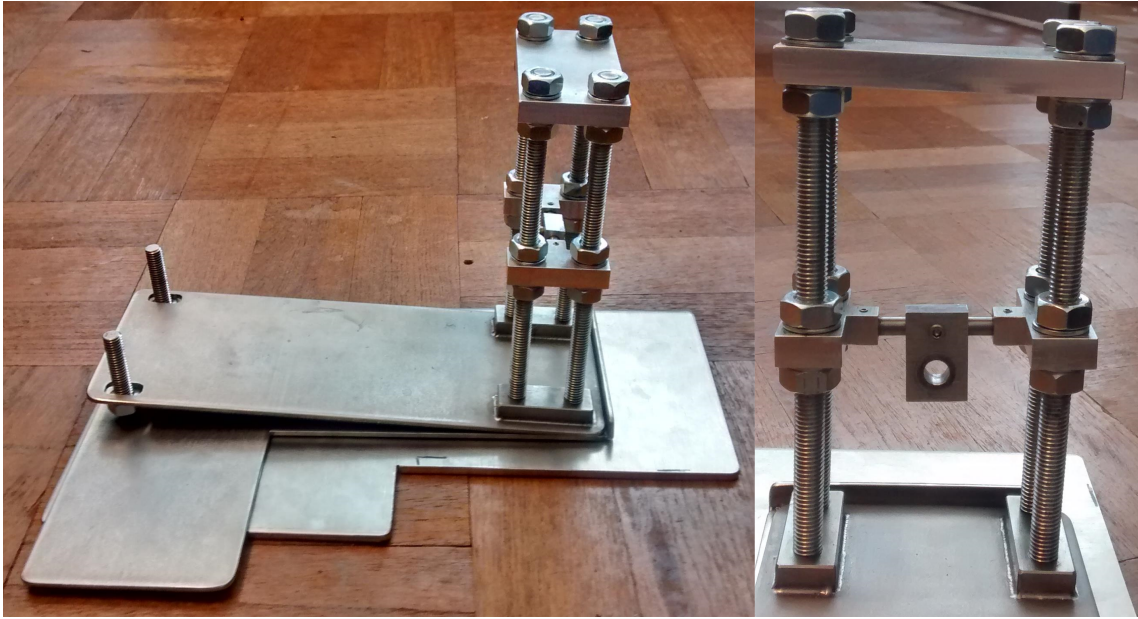


Figure 4.2: Apparatus used to support the distal end of the femur and provide an angled contact plane for the greater trochanter. The tab which is bolted onto the cylinder is visible in the right hand image.

der is described in chapter 3. The threaded hole at the closed end of the cylinder was designed to be bolted onto an aluminium tab attached to the bracket. The angle  $\phi$  could be altered by moving the distal end of the femur in the vertical axis by raising or lowering the bracket.  $\alpha$  was altered by rotating the bolt in the aluminium tab.

The femur was set to the desired orientation defined by the angles  $\alpha$ ,  $\phi$ , and  $\theta$  using a protractor and parallax. A seam artefact from the casting process running along the femoral head in the mediolateral direction was used as a reference for measuring  $\alpha$ , along with the horizontal lower face of the load cell.  $\phi$  is the angle between the axis of the cylinder and the base plate bolted to the loading frame.  $\theta$  is simply the angle between the angled plate and the base plate. Figure 4.3 shows the lines along which the angles are measured. A small source of error in the measurement of  $\alpha$  was caused by the cylinder rotating when tightening the nut holding it in place. The femur was positioned at the desired  $\alpha$  angle then the nut was tightened with a spanner.  $\alpha$  was then measured again and, if it deviated from the desired angle by more than an admissible error of  $2^\circ$ , the angle was re-set.

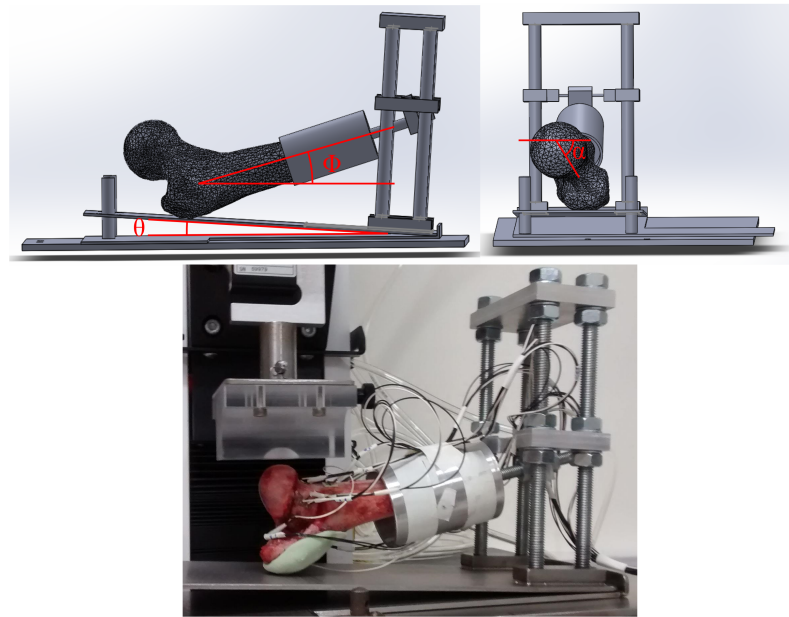


Figure 4.3: The upper two images are taken from the CAD drawing of the apparatus, and shows the angles describing the loading conditions of the femur. The right femur is shown, as this model was used in the initial design of the apparatus. The angles are the same for the left femur, but the direction of  $\alpha$  is reversed. The photograph shows the sheep's bone femur fixed into the apparatus and positioned in the loading frame beneath the load cell attachment. Exactly the same arrangement was used for the experiments with the PVC femur. The sheep's femur experiment will be discussed in the following chapter.

### 4.2.2 Measuring and Recording Strain

The strain gauge amplifier used in this experiment samples the strain at a rate of 1,000 readings per second. The data recorded in Madaq was later downsampled to 10 per second to increase the speed of data processing. This was considered a sufficiently fine time resolution to observe the strain evolution.

The tensometer was programmed to increase the load applied to the femur at a steady rate of 50 N/minute. Figure 4.4 shows a typical load vs. time graph output by Bluehill. The regression line is calculated from the readings from 15 seconds onwards. It shows a very small error of 0.006% in the gradient, indicating that the the load rate input into program is accurate.

PVC behaves elastically in response to mechanical compression, so the strain is expected to increase linearly with time. Strain per Newton can be calculated by multiplying the gradient of the strain vs. time graph by 60/(N per minute). Figure 4.5 shows a sample graph of strain plotted over time (recorded at 0.1 second inter-

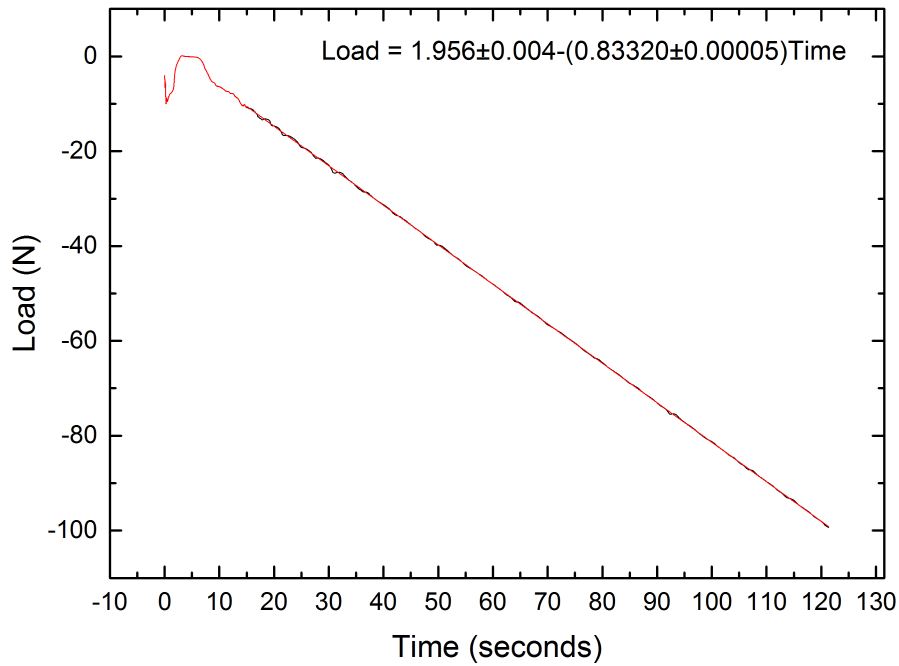


Figure 4.4: Load plotted against time output from Bluehill software. Red line shows regression line. First 15 seconds not used for regressional analysis.

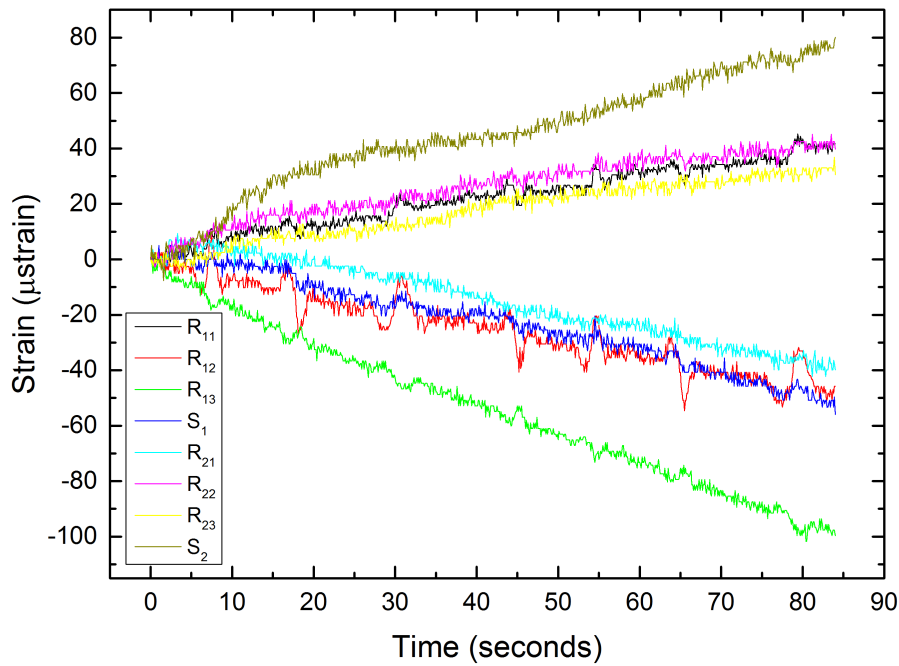


Figure 4.5: Strain plotted against time, demonstrating the linear response to load (which increases linearly with time). The data taken during the first 15 seconds were removed when calculating the gradient, as the load measurements shown in figure 4.4 indicate that the programmed load increase per second cannot be assumed for these data.

vals) measured by the eight channels connected to the six rosette component gauges and two single gauges bonded to the surface of the PVC femur, under the steadily increasing load. After an initial settling period of around 15 seconds, the change in strain is approximately linear with time. When the load cell initially makes contact with the femur, the strain appears to respond in a non-linear way with the load. This is caused by the compliance of the apparatus and can be eliminated from results when taking gradients.

Each component gauge of a tri-axial rosette requires a separate amplifier channel. A Matlab program was written to calculate the two principal strains for each rosette gauge from the gradients of the data from the three channels.

### 4.2.3 Experimental Method

The femur was tested at nine  $\alpha$  values, with the same range of  $50^\circ$  to  $130^\circ$  used in the preliminary models described in sections 2.3 and 2.4, but with an interval of  $10^\circ$  between each test. Eighteen loading configurations were used, one set with  $\phi = 10^\circ$ ,  $\theta = 5^\circ$ , another with  $\phi = 15^\circ$ ,  $\theta = 10^\circ$ . The femur will be tested under each loading condition three times and the average strain measurements will be compared with the results of the finite element model, using the standard deviation of the measurements as the experimental error. The load was increased at a rate of 50 N/minute, with an upper limit of 450 N. Loading was typically terminated once a load of 100 N was reached.

The results of the model presented in section 2.3 indicate highly strained areas on the neck of the PVC femur. The largest range in strain measurements was found in the centre of the posterior surface of the neck, followed by the superior and then the inferior surfaces. One rosette gauge and one single gauge were bonded to the centre of the posterior surface of the neck, the other rosette gauge was bonded to the superior surface of the neck, and the final single gauge was bonded to the inferior surface. The directions along which the single gauges were aligned were determined from the direction of the maximum principal strain at the corresponding point in

the preliminary model. An arrow surface was plotted on the femur showing the principal strain direction, and the gauge was bonded in approximately the same direction as the arrows in the corresponding part of the surface.

The surface was prepared and gauges were bonded to the surface, using the technique described in section 3.2. Rosette gauges were applied to the top and middle of the neck, and single gauges were applied to the lower side and middle of the neck.

### 4.3 Identification of Gauge Locations

In order to compare the results of the finite element model with the strain gauge measurement, the measurement points on the model surface must be selected to match up with the gauge locations.

Various techniques have been implemented to achieve this. Bessho et al. [14] scanned the sample with a number of epoxy resin fiducials attached to the surface. The coordinates of the fiducials were obtained from the CT scan data, and their locations were registered with a two-dimensional photograph of the sample by observation. The location of the gauges is then transformed from the two-dimensional coordinate system to the three-dimensional system of the scan data used by the finite element model. Anderson et al. [60] scanned a pelvis sample with a registration block attached to iliac crest. The block coordinates of the block are registered between the model and lab coordinates.

Trilateration is a technique used to find the coordinates of points by measurements of distances from locations with known coordinates. It is frequently used in navigation and surveying, and is not known to have been used for determining the location of strain gauges. Trilateration was used for this experiment as it requires very basic computation and apparatus and is not time consuming. In addition, no fiducials or reference objects are required for this method. As this technique has not been used for this purpose, it was assessed by investigating the effect of error

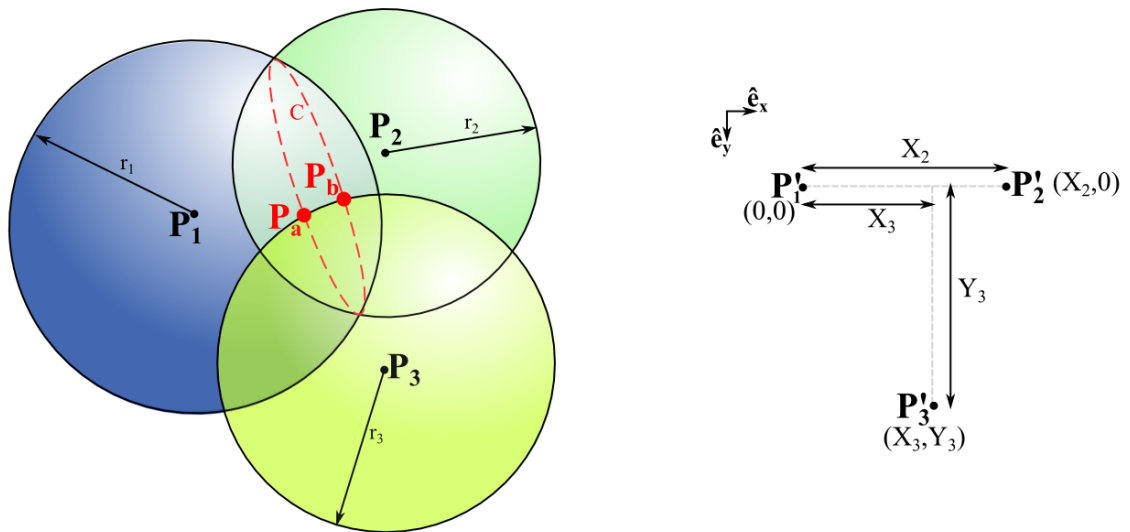


Figure 4.6: Schematic representation of the geometric problem solved in the process of three-dimensional trilateration. The three spheres are constructed at the measured radii from the corresponding reference points. The spherical surfaces around  $\mathbf{P}_1$  and  $\mathbf{P}_2$  intersect along a circle  $c$ . The third sphere intersects  $c$  in at two points,  $\mathbf{P}_a$  and  $\mathbf{P}_b$ .

in measuring distance.

### 4.3.1 Trilateration

Trilateration is a method of defining the coordinate location of a point in a three-dimensional space using its distance from three points of known location [61]. This technique was applied by measuring the distance from the gauge to three selected reference points. The reference points must be distinctive, as they must be matched by eye between the model geometry and on the surface of the sample.

Reference points were selected at the tip of the greater trochanter ( $\mathbf{P}_1$ ), the centre of the ligament pit ( $\mathbf{P}_2$ ), and at the depression in the lateral surface of the femoral head where it meets the neck ( $\mathbf{P}_3$ ). The locations of the reference points and gauge points are shown mapped onto the model geometry in figure 4.7. The distances between the gauge and each of the reference points were measured with callipers. These three distances can be seen as the radii of spheres around each reference point (figure 4.6), and are labelled  $r_1$ ,  $r_2$ , and  $r_3$ . The three spheres can intersect at one or two points, one of which is the gauge location. If they intersect in two locations, points are entered into the model geometry at these location and

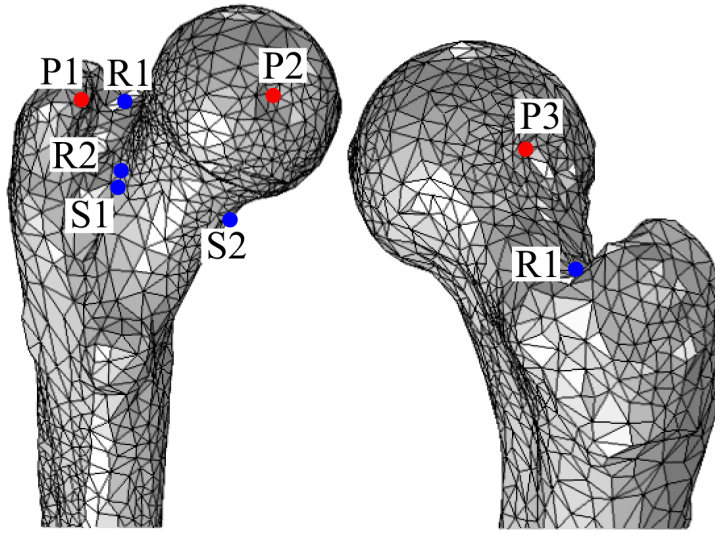


Figure 4.7: Locations in the model 3 reference points  $\mathbf{P}_1$ ,  $\mathbf{P}_2$ , and  $\mathbf{P}_3$ , and strain gauge points  $R_1$ ,  $R_2$ ,  $S_1$ , and  $S_2$ .

the point which appears to be closer to the gauge location is selected. Radii for each gauge listed in table 4.1.

radii (mm)			
	$r_1$	$r_2$	$r_3$
$R_1$	29	60	22
$R_2$	36	51	23
$S_1$	33	49	20
$S_2$	41	39	47

Table 4.1: Distances of each gauge from each of the three reference points.

A transformed coordinate system is used to find the location of the gauge point. The problem is constrained to two dimensions by considering the plane on which all three reference points,  $\mathbf{P}_1$ ,  $\mathbf{P}_2$ , and  $\mathbf{P}_3$ , lie.  $\mathbf{P}_1$  is defined as the origin, and  $\mathbf{P}_2$  lies on the  $x$ -axis. The new coordinates of the three reference points are defined as follows:

$$\mathbf{P}'_1 = [0, 0, 0] \quad (4.1a)$$

$$\mathbf{P}'_2 = [X_2, 0, 0] \quad (4.1b)$$

$$\mathbf{P}'_3 = [X_3, Y_3, 0]. \quad (4.1c)$$

The coordinates of the two points of intersection in the new coordinate system are expressed in terms of the measured radii and the coordinates of the reference points,

$$X' = \frac{r_1^2 - r_2^2 + X_2^2}{2X_2} \quad (4.2a)$$

$$Y' = \frac{r_1^2 - r_3^2 + X_3^2 + Y_3^2}{2Y_3} - \frac{X_3}{Y_3} X' \quad (4.2b)$$

$$Z' = \pm \sqrt{r_1^2 - X'^2 - Y'^2}. \quad (4.2c)$$

$X_2$  is the length of the vector between  $\mathbf{P}_1$  and  $\mathbf{P}_2$ . Expressed in the original Cartesian coordinate system the basis vector of the x-axis,  $\hat{\mathbf{e}}_x$ , is parallel to this vector.

$$X_2 = |\mathbf{P}_2 - \mathbf{P}_1| \quad (4.3a)$$

$$\hat{\mathbf{e}}_x = \frac{\mathbf{P}_2 - \mathbf{P}_1}{X_2}. \quad (4.3b)$$

$X_3$  is the length of the component of the vector between  $\mathbf{P}_1$  and  $\mathbf{P}_3$  parallel to  $\hat{\mathbf{e}}_x$ . The basis vector of the y-axis,  $\hat{\mathbf{e}}_y$ , is the perpendicular vector to  $\hat{\mathbf{e}}_x$  in the plane of the three reference points.  $Y_3$  is the length of the component of the vector between  $\mathbf{P}_1$  and  $\mathbf{P}_3$  parallel to  $\hat{\mathbf{e}}_y$ . The third basis vector,  $\hat{\mathbf{e}}_z$ , is perpendicular to both  $\hat{\mathbf{e}}_x$  and  $\hat{\mathbf{e}}_y$ .

$$X_3 = \hat{\mathbf{e}}_x \cdot (\mathbf{P}_3 - \mathbf{P}_1) \quad (4.4a)$$

$$\hat{\mathbf{e}}_y = \frac{\mathbf{P}_3 - \mathbf{P}_1 - X_3 \hat{\mathbf{e}}_x}{|\mathbf{P}_3 - \mathbf{P}_1 - X_3 \hat{\mathbf{e}}_x|} \quad (4.4b)$$

$$Y_3 = \hat{\mathbf{e}}_y \cdot (\mathbf{P}_3 - \mathbf{P}_1) \quad (4.4c)$$

$$\hat{\mathbf{e}}_z = \hat{\mathbf{e}}_x \times \hat{\mathbf{e}}_y. \quad (4.4d)$$

$X_2$ ,  $X_3$ , and  $Y_3$  are used in equations 4.2a, 4.2b, and 4.2c to calculate the coordinates of the points of intersection in the new coordinate system. These coordinates may now be transformed back to the original Cartesian coordinate system using the following equation:

$$\mathbf{P}_{a,b} = \mathbf{P}_1 + X' \hat{\mathbf{e}}_x + Y' \hat{\mathbf{e}}_y + Z' \hat{\mathbf{e}}_z. \quad (4.5)$$

Points were placed at the two solutions of equation 4.5 for each gauge, and the

point which appeared to match the gauge point was selected. The nearest node on the surface of the femur was then used as the sample point for that gauge.

### 4.3.2 Analysis of Errors in Gauge Location Measurement

The calliper measurements have an estimated error of 0.5 mm. The effect that this error have on the decision of which node is selected as the gauge point was assessed. The trilateration calculation was performed with 0.5 mm added to or subtracted from one, two, or three of the radii measured for the first rosette gauge. The original radii are  $r_1 = 29$ ,  $r_2 = 60$ , and  $r_3 = 22$ . Table 4.2 contains the distance from points calculated with each of these altered radii and the node originally chosen as the gauge point.

$r_3 - 0.5$	$r_1 - 0.5$	$r_1$	$r_1 + 0.5$
$r_2 - 0.5$	1.046543417	0.537913477	1.755132113
$r_2$	2.527498844	1.165965692	0.870980576
$r_2 + 0.5$	4.243478157	2.688449981	1.508354391

$r_3$	$r_1 - 0.5$	$r_1$	$r_1 + 0.5$
$r_2 - 0.5$	0.97143007	0.474724775	1.735748679
$r_2$	2.391683263	0.970006538	0.665570292
$r_2 + 0.5$	4.060192518	2.499531005	1.253745173

$r_3 + 0.5$	$r_1 - 0.5$	$r_1$	$r_1 + 0.5$
$r_2 - 0.5$	1.196342538	0.867874085	1.871299981
$r_2$	2.401468605	1.080475355	0.850605725
$r_2 + 0.5$	3.975501101	2.448113834	1.233319674

Table 4.2: Distance from selected gauge node in mm of points with deviations of  $\pm 0.5$  mm from the original measurements of one, two, or three radii.

The average distance between the originally chosen gauge point node and each of its nearest neighbouring nodes is 5.267184 mm. The distance between the solution to the trilateration calculation and the originally selected node would have to be less than half of this distance to ensure that the original node was selected and not one of its nearest neighbours. Four of the 27 calculated differences exceed this distance. This means that they may result in the selection of a different node from

the original, although this is not guaranteed. All potential gauge point nodes are found on the surface of the femur, but the solutions to the trilateration calculation are not constrained to the surface. Only the component of the distance between the node and the solution parallel to the surface has an effect on the choice of the gauge point node. This means that a lower limit of 22 out of 26 of the tested radii (not including the original measurements of  $r_1$ ,  $r_2$ , and  $r_3$ ) result in the same node selection as the original measurements. Because of this, this technique was considered sufficiently reliable to be used for the selection of gauge point nodes in this experiment.

The use of a more accurate method of measuring distance than callipers would result in a smaller error in the measurement of the radii. The same test was carried out with a radius measurement error of 0.25 mm. The distances between the originally selected node and the solutions for each of the 27 configurations are listed in table 4.3. None of the differences exceed the limit of half of the average distance between the originally chosen node and each of its nearest neighbours. If the error in measuring the radii could be reduced to 0.25 mm, the error due to measurement could be considered to have no effect on the selection of the gauge point node.

$r_3 - 0.5$	$r_1 - 0.5$	$r_1$	$r_1 + 0.5$
$r_2 - 0.5$	0.961769783	0.338839188	0.525516496
$r_2$	1.706978957	1.033983707	0.553078768
$r_2 + 0.5$	2.494342638	1.785106424	1.172099242
$r_3$	$r_1 - 0.5$	$r_1$	$r_1 + 0.5$
$r_2 - 0.5$	0.929608976	0.285274105	0.506548046
$r_2$	1.654918769	0.970006538	0.455203825
$r_2 + 0.5$	2.429411548	1.714414112	1.084463855
$r_3 + 0.5$	$r_1 - 0.5$	$r_1$	$r_1 + 0.5$
$r_2 - 0.5$	0.981727573	0.449347243	0.620848782
$r_2$	1.653130446	0.98687954	0.512984691
$r_2 + 0.5$	2.400477196	1.691736994	1.067899104

Table 4.3: Distance from selected gauge node in mm of points with deviations of  $\pm 0.25$  mm from the original measurements of one, two, or three radii.

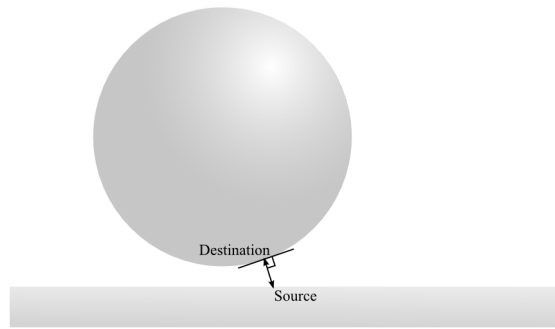


Figure 4.8: Contact. Most convex object is labelled “destination”, most concave labelled and “source”. Force acts between point on destination boundary and closest point on destination boundary in the perpendicular direction.

## 4.4 Model

The results of the experiment were compared with analogous results of a finite element model. This model was based on the one presented in section 2.3, but with the inclusion of contact mechanics to more closely match the conditions of the experiment designed in this chapter.

### 4.4.1 Contact Physics

#### 4.4.1.1 Comsol

The surfaces of the femoral head and greater trochanter are irregular and it is not easy to predict the contact area or the distribution of contact pressure [62]. It is preferable to apply load by modelling the contact forces in the hip joint, as well as between the greater trochanter, rather than applying conditions to individual boundaries as was done in section 2.3.

Comsol can model the contact between two groups of boundaries. One group is labelled “source” and the other “destination”, as shown in figure 4.8. Ideally, the boundaries belonging to the object with the greater Young’s modulus should be designated the source, and the source should concave and the destination convex. The destination boundaries should have a finer mesh than the source [63].

Real contact problems are non-continuous, the force between the two objects is

only present when they touch. A finite element treatment must make the problem continuous in order to reach a converged solution. A small overlap between the contact surfaces is allowed. The source boundaries are allowed to penetrate the destination boundaries but not vice versa. The distance between each destination point and its corresponding source point,  $d_g$ , is positive when the objects are not touching and negative when they overlap. The penalised contact pressure has a form which increases exponentially as  $d_g$  decreases when the boundaries are not touching, and linear when there is overlap. It is constrained so that it is continuous between these two conditions:

$$T_{np} = \begin{cases} T_n - P_n d_g & \text{if } d_g \leq 0 \\ T_n e^{-\frac{P_n d_g}{T_n}} & \text{otherwise.} \end{cases} \quad (4.6)$$

#### 4.4.1.2 Hertzian Contact

Comsol's augmented Lagrangian contact model requires the user to input an estimate for the contact pressure between the source and destination boundaries. It is not easy to directly calculate the contact pressure for the irregular surface of the femur, but it is possible to use similar, regular shapes to estimate the pressure. The pressure on the contact surfaces between curved objects can be calculated from Hertzian contact stress theory. This theory is concerned with contact between elastic solids in non-adhesive contact [64, p.84]. By calculating the pressure between similar shapes, an approximation of the pressures present between the contact surfaces in the model can be obtained.

The solution to Hertzian contact stress problem applies to a system where the surfaces are frictionless and non-conforming, so that the initial contact area is negligibly small with respect to the rest of the surface area of the object. An applied load brings the objects together, causing deformation at the contact point and causing the contact area to become finite.

The hip joint is a ball-and-socket joint, so it can be modelled as a sphere (diameter  $D_1$ ) in a hemispherical cup ( $D_2$ ), as shown in figure 4.9a. The mechanics of this

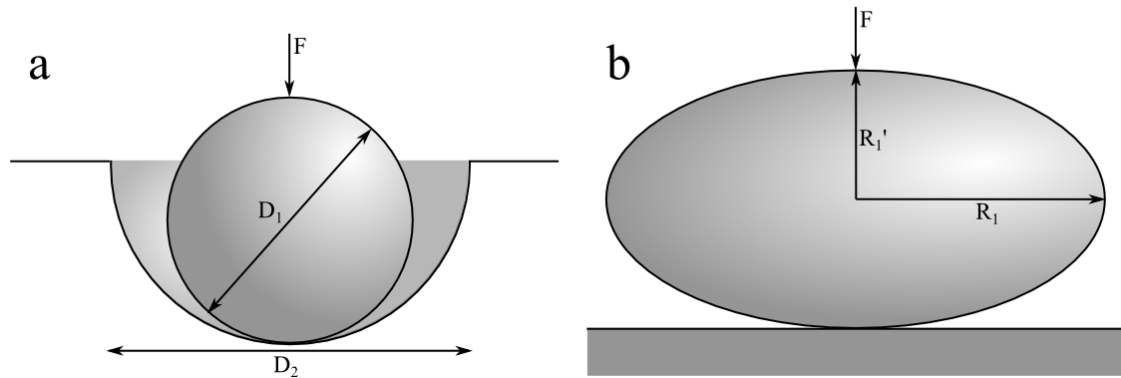


Figure 4.9: Contact pressure is calculated between regular shapes to provide an estimate of pressures between a) femoral head and acetabulum (sphere and cup), and b) greater trochanter and base plate (ellipsoid and plane).

problem are simply defined [65, p.702]. The effective radius of curvature is defined as:

$$K_D = \frac{D_1 D_2}{D_1 - D_2}. \quad (4.7)$$

The effective modulus of elasticity is a function of the Young's moduli and the Poisson's ratios of the two objects:

$$C_E = \frac{1 - \nu_1^2}{E_1} - \frac{1 - \nu_2^2}{E_2}. \quad (4.8)$$

The radius of the circular contact area between the two surfaces once loaded,  $a$ , is defined by:

$$a = 0.721 \sqrt[3]{PK_D C_E}. \quad (4.9)$$

The contact pressure is given by the following equation:

$$(\sigma_c)_{max} = \frac{1.5P}{\pi a^2}. \quad (4.10)$$

The contact pressure induced between a 23 mm sphere and a 25 mm socket with a load of 1 N, with the material properties of PVC and ABS already reported, is calculated as 1.7 MPa.

The contact pairing of the greater trochanter and the flat base plate can be reasonably well defined as an ellipsoid and an infinite plane (figure 4.9b) [65, p.704].

In this case, the radius of curvature is defined by the semiaxes of the ellipsoid

$$K_D = \frac{1.5}{1/R_1 + 1/R'_1}. \quad (4.11)$$

Three variables,  $\alpha$ ,  $\beta$ , and  $\gamma$ , are taken from a table of values, and are determined from another variable,  $\theta$  [65, p.704]:

$$\cos \theta = \frac{K_D}{1.5} \sqrt{\left(\frac{1}{R'_1} - \frac{1}{R_1}\right)^2}. \quad (4.12)$$

$\alpha$ ,  $\beta$ , and  $\gamma$  are used to calculate  $c$  and  $d$ , the semiaxes of the elliptical contact area.

$$c = \alpha \sqrt[3]{PK_D C_E} \quad (4.13a)$$

$$d = \beta \sqrt[3]{PK_D C_E}. \quad (4.13b)$$

The contact pressure is calculated from the contact area in much the same way as in equation 4.10

$$(\sigma_c)_{max} = \frac{1.5P}{\pi cd}. \quad (4.14)$$

The appropriate size of the ellipsoid which represents the greater trochanter was determined in a similar way to the spherical representation of the head, by laying an ellipsoid over the femur in Solidworks and altering the dimensions until the match was considered acceptable. The semiaxes of the ellipse were  $R_1 = 25$  mm and  $R'_1 = 30$  mm. The calculated contact pressure for these dimensions along with the material properties of PVC and steel was 13.75 MPa.

#### 4.4.2 Model Design

A finite element model was then created using the same procedure used for the preliminary model described in section 2.3, but with the application of the forces through contact with objects rather than fixed and load boundaries. Figure 4.10 shows the model geometry. A flat floor represented by a  $70 \times 40 \times 5$  mm steel block, and load cell attachment is represented by an ABS block. The load cell attachment geometry consists of a  $65 \times 65 \times 28$  mm cuboid with 25 mm radius spherical segment removed from the lower surface to mimic the design of the real load cell

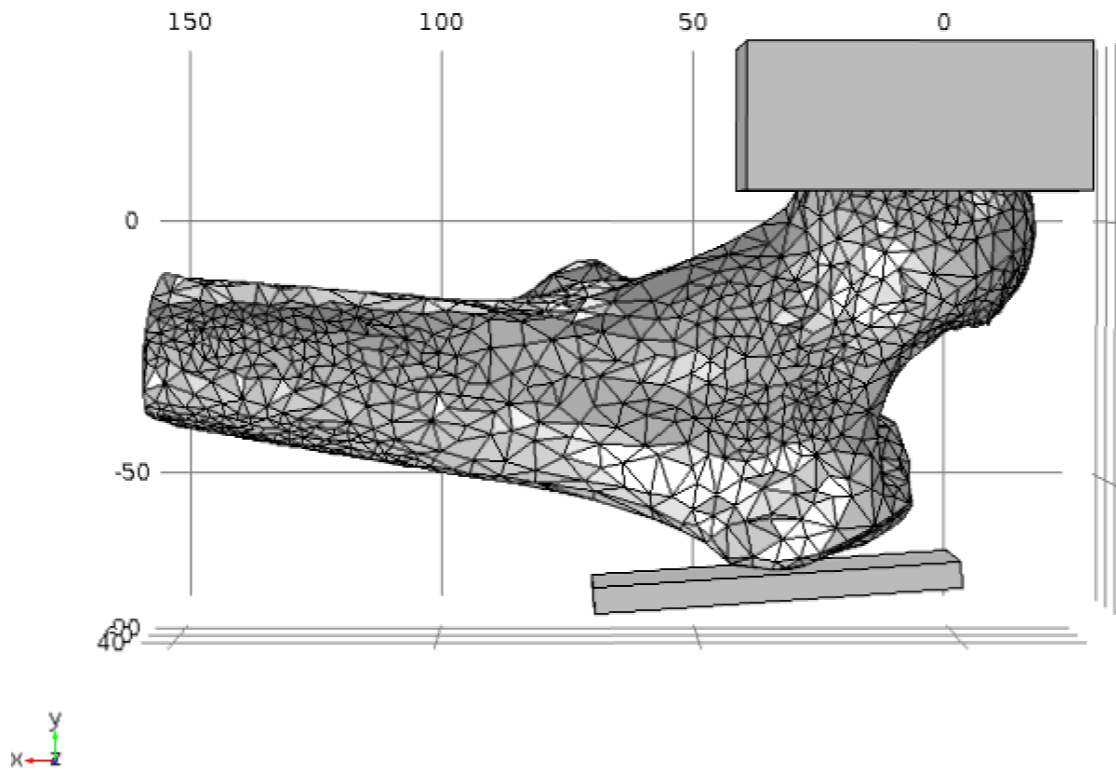


Figure 4.10: Geometry of the PVC femur finite element model, including the imported femur geometry and the load cell attachment and floor block drawn in the Comsol environment.

fitting described in section 4.2.1.1. The attachment was fixed in space and the femur translated so that the femoral head was in contact with the hemispherical surface.

Two contact pairs were set up, one between the femoral head (source) and the load cell attachment (destination), and another between the floor block (source) and the greater trochanter (destination). The contact pressure between each contact pair was set to the values calculated from equations 4.10 and 4.14.

The femur was set to revolve around a point at the centre of the femoral head, chosen by selecting the centre of the sphere removed from the attachment block.  $\alpha$  and  $\phi$  can be changed without breaking the contact between the femur and the attachment. The floor block was revolved around the  $z$ -axis to change  $\theta$ . The floor block was manually translated to bring it into contact with the greater trochanter for each loading condition once the angles have been set. Contact surfaces chosen are shown in figure 4.11.

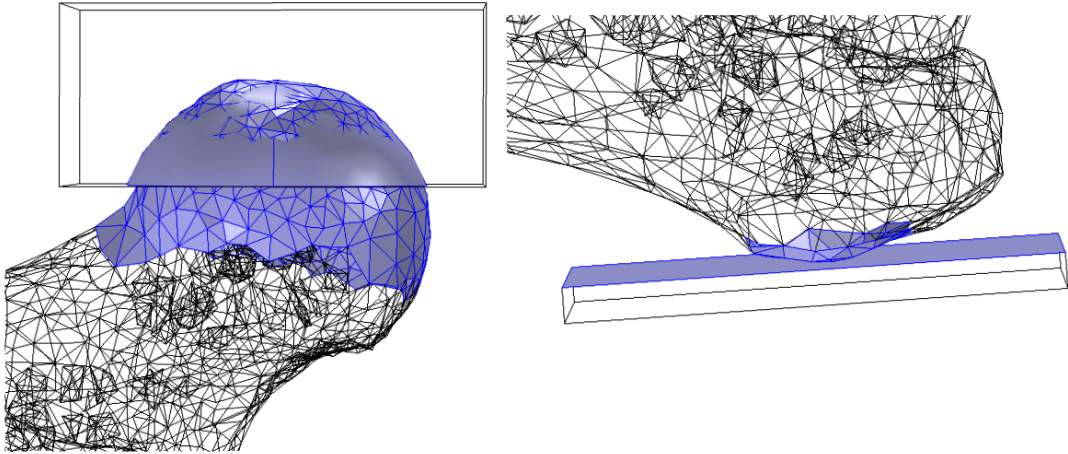


Figure 4.11: Surface boundaries where the contact force was applied.

Boundaries at the distal end were fixed exactly as described in section 2.3. The base of the floor block (the face opposite to the face in contact with the femur) was set as a fixed boundary. It is easier to achieve a stable solution in a finite element contact problem if load is applied via a prescribed displacement rather than a boundary load. A displacement of  $1 \times 10^{-8}$  mm was applied to the upper surface of the load cell attachment. A prescribed displacement of  $1 \times 10^{-8}$  was applied to the top face of the load cell fitting along the  $y$ -axis, towards the floor block, and the face was constrained to not move along the  $x$ - and  $z$ -axes. In order to calculate the strain per newton, all resultant strains were divided by the total stress integrated across this surface.

### 4.4.3 Calculating Strains in the Model

#### 4.4.3.1 Strain Direction in Single Gauges

The model is solved in a three-dimensional environment, providing three principal strains. The strains measured with the rosette strain gauges only calculate two. The second principal strain calculated from the gauge data corresponds with the third principal strain calculated by the the model.

The calculation of principal strains at the rosette strain gauge points in the

Comsol model does not depend on the orientation of the gauge at that point. The strain measured with a single gauge does depend on the orientation of the gauge. A coordinate frame was generated in Comsol with two components tangential to the surface of the object, one component normal to the surface. The strain in the direction of the gauge can be calculated using the strain calculated along one of the tangential components and the angle between this component and the gauge axis.

The vector representing the gauge axis in the Cartesian frame,  $\mathbf{g}$ , is determined from the line between the gauge point and the nearest neighbouring point in roughly the direction of the gauge. The position of the femur differs between loading conditions because it is rotated with respect to the stationary load cell attachment, so  $\mathbf{g}$  is calculated separately for each loading configuration. The unit vector of the gauge direction is the normalised vector between the coordinates of these two points. The unit vector of the first component of the new coordinate system at the gauge point,  $\mathbf{t}_1$ , is calculated by Comsol. The scalar product of the two unit vectors is equal to the cosine of the angle between them. The sine of the angle is given by the magnitude of the vector product of the unit vectors. The 2-argument arctangent function of the ratio of these two numbers gives the angle between the vectors in the interval  $-\pi \leq \theta \leq \pi$ .

In order to calculate the strains in the new coordinate system,  $\boldsymbol{\varepsilon}'$ , the strain tensor in the original Cartesian system,  $\boldsymbol{\varepsilon}$ , must be transformed using the transformation matrices calculated by Comsol,  $\mathbf{T}$ .

$$\begin{pmatrix} T_{11} & T_{12} & T_{13} \\ T_{21} & T_{22} & T_{23} \\ T_{31} & T_{32} & T_{33} \end{pmatrix} \begin{pmatrix} \varepsilon_{11} & \varepsilon_{12} & \varepsilon_{13} \\ \varepsilon_{21} & \varepsilon_{22} & \varepsilon_{23} \\ \varepsilon_{31} & \varepsilon_{32} & \varepsilon_{33} \end{pmatrix} \begin{pmatrix} T_{11} & T_{21} & T_{31} \\ T_{12} & T_{22} & T_{32} \\ T_{13} & T_{23} & T_{33} \end{pmatrix} = \begin{pmatrix} \varepsilon'_{11} & \varepsilon'_{12} & \varepsilon'_{13} \\ \varepsilon'_{21} & \varepsilon'_{22} & \varepsilon'_{23} \\ \varepsilon'_{31} & \varepsilon'_{32} & \varepsilon'_{33} \end{pmatrix} \quad (4.15)$$

All components of  $\boldsymbol{\varepsilon}'$  involving strain normal to the surface are ignored, as the strain gauges can only measure strain tangential to surface. The strain tensor is symmetrical, so  $\varepsilon'_{21} = \varepsilon'_{12}$ . Only three components of the tensor need to be considered,  $\varepsilon'_{11}$ ,  $\varepsilon'_{12}$ , and  $\varepsilon'_{22}$ .

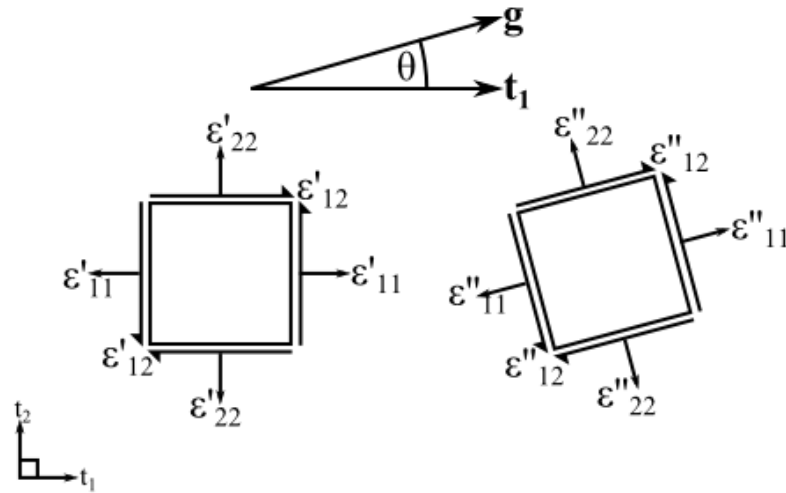


Figure 4.12: The surface strain tensor  $\boldsymbol{\varepsilon}'$  calculated in the boundary coordinate system is rotated to give  $\boldsymbol{\varepsilon}''$ , the 2-dimensional strain tensor in plane with the surface and with one component,  $\varepsilon''_{11} = \varepsilon_{\text{gauge}}$ , parallel with the gauge. Anti-clockwise rotation (from  $\mathbf{t}_1$  to  $\mathbf{g}$ ) is positive.

The angle  $\theta$  between  $\mathbf{t}_1$  and  $\mathbf{g}$  is calculated from their scalar product. A clockwise angle is defined as positive according to the right-hand rule. The vector product of the two unit vectors is used to determine whether  $\theta$  is positive ( $\mathbf{t}_1 \times \boldsymbol{\varepsilon}' > 0$ ) or negative ( $\mathbf{t}_1 \times \boldsymbol{\varepsilon}' < 0$ ). Figure 4.12 shows how the surface strain tensor is rotated to determine the strain in the direction of the gauge. The equation for strain rotation is used to calculate the strain in the gauge direction [65, p.24],

$$\varepsilon_{\text{gauge}} = \frac{\varepsilon'_{11} - \varepsilon'_{22}}{2} + \frac{\varepsilon'_{11} - \varepsilon'_{22}}{2} \cos(2\theta) + \varepsilon'_{12} \sin(2\theta). \quad (4.16)$$

#### 4.4.3.2 Strain Direction in Rosette Gauges

Another variable which can be compared between the model and the experimental results is the orientation of the principal strains. The angle  $\beta$  between the first principal strain and  $\varepsilon_1$ , the first gauge component, was determined from the results of the simulation and the experiment and compared.  $\beta$  is determined from strain gauge data with the following equation [52]:

$$\tan(2\beta) = \frac{(\varepsilon_2 - \varepsilon_3) - (\varepsilon_1 - \varepsilon_2)}{\varepsilon_1 - \varepsilon_3}. \quad (4.17)$$

To determine  $\beta$  from the model results, the unit vector representing the orientation of the gauge component must be identified. This was done by taking the coordinates

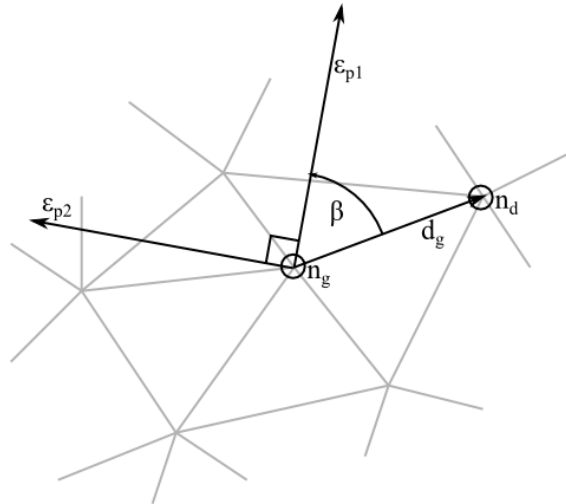


Figure 4.13: Determination of  $\beta$  in the model.  $\beta$  is the angle between gauge direction vector  $d_g$  and the first principal strain  $\varepsilon_{p1}$ .

of a node adjacent to the gauge node, using the method explained in section 4.4.3.1 to determine the gauge direction vector. The direction of the first principal strain,  $\varepsilon_{p1}$ , is calculated in Comsol, and  $\beta$  is the angle between  $\varepsilon_1$  and  $\varepsilon_{p1}$ . Figure 4.13 shows the geometry of this problem.

## 4.5 Results

Figures 4.14-4.19 show the mean value of each group of three strains per Newton measurements taken for each loading condition, plotted against the angle  $\alpha$  for each combination of  $\phi$  and  $\theta$ . The error bars represent the standard deviation of each group.

Figures 4.14 and 4.15 show the first and second principal strains per Newton at the first rosette gauge point. The second principal strain is larger than the first for all loading conditions, so this point is always in compression. Compressive strain at this point is largest here at low angles.

Figures 4.16 and 4.17 show that the second rosette gauge point is in compression at low angles, and switches to extension at some angle between  $\alpha = 90^\circ$  and  $100^\circ$  in both cases when  $\phi = 10^\circ$ ,  $\theta = 4^\circ$  and  $\phi = 5^\circ$ ,  $\theta = 9^\circ$ . The strain is largest at the higher and lower extremes of  $\alpha$ .

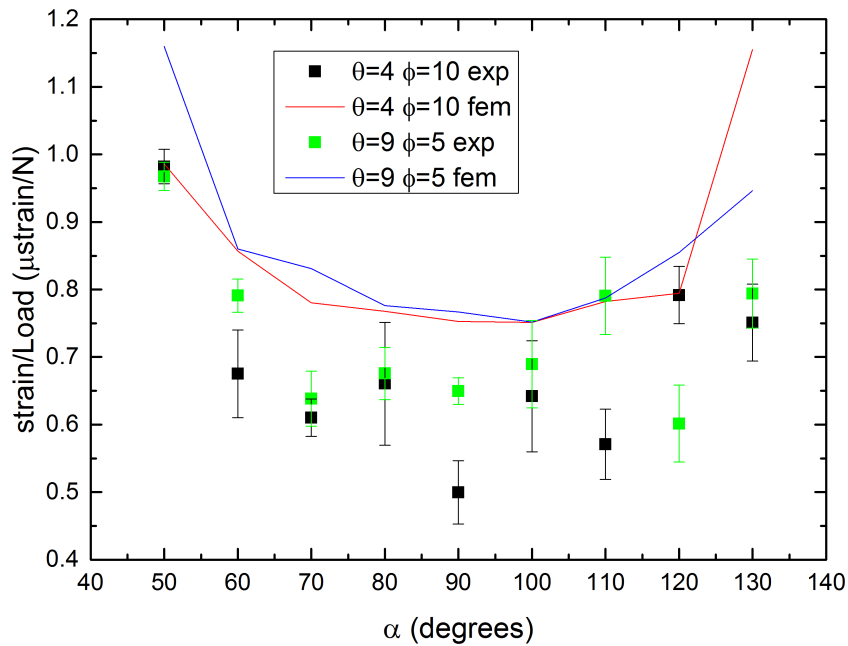


Figure 4.14: First principal strain at rosette gauge point  $R_1$ . Correspondence between model and experimental results is good for both  $\phi - \theta$  configurations. Experimental results show largest positive strains at extreme high and low  $\alpha$  angles.

The strain measured at the first single gauge point (figure 4.18) is compression for low angles and switches to extension for higher angles between  $90^\circ$  and  $100^\circ$  for  $\phi = 10^\circ$ ,  $\theta = 4^\circ$  and between  $100^\circ$  and  $110^\circ$  for  $\phi = 5^\circ$ ,  $\theta = 9^\circ$ . Again, the strain is largest at the extremes of  $\alpha$ . The strain measured at the second single gauge point (figure 4.19) is in extension for low alpha and becomes compressed at high alpha, switching between  $100^\circ$  and  $110^\circ$  for  $\phi = 10^\circ$ ,  $\theta = 4^\circ$  and  $110^\circ$  and  $120^\circ$  for  $\phi = 5^\circ$ ,  $\theta = 9^\circ$ . The largest strains found at low  $\alpha$ .

Principal strains are the largest measurable strain at a certain point. The experimentally measured principal strains measured at the first gauge point, on the superior surface of the neck of the femur, were lowest at low  $\alpha$  angles. At low  $\alpha$  the femur is rotated so that the posterior side of the bone is angled towards the floor. The largest principal strains measured at the centre of the posterior surface of the neck, at the second gauge point, were recorded at both high and low extremes of  $\alpha$ .

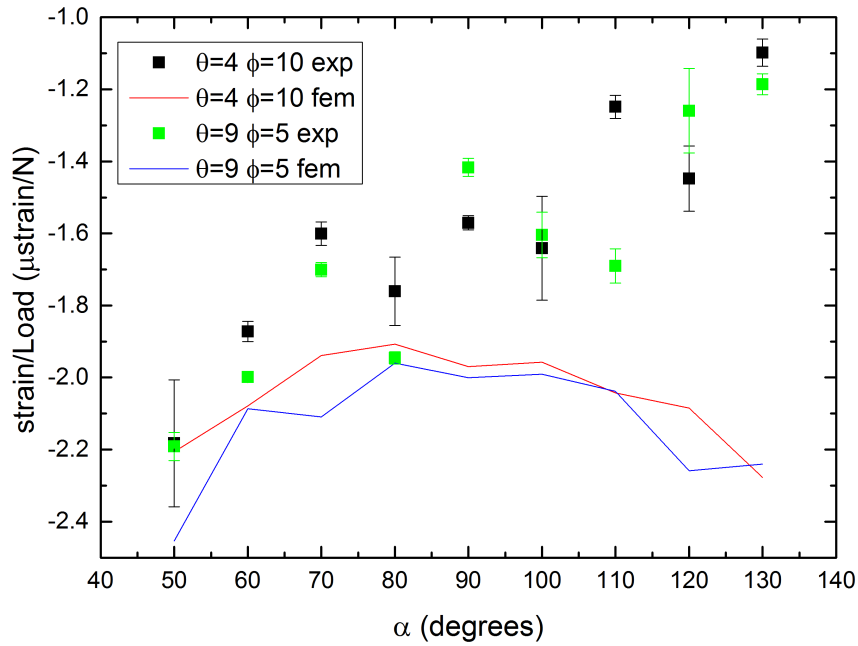


Figure 4.15: Second principal strain at rosette gauge point  $R_1$ . Good correspondence between model and experimental results at low  $\alpha$  angles, deviation begins at  $90^\circ$  degrees for both  $\phi - \theta$  configurations. Experimental results show largest negative strains at low  $\alpha$  angles.

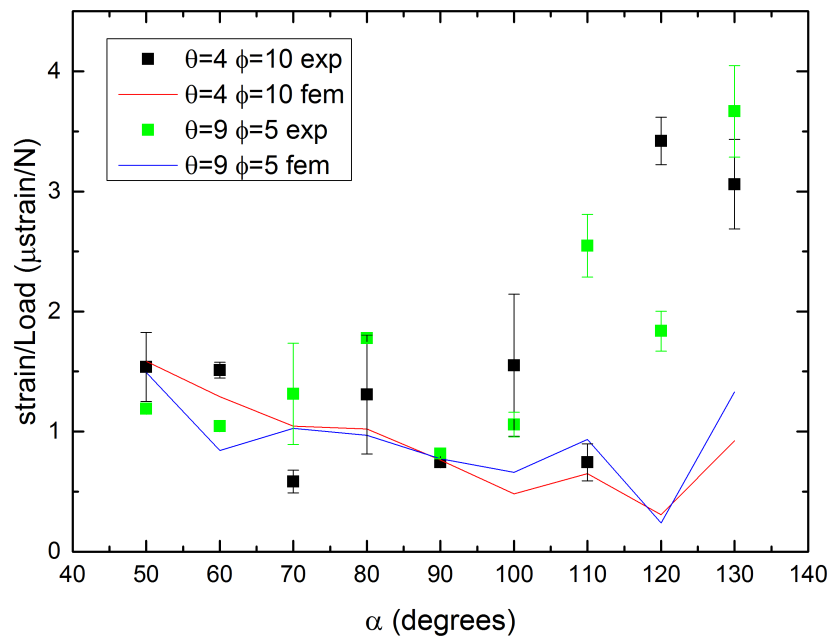


Figure 4.16: First principal strain at rosette gauge point  $R_2$ . Good correspondence between model and experimental results at low  $\alpha$  angles, deviation starts at  $110^\circ$  for  $\phi = 5^\circ, \theta = 9^\circ, 120^\circ$  for  $\phi = 10^\circ, \theta = 4^\circ$ . Experimental data show largest positive strain at high  $\alpha$  angles

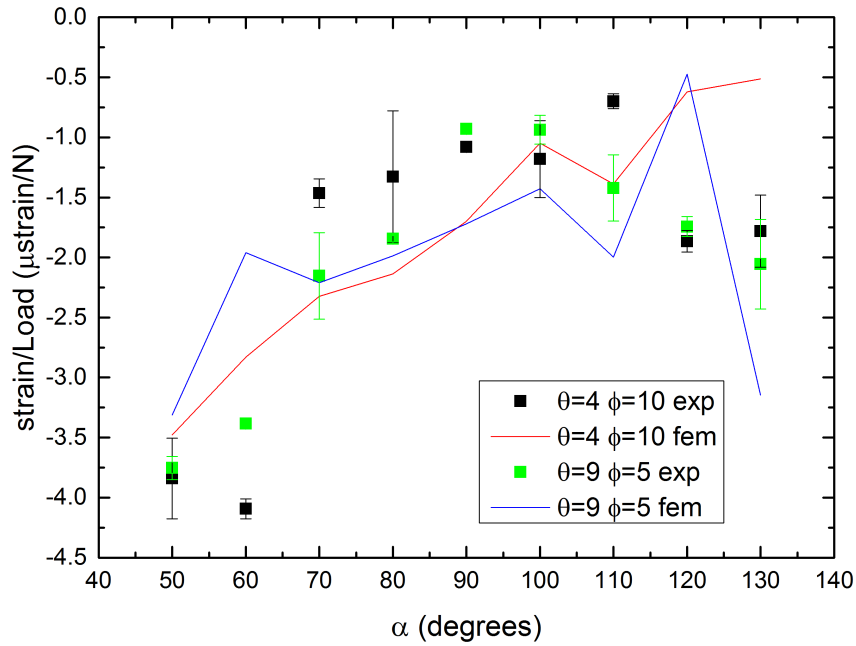


Figure 4.17: Second principal strain at rosette gauge point  $R_2$ . Good correspondence between model and experimental results for both  $\phi - \theta$  configurations. Experimental data show largest negative strain at low  $\alpha$  angles.

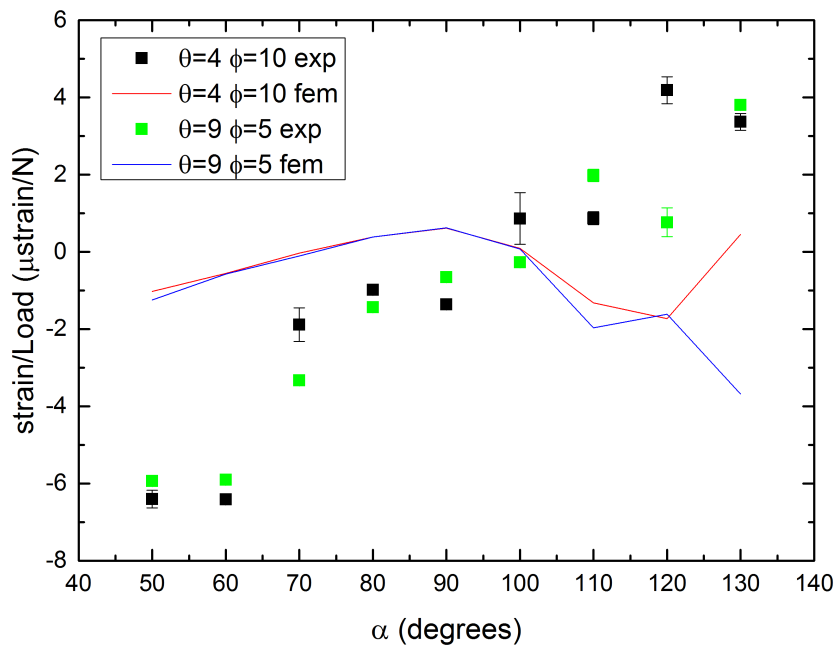


Figure 4.18: Strain at single gauge point  $S_1$ . The agreement between model and experimental results is visibly poor. Experimental data show highest negative strains at low  $\alpha$  angles, and highest positive strains at high  $\alpha$ .

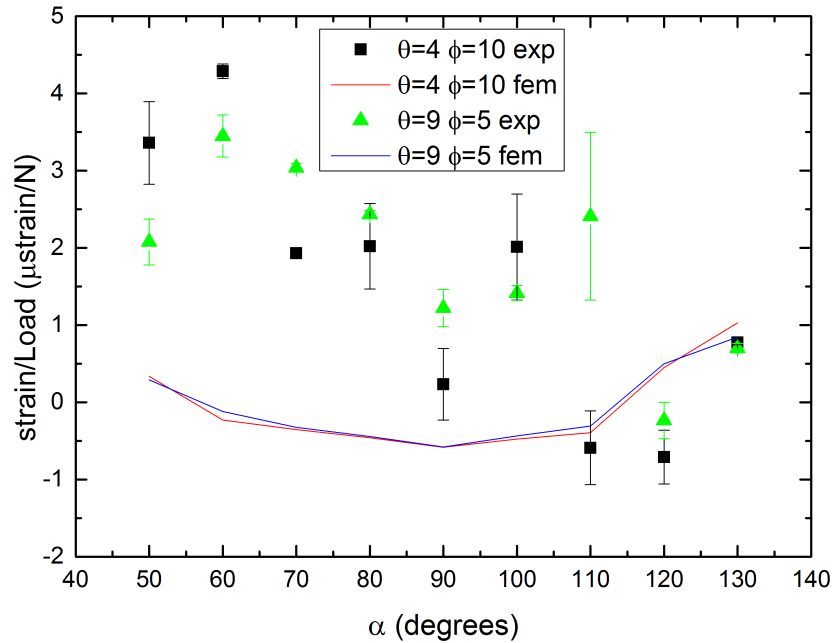


Figure 4.19: Strain at single gauge point  $S_2$ . As with the results from the  $S_1$  gauge, the agreement between model and experimental results is poor. Experimental data show highest positive strains at low  $\alpha$  angles, and switches to negative once  $\alpha$  exceeds  $100^\circ$  ( $\phi = 10^\circ$ ,  $\theta = 4^\circ$ ) and  $110^\circ$  ( $\phi = 5^\circ$ ,  $\theta = 9^\circ$ )

The results of the finite element model for the first principal strain measured at the first gauge point follows a similar path as the experimental data data, although most of the model results are larger (figure 4.14). The same is the case for the second principal strain at this point (figure 4.15) for angles below  $\alpha = 90^\circ$ , above which point the magnitude of the finite element results increase and the experimental results decrease.

The finite element and experimental results for the first principal strain measured at the second gauge point is similar for  $50^\circ \leq \alpha \leq 90^\circ$ . Above  $90^\circ$ , the results diverge, with the experimental results increasing with  $\alpha$  at a much higher rate. The results for the second principal strain at the second gauge point appear to match fairly well. The agreement between the data sets for each of the single gauges (figures 4.18 and 4.19) is not good.

The range of strains calculated from the model over the range of  $\alpha$  angles for one  $\theta$  and  $\phi$  pairing is, in general, larger than the difference between strains calculated

for each  $\theta$  and  $\phi$  for a single  $\alpha$  value. For example, the range in first strain calculated at the first gauge point when  $\theta = 10^\circ$  and  $\phi = 4^\circ$  is  $\pm 0.40395 \mu\text{strain N}^{-1}$ , whereas the largest difference between first principal strains for a given alpha at this point is  $\pm 0.20916 \mu\text{strain N}^{-1}$ . This is also true of the experimental data, and in many cases the error bars overlap. Altering  $\phi$  and  $\theta$  in this case does not provide a significantly more varied data set when compared to just changing  $\alpha$  for one  $\phi$  and  $\theta$  setting.

The second principal strain measured at the first gauge point, and both principal strains measured at the second gauge point, all show much better agreement between the model and experiment at low angles than at high. It could be the case that, at the higher angles, the conditions of the model begin to differ from the experiment.

There is a significant amount of variation in the experimental data, some error bars are quite large and the data sets are not as smooth as the model. There is clearly a discrepancy between the model and experimental data, but the scatter in the experimental data makes it difficult to observe the extent of this discrepancy. Some potential causes of discrepancy between the model and the experiment, and variation within the experimental results, have been identified.

Figure 4.20 shows the angle between the first gauge component of the rosette gauges and the direction of the first principal strain, calculated for both the experimental and model data using the methods described in section 4.4.3.2. Although there is some difference between values for this variable calculated from the experimental and model data, the significant deviations between data sets seen in in figures 4.15 and 4.16 are not present here. This indicates that inconsistencies between the loading conditions of the model and experiment are considerably more consequential on the size of the principal strains than on their direction.

The contact physics incorporated into the model does not include friction between the surfaces, although there will be some friction present in the experiment. This could cause a difference in the magnitude and distribution of the strain induced in the femur.

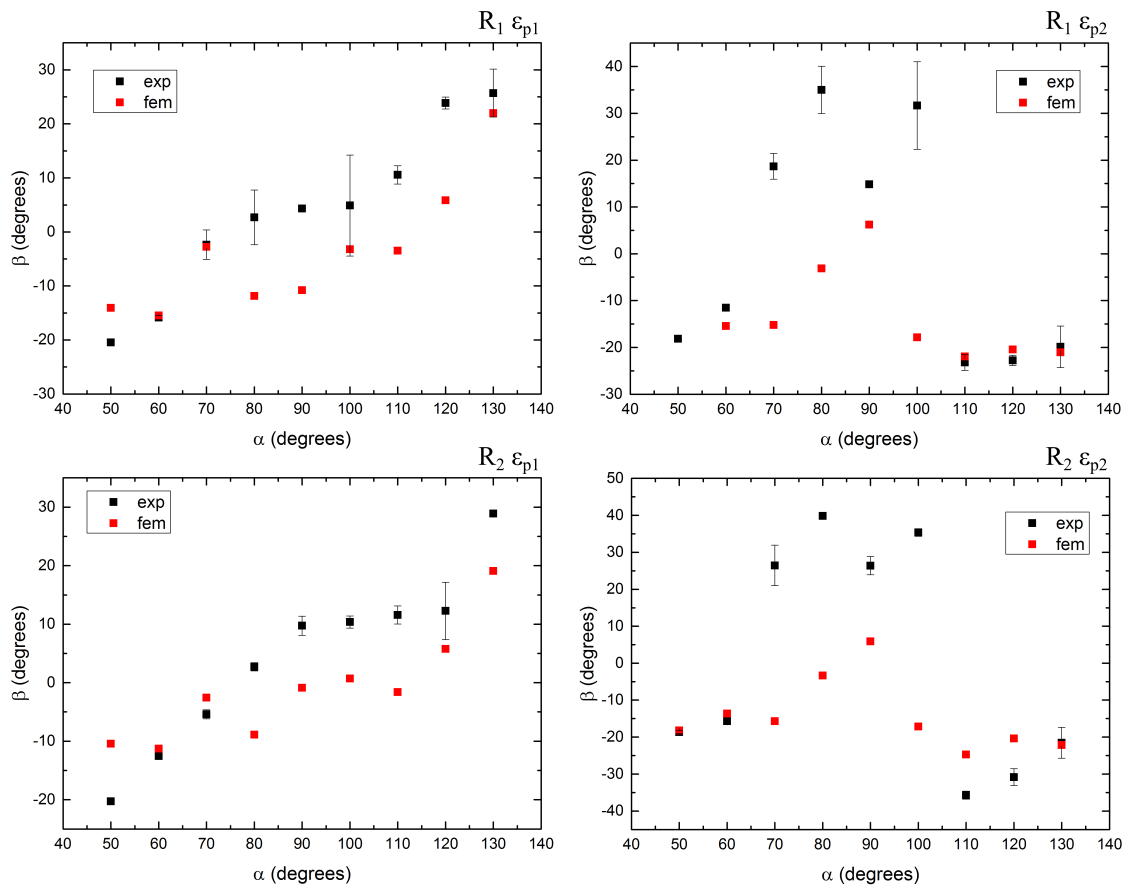


Figure 4.20: Angle between first component of strain gauge and first principal strain, calculated from experimental and model results. There is deviation between data sets than is the case for the strain/load data, suggesting that difference between the model and the experiment have little effect on the direction of the principal strains.

The measurement of  $\alpha$  is not exact, there is an estimated error of  $2^\circ$  caused by rotation when tightening the nut holding the cylinder in place. The apparatus was set, then the three load cycles were performed without resetting the angle, so this should not cause any difference between measurements with the same loading condition.

It was stated in section 4.2.2 that compliance in the frame causes a waiting time of a few seconds before the apparatus settles and the measured strain takes on an elastic response to the increasing load. This is partially caused by the apparatus shifting and bending very slightly when first loaded, mostly due to the bolts supporting the angled plate not being perfectly parallel or the femoral head moving within the concave spherical surface of the load cell attachment. This should not cause a large error as it was ensured that nothing visibly moved, and the test was terminated if there was any visible motion.

Another possible cause for error is inaccuracy in measuring the strain/Newton from the gradient of the strain vs time graphs. Some noise is present in the signal, and they are not totally linear at start due to compliance in apparatus. Tests resulting in data sets with excessive noise were repeated, but this did not remove the effect entirely.

## 4.6 Conclusion

The aim of the work presented in this chapter is to develop the techniques necessary for mechanical testing of femoral samples, as well as a finite element model with loads applied through contact mechanics, and comparing the strains present in each. The purpose of this was to test out the methods that will be used with a real bone femur sample with a more robust, easily available, and structurally simple PVC model femur.

Trilateration was used to determine the coordinates of the points in the geometry of the Comsol model corresponding to the location of the strain gauges on the surface of the PVC femur. This technique has not been used for this purpose before, so its reliability was assessed and considered acceptable.

Both the experiment and the model quantified the loading condition of the femur with three angles,  $\alpha$ ,  $\phi$  and  $\theta$ . Altering  $\phi$  and  $\theta$  in this experiment does not provide a significantly more varied data set when compared to just changing  $\alpha$  and keeping  $\phi$  and  $\theta$  the same. This may not be the case for all  $\phi$  and  $\theta$  combinations but, given that it is important to keep testing time with the bone femur to a minimum, only the effect of changing  $\alpha$  will be investigated with the sheep's femur.

The results of the experiment indicate that, under the conditions of this experiment, strains in the neck of the femur are largest when the body is rotated away from an exclusively sideways fall, and is angled forwards or backwards.

The results show some discrepancy between the experimentally measured strain and the strain calculated in the model, particularly at large angular deviations from the idealised sideways fall ( $\alpha = 90^\circ$ ). A potential cause of this is the friction between the contact surfaces, which was not included in the simulation. The effect of friction at the interface between the femoral head and the load cell attachment will be investigated when the sheep's femur is tested. There is a significant level of scatter within the experimental data. Attempts will be made to remove sources of this variation in the data by continuing to ensure that the apparatus is adequately bolted together and the femoral head is aligned with the load cell so that there is no detectable movement when the load is applied.

## Chapter 5

# Computational and Experimental Investigation of Strain in a Sheep's Femur

### 5.1 Introduction

The next stage of the investigation is to create a model for sheep's bone and compare with experimental results. Sheep bone was used because it is more readily available than human bone, and therefore easier to replace if it gets damaged.

The differences between the sheep and PVC femurs must be taken into account, both in terms of the properties of the material and the shape of the sample. The sheep bone cannot be left at room temperature indefinitely or it will decay, so care must be taken to minimise the length of time spent carrying out the experiments, while ensuring that a sufficiently varied data set is generated. The techniques necessary for bonding strain gauges to bone have already been successfully used with the PVC femur, so no changes need to be made. A significant difference between the PVC and bone models is that the spatially dependent Young's modulus must be included in the sheep's femur model.

Although there is a layer of hard cortical bone surrounding the sheep's femur, it is quite thin at the greater trochanter. The greater trochanter of the PVC femur

was allowed to rest directly on the angled steel plate. Protection of the greater trochanter was considered necessary to protect the sheep's femur from damage during the experiment. A PMMA cap was used, as was skin-simulant foam, and the dependence of strain on which of these two was used was assessed. The apparatus was made with the dimensions of both the PVC and the sheep femur in mind, so it can be used for both samples without need for modification.

The smaller size of the sheep bone meant that the gauges could not all be bonded to the same places as they were on the PVC femur. A single gauge was not bonded to the posterior side of the neck, as was the case in for the PVC femur, but was instead bonded to the anterior side of the neck. The new configuration of the gauges is further discussed in section 5.2.3.

A new load cell attachment was required to fit the smaller sized head of the sheep's femur. Two attachments were made, one perspex and the other PTFE. The results presented in the previous chapter showed some difference between the strains measured in the experiment and the model. A potential cause for this is the friction between the contact surfaces, which is present in the experiment but were not included in the model. By testing the bone with two attachments with different frictional coefficients and comparing the strain measured in otherwise identical experiments, it can be confirmed whether the friction between the femoral head and the load cell attachment has an effect on the strain measured by the gauges.

## 5.2 Experiment

The distal end of the sheep's femur was set into an aluminium cylinder with PMMA bone cement as described in section 3.3, and bolted to the apparatus in place of the PVC femur.

In order to reduce the amount of time taken to carry out the tests, and therefore reduce the length of time at which the bone is at room temperature, a subset of

the loading angles used in the PVC femur experiment was used. The experimental results from section 4.5 showed considerably more variation in results caused by varying  $\alpha$  across the range of nine angles tested than between the two  $\phi$  and  $\theta$  angles. For the sheep's femur experiment, only  $\alpha$  was varied, and the other two loading angles were kept at  $\phi = 10^\circ$ ,  $\theta = 4^\circ$  for all tests. The test was run for each loading configuration three times, as before, to provide a mean and standard deviation.

### 5.2.1 Load Cell Attachments

The load was applied through a load cell attachment designed to simulate the acetabulum in much the same way as was done with the PVC experiment. The attachment used in that experiment cannot be used as it was custom made to fit the PVC femur. The PVC femur is cast from human bone, which has a much larger femoral head than sheep bone. A new attachment was made in the same way, but designed to fit the sheep femur.

The attachment was designed in SolidWorks using the same method of superimposing a sphere over the femoral head described in section 4.2.1.1. The radius of the femoral head was determined to be 10.5 mm, a radius of 11.25 mm was used for the concave spherical surface of the attachment. The drawing of the attachment is shown in figure 5.1.

The rapid prototyping machine was not operational when the bone attachment needed to be made, so 3D printing was not an option. Instead, the shape of the attachment was machined from plastic. This provided the opportunity to experiment with the materials used to make the attachment. The contact mechanics implemented in the finite element model do not incorporate a frictional component. Comparing results taken with two different load cell attachments with different coefficients of friction with the model results will show whether this is a reasonable assumption to make or if the friction between the acetabulum and the femur needs to be taken into account. Perspex and polytetrafluoroethylene (PTFE) were used. The two load cell attachments are shown in figure 5.1.

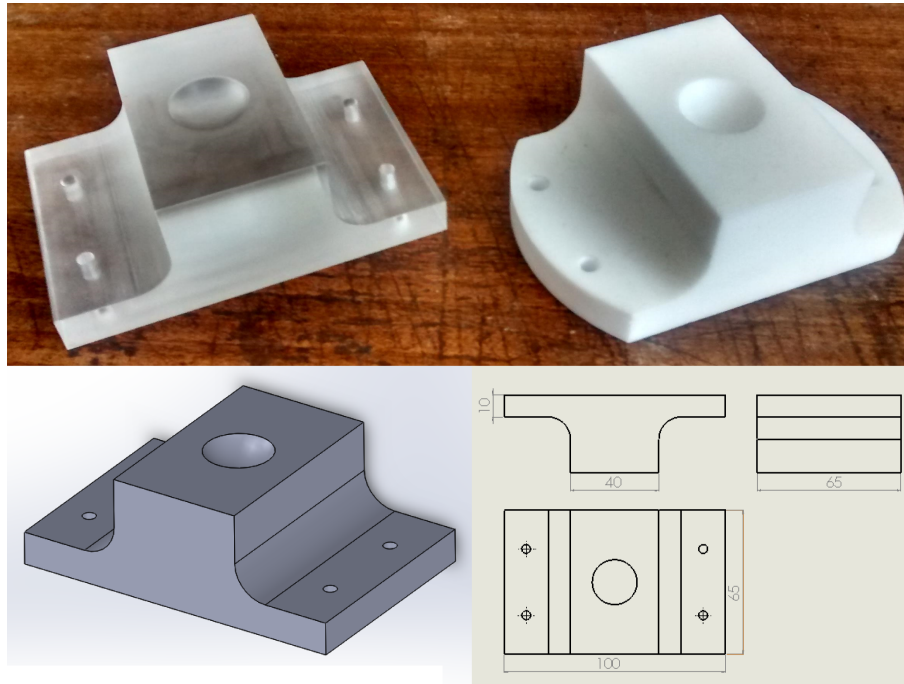


Figure 5.1: The two load cell attachments used in the experiments with the sheep's femur: machined from perspex (left) and PTFE (right). The PTFE attachment was machined from a cylinder, the full  $100 \times 65$  mm base could not be included. It has a large enough base to accommodate the four drill holes, so this does not compromise the structure.

### 5.2.2 Greater Trochanter protection

In a real fall scenario, the femur does not make direct contact with the floor. The impulse travels through fat and muscle tissue before reaching the greater trochanter. The soft tissue dampens the impact, lessens the amplitude, and widens the area over which the force is delivered to the bone [35, 37]. The purpose of this experiment is not to simulate fracture loads, as the femur must be put through many load cycles so it is important to avoid damaging the bone in the process. The force-reducing effect of the soft tissue is not of concern here, nor is its damping effects as the applied load is quasi-static, but the effect of spreading the load over a wider area is important. No soft tissue surrogate was used in the experiments with the PVC femur, the greater trochanter was rested directly on the steel angled plate. The cortical shell is very thin at the greater trochanter, measured to be  $0.6 \pm 0.1$  mm from the scan of the sheep bone sample, so a load large enough to cause significant strain in neck could potentially cause crushing here. It is necessary to use some protection at the greater trochanter to avoid large contact pressures which could cause permanent damage to the bone.



Figure 5.2: Two greater trochanter protectors. Left: PMMA, right: foam.

Some studies involving the application of force to the proximal femur involve the use of PMMA caps to distribute the load over a wider area [14, 16, 20]. This is a hard material which, unlike the soft tissue, does not dampen the force at all. It only serves to increase the contact area and reduce the pressure. Other studies use polymer foams as a surrogate for soft tissue, particularly when simulating impact forces in the hip joint [34–37]. Taking one set of data with a PMMA cap and another with foam between the greater trochanter and the floor and comparing the two will show whether the foam makes a difference to the relationship between strain and load. Figure 5.2 shows each of the greater trochanter protectors and their placement in the experiment.

The sheep's femur was removed from the freezer and left to thaw for 12 hours in a refrigerator prior to the casting of the PMMA cap. The PMMA cement was mixed as in section 3.3.1, then the greater trochanter was greased and a layer of cement approximately 3 mm thick was moulded to the surface. Care was taken to ensure that the cement cap did not wrap around the bone too much, so that it could be removed after setting, but also that it wrapped around the bone sufficiently that it did not slip off during loading, and that the cap fit the greater trochanter in a unique way. Once the cement had hardened, a marker pen was used to draw around the cap onto the surface of the bone to indicate where the cap should fit each time it was placed on the greater trochanter.

The thickness of the soft tissue over the greater trochanter varies between indi-

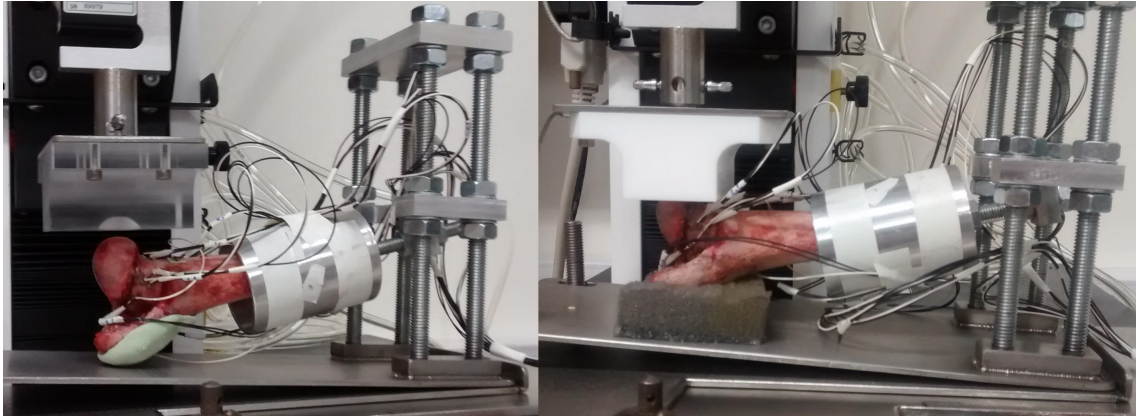


Figure 5.3: Left: perspex attachment and PMMA cap. Right: PTFE attachment and foam.

viduals. Robinovitch et al. [35] sampled the tissue thickness of nine cadavers, all over the age of 60 at time of death, and found a range of 8 to 45 mm, with a mean of  $24 \pm 3$  mm. A thickness of 20 mm was selected for the soft tissue surrogate. A block of open-cell polyether foam was used with a 1.5 mm layer of silicone rubber to simulate skin. Blocks of foam ( $290 \times 210 \times 100$  mm) already coated in a 2 mm layer of silicone were sourced from the left-over materials from a previous experiment [66], and so did not have to be prepared for this experiment. The foam was cut to 50 mm square, 20 mm thick with a hand saw. The foam was placed silicone side down onto the angled steel base plate directly underneath the greater trochanter. Three foam squares, all with a layer of silicone on one side, were cut so that they could be cycled throughout the testing to allow the foam to rest between testing. Each square was used for the three load cycles applied for one of the loading angles, then allowed to return to its original shape while the next two loading angles were tested with the other two squares.

### 5.2.3 Method

Four sets of data were taken, for each combination of the two load cell attachments and the two greater trochanter protectors. Figure 5.3 shows the experimental set up with the sheep's bone, with two configurations that show both attachments and both protectors.

The results of the experiment reported in chapter 3 do not confirm that strain

measurements taken from the bone sample can be considered reliable following four freeze/thaw cycles after the gauges are bonded to the surface. All tests must be carried out after no more than three cycles, or their reliability cannot be confirmed. The femur was taken out of freezer and the distal end was set in PMMA as described in section 3.3. The PMMA cap was made then gauges and solder terminals were bonded to the bone and the wires were soldered before the femur was returned to the freezer. The bone could now be tested on three separate occasions, with the bone being returned to the freezer twice between them. The femur was removed from the freezer around 15 hours before testing and left to thaw in a refrigerator. It was removed from the refrigerator 30 minutes before testing and allowed to reach thermal equilibrium at room temperature.

During the first testing period, the experiment was carried out with the PMMA cap and perspex attachment. The PMMA cap and PTFE attachment were used during the second testing period. Two data sets were taken during the third period, with the foam greater trochanter protector and each of the two load cell attachments. The femur was returned to the freezer after each testing period, and was at room temperature for between five and seven hours.

The same gauge configuration was used as in the PVC femur experiment, two tri-axial rosette and two single gauges. The gauges and solder terminals were bonded using method outlined in section 3.2. The results of the spatially dependent model reported in section 2.4 showed high strain concentration around the neck, so a similar selection of gauge locations as were used for the PVC femur was considered. An identical set of locations could not be used, as the sheep femur is much smaller than the human femur used to cast the PVC model. It was not possible to fit both a single and a rosette gauge in the middle of the posterior surface of the neck along with the with solder terminals for all four component gauges. Instead, only the rosette gauge was placed in the middle of the posterior surface of the neck, and the single gauge was bonded to the anterior surface of the neck.

The femur was loaded using a similar method as was used for the PVC femur, by

gradually increasing the load to a maximum, but with a smaller loading rate of 20 N per minute, and a smaller maximum load of 35 N. This was so that the femur could be closely observed so that any sign of damage to the bone would be noticed and the experiment could be terminated. No signs of damage were observed during any of the tests. The smaller maximum load was used as a precaution against overloading the bone and causing damage.

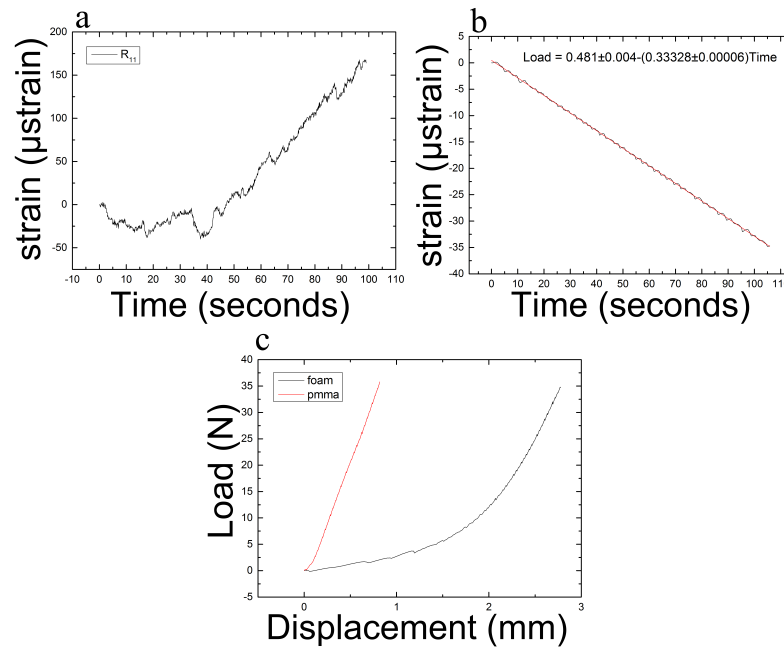


Figure 5.4: a) Sample strain vs. time plot taken with foam greater trochanter protector. b) Load vs. time with foam protector. c) Comparison of load vs. vertical displacement of the load cell (measured by control software) for the different greater trochanter protectors.

Figure 5.4a shows an example of the strain measured by one of the gauges on the sheep's femur taken with the foam greater trochanter protector. The smaller gradient before the foam was crushed is more a measure of the properties of the foam than the bone, the second gradient from when the foam was fully crushed is a measure of the deformation of the bone, so the gradient of only this part of the data was used to provide a measure of the strain per Newton. Figure 5.4b shows that the load still changes linearly with time when foam is used, and at the expected rate of 20 N per minute. Figure 5.4c shows a typical load vs. displacement graph output by the tensometer control software when testing the femur with the PMMA and foam protectors. With the PMMA cap, the loading is linear with extension once the system is settled. In the case of the foam, the gradient increases with load as

the structure effectively hardens as it is compressed. The early part of the graph, up to around 50 seconds, shows a much slower increase in strain per second than the latter part of the graph.

### 5.3 Model

The femur used in this experiment had previously been used to generate the mesh and linear interpolation function used to create the bone model in section 2.4. The same STL file and linear attenuation data were used to generate this contact model. The bone geometry was imported into Comsol and partitioned using the same settings used in the model described in chapter 2. The load cell attachment geometry was drawn just as in chapter 4, but with the dimensions of the cells designed to match the attachment designed to use with the sheep femur. The interpolation function was applied across the bone geometry, material properties were assigned according to equations 2.2.1-2.2.5. Contact was modelled between the femoral head and acetabular face of the load cell. The contact pressure was again estimated by calculating the pressure between a sphere and spherical cup using equation 4.4.5. The Young's modulus of the surface of the femoral head was estimated to be 20 GPa by sampling the modulus of 10 points at the surface of the femoral head. The estimated contact pressure was calculated to be 4.5 MPa.

Including the contact mechanics between the greater trochanter and the foam would significantly complicate the model, as it would need to simulate the large displacements of the foam. Since the strain per Newton measurement of the experimental results was based on measurements taken when the foam is compressed, there is no need to model the load dependant Young's modulus of the foam. The PMMA cap was moulded to the surface of the bone, so the contact area is much larger than that of the PVC femur and the flat steel plate, which is dependent on the magnitude of the load. Similarly, the foam deforms to match the surface it is in contact with, creating a large surface area. The large surface area of the contact which, unlike the ellipse-plane interface assumed in the PVC model, does not depend

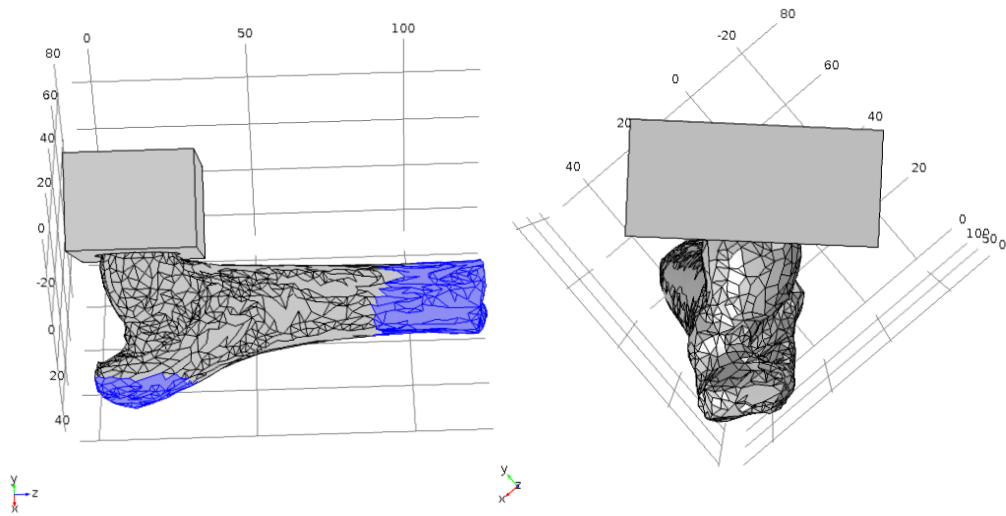


Figure 5.5: Alignment of femur and load cell attachment with respect to coordinate axes. Highlighted boundaries in left image show fixed boundaries.

on the applied load, means that the contact mechanics at this interface does not have such a significant effect on the strain induced in the femur. A fixed constraint was applied to boundaries on the greater trochanter (figure 5.5).

A single model was created to simulate the strain measurements to be compared with all four experimental data sets. This was to keep the model as simple as possible. If the experimental data sets significantly differ from one another, this will indicate that the greater trochanter protection and the load cell attachment material have an effect on the strain induced in the sample, and that one single model cannot legitimately be used to simulate all conditions. The load cell attachment was given the material properties of perspex ( $E = 3.3$  GPa [46],  $\nu = 0.415$  [47, p.277]).

The PVC femur was rotated about a point at the centre of the femoral head while the load cell attachment remained stationary. In the case of the sheep bone model, the interpolated Young's modulus function is spatially dependent and assigned based on coordinates which use the same coordinate system as the STL file used to generate the femur geometry. Rotating the femur geometry would cause the geometry and the function to no longer match up in space. Instead, the attachment was rotated around the femoral head. This means that the normal direction to the

top surface of the attachment is no longer aligned along one of the axes within the Comsol environment. The shaft of the femur was aligned vertically in the scanner, so it pointed along the  $z$ -axis. The rotation of the load cell attachment is therefore exclusively about the  $z$ -axis (figure 5.5). Instead of aligning the displacement applied to the face along one of the axes (which, in the PVC model was perpendicular to the surface), the displacement was applied normally to the surface. The portion of the greater trochanter covered by the PMMA cap was estimated and these boundaries were fixed.

Comsol can be used to directly calculate linear and shear stress along the coordinate axes. In the PVC model presented in chapter 4, the top surface of the attachment was aligned perpendicular to the  $y$ -axis under all loading conditions. In this model, the attachment rotates around the stationary femur, so the plane of the top surface is not always in alignment with one of the axes. The stress tensor must be transformed so that it is perpendicular to the surface.

The stress tensor is rotated angle  $\theta$  about the  $z$ -axis:

$$\begin{pmatrix} \cos \theta & -\sin \theta & 0 \\ \sin \theta & \cos \theta & 0 \\ 0 & 0 & 1 \end{pmatrix} \begin{pmatrix} \sigma_x & \tau_{xy} & \tau_{xz} \\ \tau_{xy} & \sigma_y & \tau_{yz} \\ \tau_{xz} & \tau_{yz} & \sigma_z \end{pmatrix} \begin{pmatrix} \cos \theta & \sin \theta & 0 \\ -\sin \theta & \cos \theta & 0 \\ 0 & 0 & 1 \end{pmatrix} = \begin{pmatrix} \sigma'_x & \tau'_{xy} & \tau'_{xz} \\ \tau'_{xy} & \sigma'_y & \tau'_{yz} \\ \tau'_{xz} & \tau'_{yz} & \sigma'_z \end{pmatrix} \quad (5.1)$$

The  $y$ -component of the linear stress is being transformed, so only the linear  $y$ -component of the transformed tensor,  $\sigma'_y$ , is needed.

$$\sigma'_y = \sigma_x \sin^2 \theta + \sigma_y \cos^2 \theta + 2\tau_{xy} \sin \theta \cos \theta \quad (5.2)$$

The rotated  $y$  component of the stress is integrated over the top surface of the attachment as before to find the total load. Figure 5.6 shows the rotation of the stress tensor and the direction of the stress which needs to be measured.

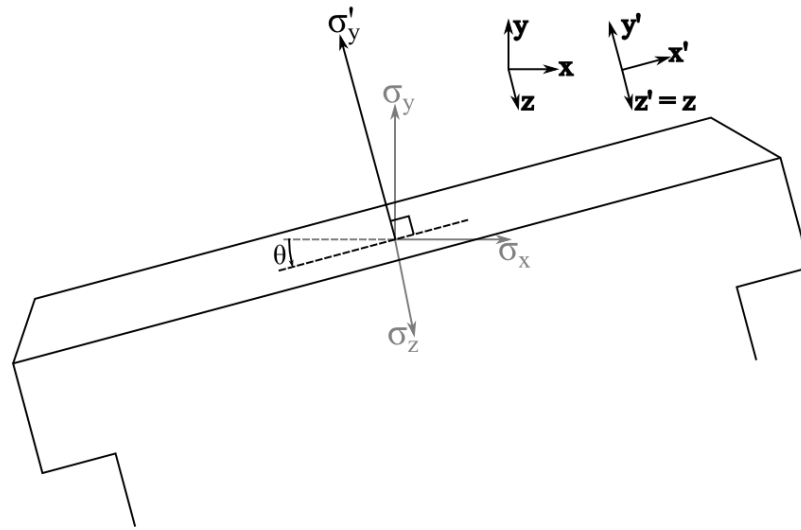


Figure 5.6: Load cell attachment is rotated about  $z$  axis, stress perpendicular to top surface is integrated across plane.

### 5.3.1 Trilateration

The coordinates of the gauge points were located in the model geometry with trilateration. Figure 5.7 shows the location of the reference points and the gauge points. No visible depression at the lateral side of the head is present in the sheep's femur, unlike the PVC human analogue, so another reference point was needed. The most prominent point of the lesser trochanter was selected instead. The distances of each of the gauge points from each of the reference points,  $r_1$ ,  $r_2$ , and  $r_3$ , are included in table 5.1. As with the PVC model, the first and third principal strains were calculated in the Comsol model for the rosette gauges, and the method described in section 4.4.3 was used to calculate the strains along the gauge directions for the single gauges.

radii (mm)			
	$r_1$	$r_2$	$r_3$
R <sub>1</sub>	34	38	19
R <sub>2</sub>	29	27	20
S <sub>1</sub>	32	36	31
S <sub>2</sub>	22	27	44

Table 5.1: Distances of each gauge from each of the three reference points on the sheep femur.

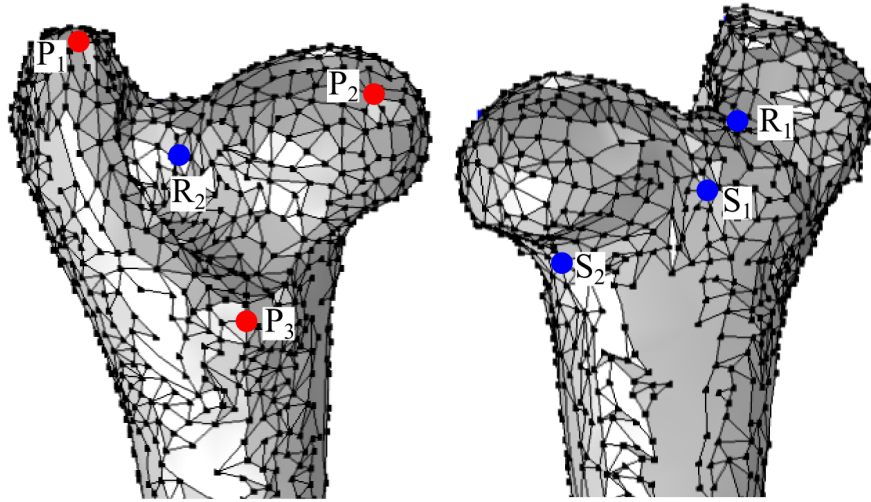


Figure 5.7: Location of reference points used in trilateration (marked red) and the calculated gauge points (blue).

## 5.4 Results

The strains measured in the experiment and calculated by the finite element model are plotted in figures 5.8 to 5.13. As with the PVC femur study, the strain at each rosette gauge point has been split into first and second principal strains, and the strain at the single gauge points is measured along the gauge direction. It is clear that the model results differ significantly from all four experimental datasets. The angle between the first strain gauge component and the first principal strain calculated from the results of the experiment and the model is plotted in figure 5.14. There is visibly less deviation between the data sets for this variable than there is for the principal strains.

### 5.4.1 Comparison of Experimental Results

In order to assess whether the greater trochanter protector and the load cell attachment material have a significant influence on the strain measured, a statistical test is required to assess whether the data sets differ significantly from one another. The Student's *t*-test was used to compare individual data points, each consisting of three measurements, between sets to confirm whether the means can be considered to be the same.

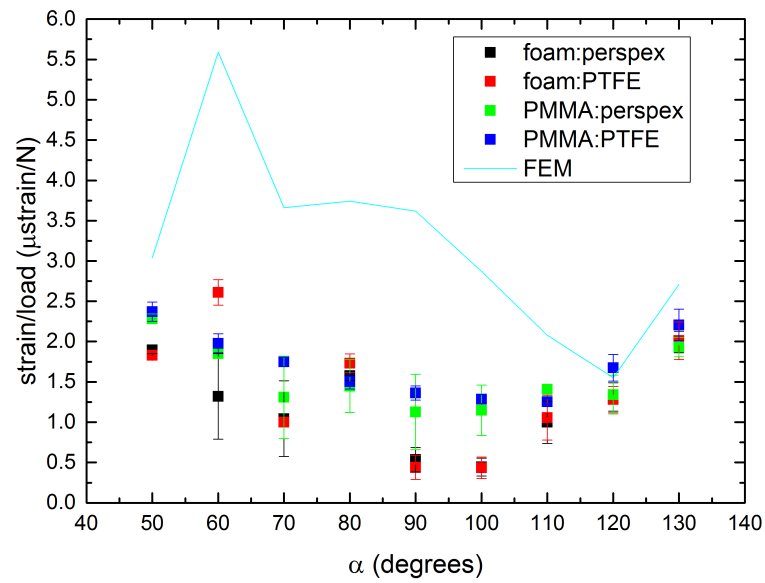


Figure 5.8: First principal strain measured experimentally and calculated with the finite element model at rosette gauge point  $R_1$ . The simulated strain is considerably greater than the experimental strains for  $\alpha < 120^\circ$ .

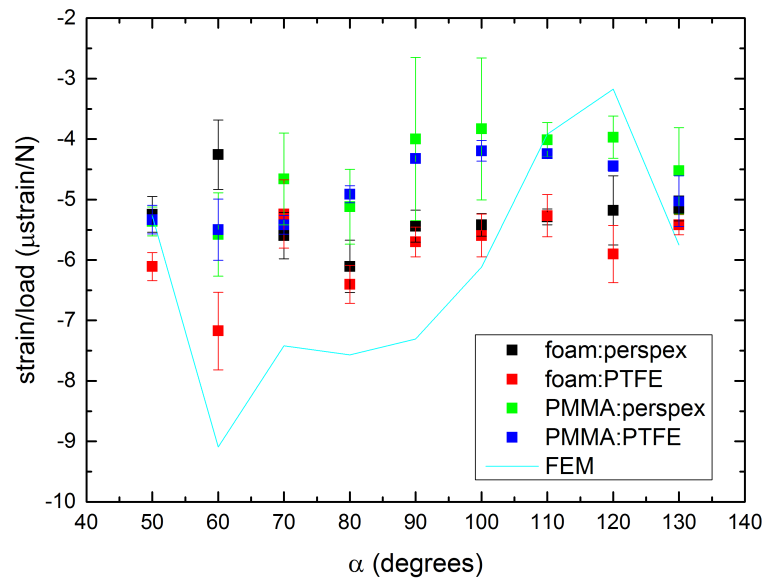


Figure 5.9: Second principal strain measured experimentally and calculated with the finite element model at rosette gauge point  $R_1$ . The model results are closer to the experimental data than was the case for the first principal strain.

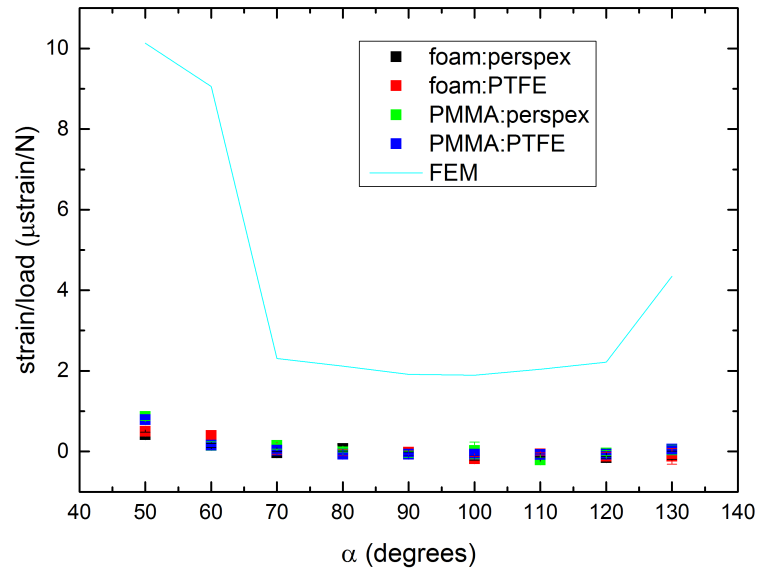


Figure 5.10: First principal strain measured experimentally and calculated with the finite element model at rosette gauge point  $R_2$ . The strains calculated with the model are considerably larger than the experimental data. This is particularly visible at the high and low extremes of  $\alpha$ .

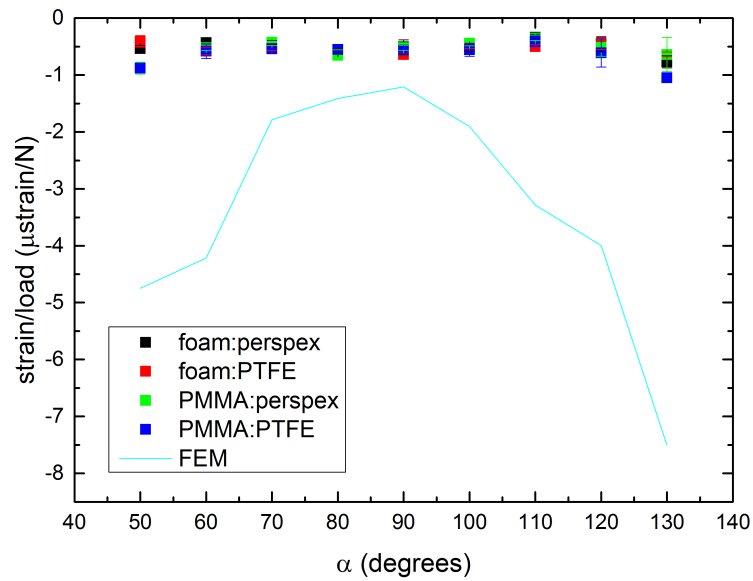


Figure 5.11: Second principal strain measured experimentally and calculated with the finite element model at rosette gauge point  $R_2$ . The simulated strains are again much larger than the experimental data, particularly at the high and low extremes of  $\alpha$ .

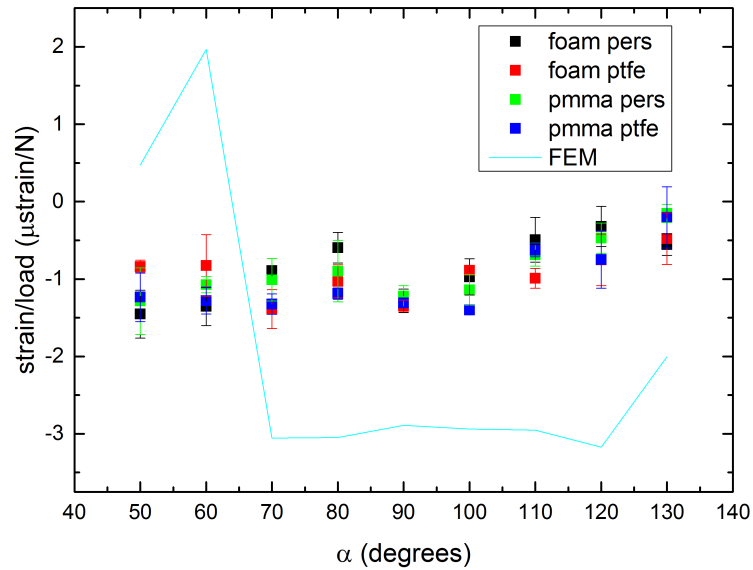


Figure 5.12: Experimental strain and strain calculated with the finite element model at single gauge point  $S_1$ . Simulated strains are typically significantly larger than the experimental strains, and feature a large change in strain from positive to negative between  $\alpha = 60^\circ$  and  $70^\circ$ . This is not seen in the experimental strains, which are exclusively negative.

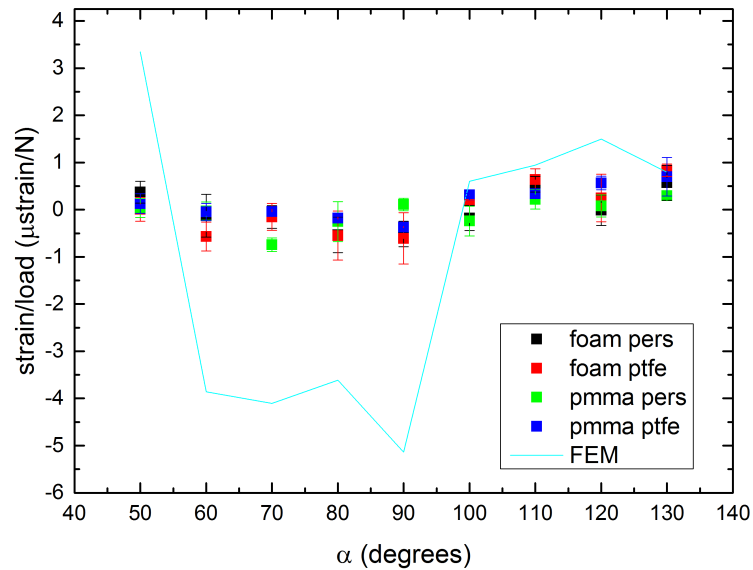


Figure 5.13: Experimental strain and strain calculated with the finite element model at single gauge point  $S_2$ . Simulated strains are significantly larger than experimental strains for  $\alpha \leq 90^\circ$ .

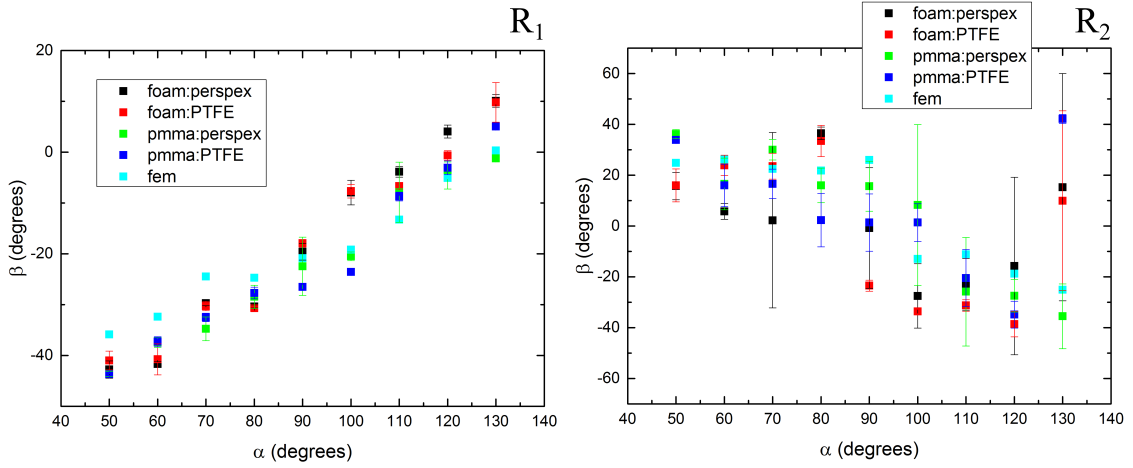


Figure 5.14: Angle between first component of strain gauge and first principal strain, calculated from experimental and model results. As was the case for the results of the PVC study, there is less deviation between the data sets. This indicates that any differences between the model and the experiment have little effect on the direction of the principal strains.

The Student's  $t$ -test is a statistical test of the null hypothesis that the means of two samples are equal [67, p.158]. The test statistic,  $t$ , is calculated from the means of the two samples,  $x_1$  and  $x_2$ , the size of each sample,  $N_{x_1}$  and  $N_{x_2}$ , and  $S$ , the pooled estimate of the standard deviation,

$$t = \frac{\bar{x}_1 - \bar{x}_2}{S \sqrt{(1/N_{x_1}) + (1/N_{x_2})}}, \quad (5.3)$$

$S$  is calculated from the standard deviations of each sample,  $s_{x_1}$  and  $s_{x_2}$ ,

$$S = \sqrt{\frac{(N_{x_1} - 1) s_{x_1}^2 + (N_{x_2} - 1) s_{x_2}^2}{N_{x_1} + N_{x_2} - 2}}. \quad (5.4)$$

The critical values of  $t$  are defined by the Student's  $t$ -distribution.

The Student's  $t$ -test was used to determine whether various measurements could be considered to be the same for data taken with different greater trochanter protectors, or different load cell attachments.  $t$  was calculated for each value of  $\alpha$ , comparing data under the following four combinations of conditions:

1. Perspex load cell attachment, compare greater trochanter protectors
2. PTFE load cell attachment, compare greater trochanter protectors
3. PMMA greater trochanter protector, compare load cell attachments

Perspex PMMA vs foam	R <sub>1</sub>		R <sub>2</sub>		S <sub>1</sub>	S <sub>2</sub>
	ep1	ep2	ep1	ep2		
50	9.0530	0.5400	6.5840	5.0264	0.5474	1.9177
60	1.7274	2.5538	0.0176	2.8457	1.7853	0.3461
70	0.6595	1.9082	3.3037	0.0404	0.7207	3.6538
80	0.6701	2.2668	1.4881	1.1025	1.1765	0.8506
90	2.0859	1.8143	0.3053	0.1722	0.5127	3.5797
100	3.6828	2.3162	1.5019	1.7734	0.9404	0.2695
110	2.6904	7.0741	2.7059	0.4141	1.0324	2.1154
120	0.1733	3.1354	2.8212	0.4749	0.8035	0.4125
130	0.6097	1.4482	1.4462	0.6962	3.8307	1.2847
PTFE PMMA vs foam	R <sub>1</sub>		R <sub>2</sub>		S <sub>1</sub>	S <sub>2</sub>
	ep1	ep2	ep1	ep2		
50	7.0009	4.0504	5.8066	6.7482	2.0852	0.6619
60	5.5441	3.5525	3.6930	0.0505	1.8236	2.5098
70	20.8884	0.5272	0.5893	0.1396	0.3934	0.6712
80	2.6489	7.4697	0.8950	0.0338	1.2136	1.2241
90	9.2227	9.4630	2.2515	2.0573	0.7001	0.7584
100	10.2037	6.1818	2.9883	0.9077	12.9316	5.0928
110	1.2185	5.0201	0.2520	1.5663	4.0290	2.2006
120	2.9365	5.2373	0.5440	1.0513	0.0064	1.0461
130	1.1058	1.4897	1.3803	7.3563	0.9192	0.5529

Table 5.2: *t*-test statistics calculated from results taken with the same cells

4. Foam greater trochanter protector, compare load cell attachments

The size of all of the samples was  $N_{x_1} = N_{x_2} = 3$ , the number of mechanical tests carried out for each data point.

Tables 5.2 and 5.3 contains the *t*-test statistics for each pair of strain measurements. 49 of the 216 *t*-values exceed the 0.05 confidence limit of 2.776. 12 exceeded the limit under combination 1, 21 under combination 2, 6 under combination 3, and 10 under combination 4. 14.8% of results are different at the 0.05 significance level when comparing the load cell attachments. 30.6% of results are different at the 0.05 significance level when comparing greater trochanter protectors. This is an indication that both the interfaces between the load cell attachment and the femoral head, and between the greater trochanter and the base plate have an effect on the strain response to loading. It is clear from figures 5.8 – 5.13 that the difference between the experimental data sets is much smaller than that of the experimental and model

PMMA Perspex vs PTFE	R <sub>1</sub>		R <sub>2</sub>		S <sub>1</sub>	S <sub>2</sub>
	ep1	ep2	ep1	ep2		
50	1.1081	0.1554	1.0871	0.0223	0.1651	0.5762
60	1.7743	0.1662	0.1009	0.8492	1.7862	0.1297
70	1.4849	1.6960	1.7745	1.7925	1.7881	7.6921
80	0.2828	0.5568	4.2405	1.5730	1.2557	0.3037
90	0.8591	0.4140	0.0404	0.9575	1.0683	6.1670
100	0.7488	0.5284	0.7708	1.6196	2.1823	3.0255
110	5.6227	1.3845	2.2608	0.9103	0.5933	0.9660
120	1.9526	2.2854	0.3647	0.5743	1.1479	3.0605
130	2.0778	1.0488	0.1780	2.2588	0.2213	1.7234
Foam Perspex vs PTFE	R <sub>1</sub>		R <sub>2</sub>		S <sub>1</sub>	S <sub>2</sub>
	ep1	ep2	ep1	ep2		
50	1.5468	3.9739	1.8211	1.8724	3.3062	1.8625
60	4.0332	5.8632	7.1574	3.6434	1.9480	1.3873
70	0.1644	0.9044	1.3134	3.2210	3.3858	0.0080
80	2.0746	0.9562	1.6555	0.8346	2.5808	0.0430
90	0.7787	1.2470	1.0640	1.8179	0.6667	0.2652
100	0.0916	0.7573	0.3897	0.6041	0.6185	2.3353
110	0.2552	0.0934	4.2744	4.6064	2.7318	0.6278
120	0.2390	1.6900	0.5645	0.1021	1.7620	0.7566
130	0.1098	1.7671	0.2206	1.9354	0.3647	1.1689

Table 5.3: *t*-test statistics calculated from results taken with the same greater trochanter protectors

data.

Figure 5.15 shows only the experimental data. For all datasets, the strain at the first rosette gauge point is compressive for all loading angles. The largest strains were measured at lower  $\alpha$  values. The strain is always larger at the first rosette gauge point than it is at the second. The strains at the second rosette gauge point are also all compressive, aside from at  $\alpha = 50^\circ$  for the PMMA:perspex dataset, where the magnitude of the first principal strain exceeds that of the third. The largest strains are found at the high and low extremes of  $\alpha$ .

The strain measured at the first single gauge point is compressive for all angles, and largest for lower  $\alpha$  angles. At the second single gauge point, the strain is compressive between the angles  $0^\circ < \alpha < 90^\circ$ , and otherwise tensile. The strain peaks at  $90^\circ$ .

### 5.4.2 Comparison of Experimental and Model Results

A possible cause for discrepancy between the model and experimental results is an insufficiently high resolution of data imported into the linear interpolation function which characterises the spatially dependent Young's modulus of the bone. The linear attenuation data was downsampled so that each value represented the average linear attenuation in a  $1 \text{ mm} \times 1 \text{ mm} \times 1 \text{ mm}$  volume, in order to create a sufficiently small file which could be imported into Comsol without the software crashing. Much of the cortical bone at the head and neck of the femur can be smaller than 1 mm in thickness. The linear attenuation data in voxels covering the the boundaries between cortical bone and air is averaged across the two media, artificially lowering the linear attenuation, and therefore Young's modulus of the cortical bone at these points. Figure 5.16 shows Young's modulus plotted along a line through the neck of the femur in the plane perpendicular to the main axis of the femur, starting from the location of the second rosette gauge,  $R_2$ . A two-dimensional plot of the Young's modulus on this plane is also shown. One would expect that the highest moduli would be found at the edges of the line, where the

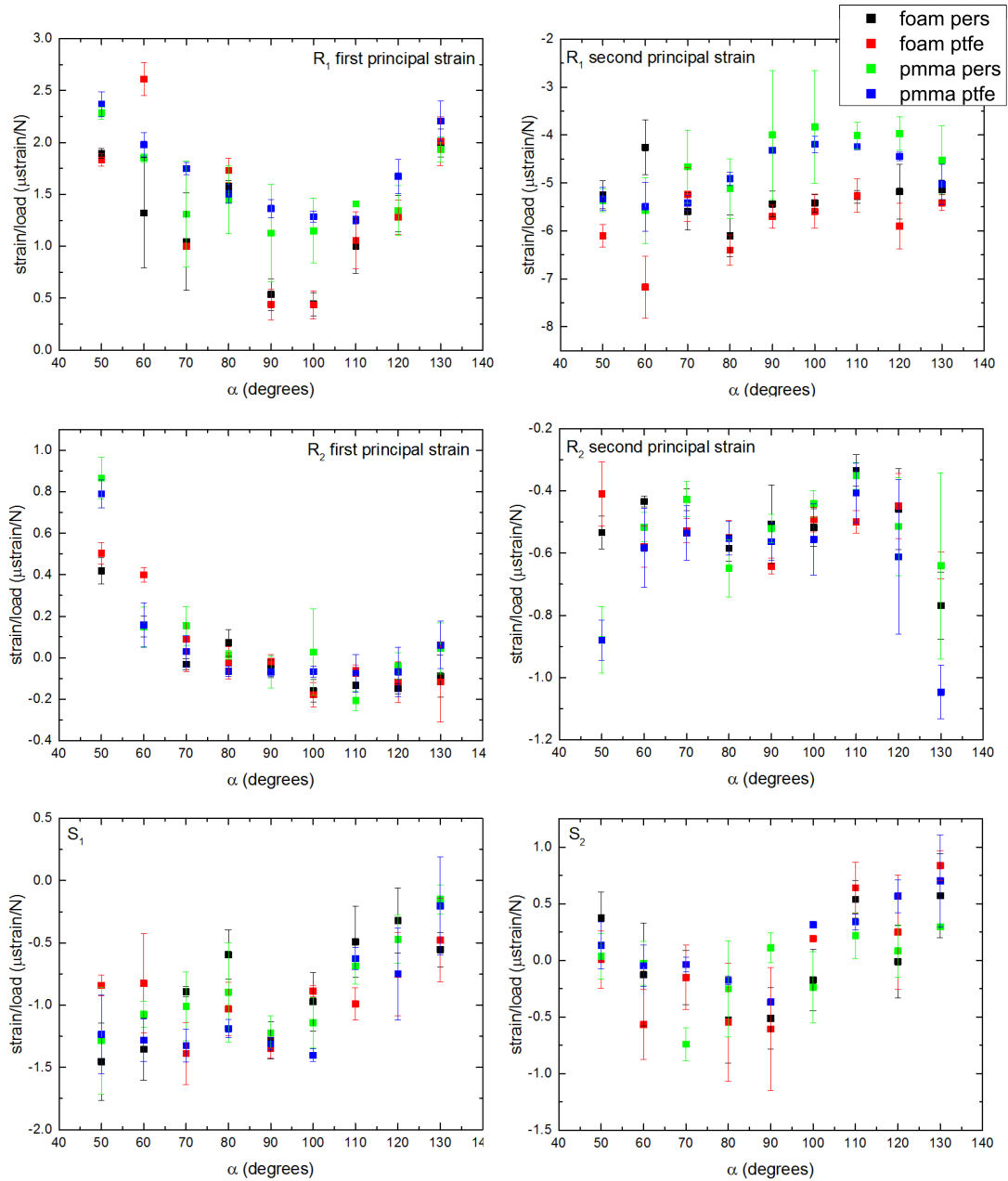


Figure 5.15: First and second principal strains calculated from strains measured with rosette gauges, and strain measured with the single gauges. The largest strains measured at the first gauge point are positive, and measured at the lowest  $\alpha$  angles. The strains measured at the second gauge point largest at the low (positive strain) and high (negative) extremes of  $\alpha$ . The strain at the first single gauge point is largest at the lowest  $\alpha$  angles, and is negative. The strain at the second single gauge point peaks at  $\alpha = 90^\circ$ , and is negative.

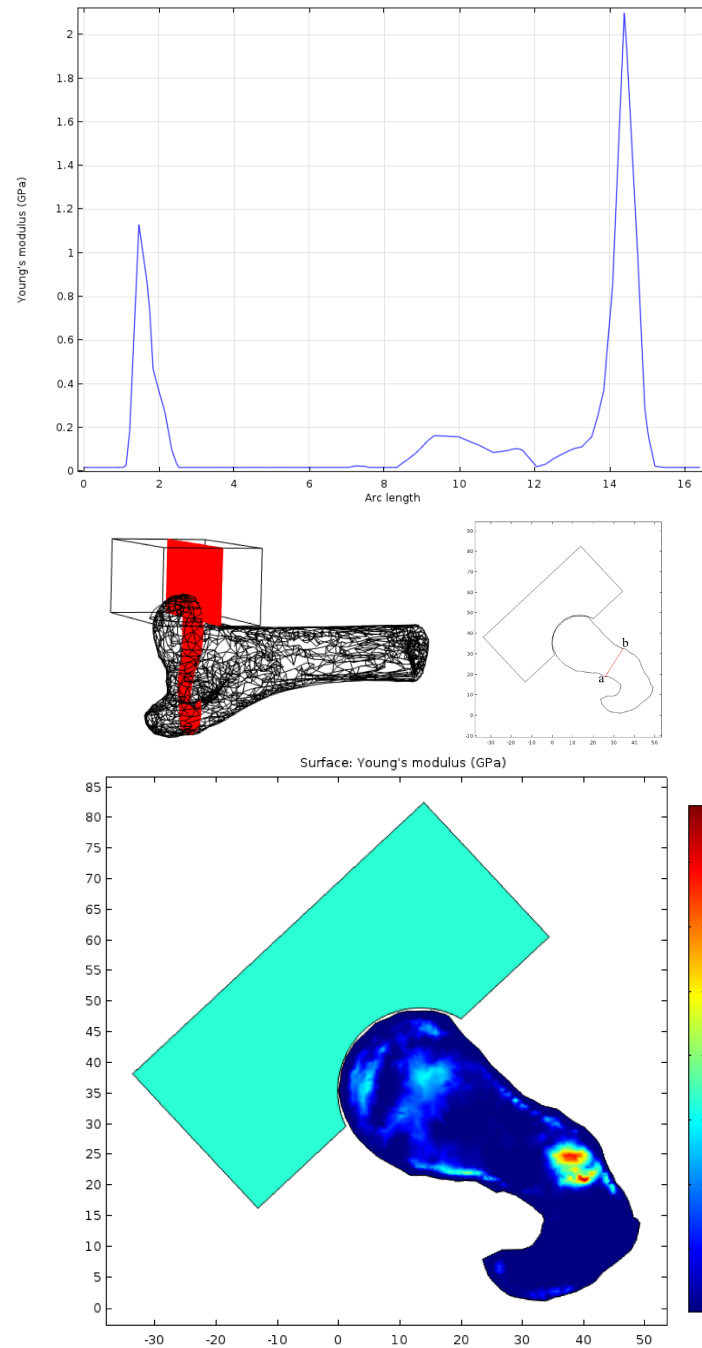


Figure 5.16: Young's modulus plotted along a line through neck of femur, and plotted onto a plane. The "arc length" plotted on the  $x$ -axis is the length of the line running from point a (the location of  $R_2$ ) to point b.

cortical bone is found, with lower values in the centre which consists of much softer tissue. Instead, there is a portion of the line approximately 1 mm long with very low modulus at either end of the line, at the edges of the structure. The modulus reaches a peak at 1.5-2 mm from boundary. The largest moduli calculated along this line are considerably smaller than the average cortical bone Young's modulus of 20 GPa given in section 5.3. The partial volume effects caused by downsampling the linear attenuation file cannot be responsible for the lowering of the modulus over this large a scale, however, the coarseness of the mesh will also have an effect. The average volume of the tetrahedral mesh elements is  $1.958 \text{ mm}^3$ . To improve this, a finer mesh would have to be used.

The mesh was refined as much as possible, further refinements resulted in a failure to generate the mesh as a degenerated triangle was created. Instead of refining the entirety of the mesh, a triangular surface mesh was applied to the bone, and this was meshed to a finer degree than the bulk tetrahedral mesh. This mesh configuration resulted the solver failing to find a solution when  $\alpha$  was set to  $50^\circ$  and  $60^\circ$ , but a solution was successfully found for the seven other simulations. The principal strains calculated at the rosette gauge points from these simulations, along with the results from the original mesh, are shown in figure 5.17. The average difference between the strains measured by two models with the same loading conditions and different meshes is 23.2%. The instances where the difference is largest are typically found where the change in strain as a function of  $\alpha$  is largest. The difference is observably large in all four graphs for  $\alpha = 130^\circ$ . The deviations between the model and experimental results at the second rosette gauge point have been found to be largest for the most extreme values of  $\alpha$  (figures 5.10 and 5.11). The use of the refined mesh reduces the scale of the deviation in this case, but there is still a significant difference between the results of this model and the experimental data.

Another possibility is that the mathematical relations used to characterise the Young's modulus of the bone do not apply to sheep bone. The equations used to calculate the Young's modulus were taken from studies into human bone [17, 33], and the equation used to determine the ash density from the  $\text{K}_2\text{HPO}_4$  concentration

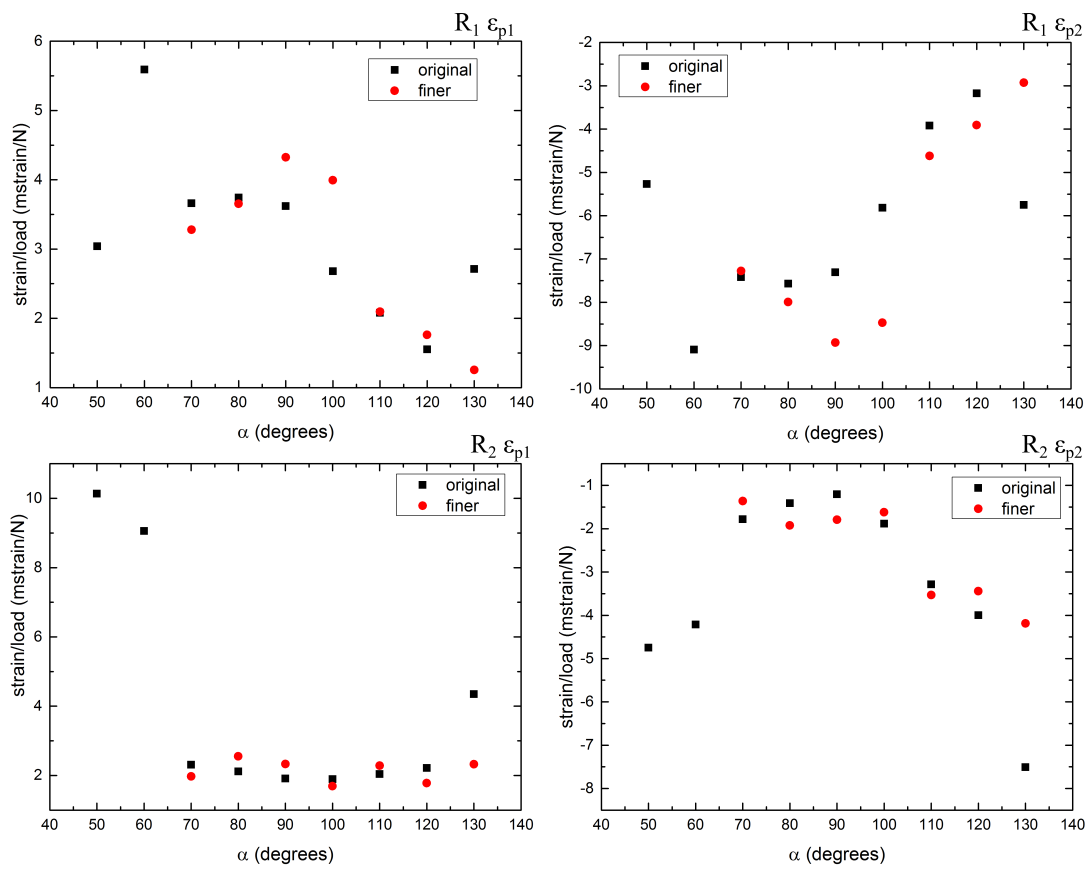


Figure 5.17: First and second principal strain/load measured at each rosette gauge points, calculated from models using the original tetrahedral mesh and the mesh with a finer triangular surface mesh. Solutions were not found with the refined mesh for  $\alpha = 50^\circ$  and  $60^\circ$ . Largest deviations are seen where the change in strain as a function of  $\alpha$  is largest, and at  $\alpha = 130^\circ$

was taken from a study which used bovine bone [32]. No studies have been found which determine whether the relationship between ash density and Young's modulus is dependent on species.

#### 5.4.2.1 Young's Modulus Compensation

The effect of the reduction in the Young's modulus of the cortical bone caused by partial volume effects on the strain induced in the model was observed by altering the material properties. A coefficient,  $A$ , was added to equation 2.2, which describes the Young's modulus of the cortical bone using the ash density of the bone. The inclusion of this coefficient allows for simple manipulation of the Young's modulus of the cortical tissue, the part of the bone with the greatest responsibility for its strength, so that any artificial lowering of the modulus may be compensated for. Equation 2.4, the interpolated equation allocated to the ash density values between the thresholds used for cortical and cancellous bone, was also amended.

$$E_{cort} = 10.2A\rho_{ash}^{2.01} \quad (5.5a)$$

$$E_{int} = 0.49 \left[ \frac{7.49A - 1}{0.33} (\rho_{ash} - 0.27) + 1 \right] \quad (5.5b)$$

The model was run under a single orientation,  $\alpha = 80^\circ$ , and  $A$  was swept from 0.1 to 1 at an interval of 0.1, then from 1 to 3.5 at an interval of 0.5. The principal strains at each rosette gauge points were recorded after each simulation, and a power function was fit to each set of data (figure 5.18). The power functions were used to find the appropriate value of  $A$  to which would give the average strain results measured during the experiment. The solution to the power functions which give the experimental average strains for the first and second principal strain at the first rosette point, and the second principal strain at the second rosette points, are 3.00, 1.53, and 9.08 respectively. There is no solution to the power function fit to the results of the first principal strain at the second rosette point which gives the mean experimental strain. This function has a significantly lower coefficient of determination than the other three, and so does not describe the model data as well. It is observed from the graph, however, that the strains calculated in the model

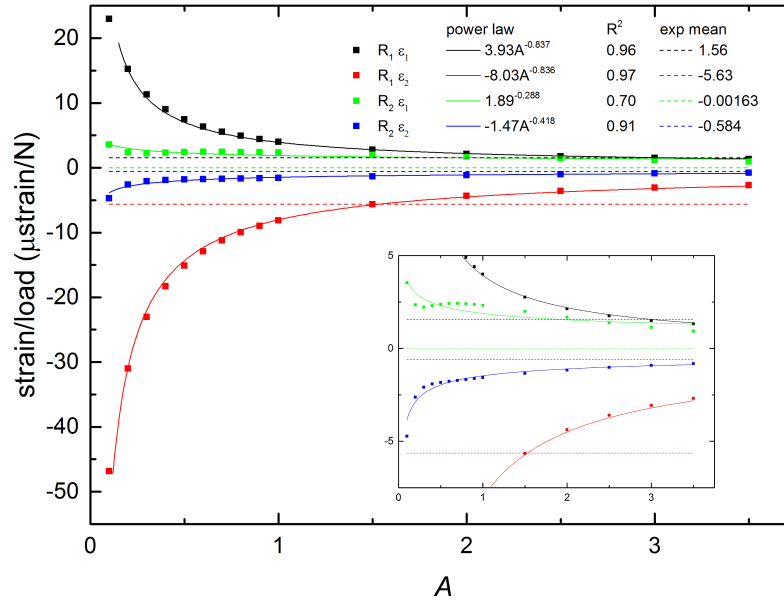


Figure 5.18: First and second principal strain measured at each rosette gauge point, as a function of the multiplication coefficient  $A$ . Results of the finite element model are plotted (points), as are the power functions fit to the points (solid line), and the mean values of the principal strains measured in the experiment (dashed line).

at this point are much larger than the experimental mean, and that any solution would require a coefficient outside of the range used in this investigation. The three solutions which were possible to find are significantly different, the smallest is approximately six times smaller than the largest. This investigation shows that altering the equation which characterises the Young's modulus of the cortical bone according to the ash density does have a significant effect on the strains calculated in the model, and that it is possible to achieve strains close to the experimental results by increasing the Young's modulus of the cortical bone. It has not been possible to create a model which accurately simulates the magnitude of strain measured experimentally in more than one location on the surface of the bone by applying a multiplication factor to the equation, due to the complexity of the geometry and the inhomogeneity of the femoral structure.

## 5.5 Conclusion

This chapter consists of an investigation similar to that carried out with PVC femur, but this time with sheep bone. This involved the inclusion of foam and PMMA greater trochanter protectors in the experiment, along with the addition of

two load cell attachments with significantly different coefficients of friction. The contact mechanics simulation used in the PVC model at the greater trochanter - base plate interface was replaced by fixed boundaries.

Data was taken with all four possible combinations of the load cell attachments and greater trochanter protectors. 30.6% of results taken with different protectors were considered to significantly differ from one another. While significant, the difference between experimental datasets was considerably smaller than the discrepancy between the experimental results and those simulated by the model. The foam protector is a much closer simulant of the soft tissue which protects the proximal femur during impact, so a way of refining the model would be to more closely model the conditions of the foam. It is not clear at this stage whether that would require the simulation of contact between the foam and the femur, along with the material properties of the foam, or simply an alteration of the fixed boundaries.

14.8% of corresponding results taken with different attachments were considered to significantly differ from one another. This is smaller than the variation caused by using different greater trochanter protectors, but it is still significant. It is preferable to use low-friction materials to simulate the acetabular surface and the low frictional forces in a real hip joint. Use of lubrication would also help reduce friction in the experiment. Addition of a frictional component to the contact model could also be considered.

There is a clear difference between the results of the model and the experiment. A potential cause for this could be inaccuracy in defining the material properties of the bone, either due to the use of mathematical relations which do not correctly characterise ovine bone, or to partial volume effects causing the lowering of the perceived Young's modulus of the cortical bone.

The experimental data shows that the largest strains are measured at the first rosette gauge point, on the superior surface of the neck, and are compressive. The largest strains occur at low  $\alpha$  values, when the femur is oriented so that contact

between the femur and the base plate occurs at the posterior face of the greater trochanter.

# Chapter 6

## Conclusion

### 6.1 Overview

The aim of the work presented in this thesis was to use a finite element model and experimental testing to simulate the loading conditions caused by a fall, and investigate how changes to the loading conditions can affect the strains measured in the proximal femur.

The technique for using CT data to develop finite element models of proximal femur bone samples was tested. Mathematical relations were used to calculate the Young's modulus of bone based on its ash density, calculated from the linear attenuation of the bone measured in the CT scan. Chapter 2 contained a preliminary study into the effect of loading orientation on strain distribution in the proximal femur. The strain distribution was confirmed to be significantly dependent on orientation, and that strain peaked in the neck of the femur, particularly when the bone was rotated away from the lateral fall position.

Techniques necessary for bonding strain gauges to bone, and for using PMMA bone cement to fix the distal end of the proximal femur sample to the apparatus were tested and implemented. The investigation into the effect of multiple freeze-thaw cycles on strain measurements showed that strain readings could be considered reliable after no more than three freeze-thaw cycles. Inconsistencies were found in the strain measurements after four cycles, but more work must be done to confirm

whether this is caused by the freezing and thawing, or if variation was introduced by some other factor. The confirmed number of cycles was sufficient to carry out the tests needed for this project, but further work is required to establish whether freezing and thawing a strain gauged bone has an effect on the strain measurements.

The models created in this study include the contact mechanics in the hip joint, as well as between the greater trochanter and the floor in the PVC model. This has not been done before now, point loads or boundary loads are frequently used to apply load to the femur. The surfaces of the femoral head and the acetabulum are irregular, so the contact area between the two depends on the orientation of the femur in the acetabulum. This study modelled the acetabulum with a smooth concave spherical surface. In a real hip joint, the femoral head and acetabulum are coated in a layer of cartilage. Further modifications to the model could include a simulation of these layers.

The requirement for the models and experiments to be directly comparable meant that strain gauge data needed to be compared with strains computed in the model at the same points on the surface of the femur. Trilateration was successfully used to locate points in model geometry to match the locations of the strain gauges used in the experiment. This is a novel use of this technique, which has not been used for registration locations of points on a CT-derived geometry before, and has shown to be used to select points to an acceptable level of accuracy.

## 6.2 Outcomes

Previous finite element studies on the proximal femur have shown that falls onto the posterolateral aspect of the greater trochanter are associated with the lowest fracture forces [13, 21, 23]. Both PVC and sheep bone experiments showed highest strains at extreme angles of  $\alpha$  in both rosette gauges. The highest strains overall measured in the sheep bone experiment were found at the lowest angles of  $\alpha$ , representing a fall in the posterolateral direction. A fully sideways fall is approximated

when  $\alpha = 90^\circ$ , and a fully backwards fall when  $\alpha = 0^\circ$ , so the lower  $\alpha$ , the further the femur is rotated towards a backwards fall.

Previous simulations into the initiation and propagation of fractures in the proximal femur caused by loading in a fall configuration have shown that fractures most frequently occur in the neck of the femur, specifically the top of the neck [13]. The preliminary models presented in chapter 2 of this thesis showed large strain concentrations around the neck of the femur, and the sheep's bone experiment and model results showed the largest strains at the gauge point at the top of the neck. Although the sheep's femur is quite different from a human femur, this result is promising. This is in keeping with the statistical analysis of real hip fracture incidences, which find that the majority of hip fractures are intracapsular [8].

The results of the sheep's bone model are not a close estimate of the results of the experiment. It is suspected that the cause of this discrepancy is inaccuracy in defining the material properties of the bone in the model. The mathematical relations used to define the Young's modulus of bone tissue are based on studies involving human and bovine bone, it is possible that they do not correctly characterise ovine bone. Inaccurate calculation of the Young's modulus of the bone tissue could be attributed to the the limited resolution of the linear attenuation data imported into the model and the coarseness of the mesh. These factors cause a partial volume effect responsible for the perceived lowering of the calculated Young's modulus of the cortical bone.

### 6.3 Limitations and Future Work

This investigation was designed to show the effect of changing the orientation of the femur in a fall configuration, to show that the model is useful and can be applied to real fall simulations. This work can potentially be developed to model the real-life conditions of fall mechanics. Very little is known about what happens during a fall, as it is impractical to observe and monitor them when they naturally

occur. It is possible to simulate a fall with healthy volunteers, but it is not possible to identically replicate the conditions of a real fall.

Finite element analysis allows for the simulation of a vast number of scenarios, and to examine the effects of changing a single variable in a complicated problem. In the case of the analysis of the mechanics of falling, finite element analysis can be used to isolate boundary conditions associated with a high probability of hip fracture. The risk of hip fracture could then be reduced by taking measures to avoid these conditions in the event of a real fall. This study explored the effect of altering the orientation of the femur with respect to the impact surface. The largest strains were measured under conditions equivalent to a fall in the posterolateral direction. This information could be considered in the design of hip protectors. It could also influence the positioning of furniture in a room to decrease the likelihood of this kind of fall.

The samples used in this study were a PVC surrogate femur cast from a full size human femur, and a sheep femur. The investigations carried out with each of these samples allowed us to simulate separately the shape of the human proximal femur, and the spatially varying material properties of a femoral bone sample. The successful use of the apparatus in supporting both samples at a range of loading angles without slippage or damage to the samples shows that it can be used in tests with real human proximal femur samples.

A soft tissue simulant foam was used in the sheep femur experiment reported in chapter 5, with the same thickness of foam used for each loading orientation. In a real body, the thickness of the soft tissue is not consistent all the way around the hip joint. The soft tissue thickness profile also varies between individuals. As this model is static, soft tissue thickness only effects the size of the load, so study is required into how the orientation of the femur affects impact force given soft tissue thickness.

The size of the load delivered to the femur in a fall depends on a large number

of factors, including the mass of the faller, the angle a person falls at, and the thickness of the soft tissue at the greater trochanter. The strains compared in this study were induced by a load of 1 N, a very small load compared to those seen in falls. The strains associated with real fall conditions could be estimated from the results of this model by applying a realistic fall load. As neither of the models created for this project simulated a real human bone, this step was not considered useful at this stage. The effect of falling technique on impact load and femur orientation upon impact would have to be assessed in order to estimate the appropriate force for each femur orientation. The experiment and model used in this study do not include the reaction forces caused by muscles and ligaments. A further refinement to the investigation would include these forces, potentially defined by studies into whole-body modelling of reaction forces in a fall [68].

Experiments and models used in this study involved static or quasi-static loading to induce strain in the femurs. This is adequate for assessing the strain distribution and can potentially be used to calculate the size of strains caused by a real fall, but it cannot capture the dynamic response of a fall scenario. A study of the time-dependent strain evolution may be applied to create a greater understanding of fracture initiation and propagation in the proximal femur. The contact mechanics simulation incorporated into the models presented in this thesis have the potential to capture the dynamic interaction within the hip joint, as well as between the femur and the impact surface. There is potential to adapt the finite element model created in this project to include a time dependent force caused by impact through simulated contact boundaries at the femoral head and greater trochanter. The reliability of the results of this model would need to be tested by comparison against strains measured in an impact experiment. It would be necessary to model the soft tissue over the greater trochanter, as well as the compliance of the hip joint and pelvis.

The circumstances of a fall vary between individuals and falls. The nature of the fall depends on environment, such as the surface of the floor and objects around the faller. The condition of the proximal femur, such as whether the faller has osteoporosis or has suffered a hip fracture before, will also have an effect on the strain

---

distribution caused by a fall. Other factors include the mass of the faller, and the thickness of the soft tissue covering the greater trochanter. The benefit of using finite element modelling is that a large number of conditions can be simulated. An aim of this study is to develop the techniques necessary for building a model where the effect of changing the conditions of the fall can be assessed, and the conditions causing hip fracture can be identified. By identifying these conditions, steps can be taken to create a safer environment to reduce the proportion of falls that lead to hip fracture.

## Bibliography

- [1] Falls in the over 65s cost nhs 4.6 million a day. <http://www.ageuk.org.uk/latest-press/archive/falls-over-65s-cost-nhs/>. Accessed: 05-09-2016.
- [2] National hip fracture database annual report 2015. <http://www.nhfd.co.uk/nhfd/nhfd2015reportPR1.pdf>. Accessed: 05-09-2016.
- [3] M.A.K. Liebschner. Biomechanical considerations of animal models used in tissue engineering of bone. *Biomaterials*, 25(9):1697–1714, 2004.
- [4] P. Haentjens, J. Magaziner, C. S. Colón-Emeric, D. Vanderschueren, K. Milisen, B. Velkeniers, and S. Boonen. Meta-analysis: Excess mortality after hip fracture among older women and men. *Annals of Internal Medicine*, 152(6):380–390, 2010.
- [5] Subnational population projections for england: 2014-based projections. <https://www.ons.gov.uk/peoplepopulationandcommunity/populationandmigration/populationprojections/bulletins/subnationalpopulationprojectionsforengland/2014basedprojections>. Accessed: 05-09-2016.
- [6] National hip fracture database extended report 2014. [http://www.nhfd.co.uk/20/hipfractureR.nsf/vwcontent/2014reportPDFs/\\$file/NHFD2014ExtendedReport.pdf](http://www.nhfd.co.uk/20/hipfractureR.nsf/vwcontent/2014reportPDFs/$file/NHFD2014ExtendedReport.pdf). Accessed: 05-09-2016.
- [7] J.B. Lauritzen. Hip fractures: incidence, risk factors, energy absorption, and prevention. *Bone*, 18(1):65S–75S, 1996.
- [8] The national hip fracture database preliminary national report 2009. [http://www.nhfd.co.uk/20/hipfractureR.nsf/vwcontent/2009ReportDownload/\\$File/NHFD2009Report.pdf](http://www.nhfd.co.uk/20/hipfractureR.nsf/vwcontent/2009ReportDownload/$File/NHFD2009Report.pdf). Accessed: 05-09-2016.
- [9] N Li, E Tsushima, and H Tsushima. Comparison of impact force attenuation by various combinations of hip protector and flooring material using a simplified fall-impact simulation device. *Journal of Biomechanics*, 46:1140–1146, 2013.
- [10] T. Markova and K. Schwartz. Does a hip protector reduce the risk of hip fracture in frail elderly patients. *Journal of Family Practice*, 50(3):259, 2001.
- [11] N. M. van Schoor, W. L. Devillé, L. M. Bouter, and P. Lips. Acceptance and compliance with external hip protectors: A systematic review of the literature. *Osteoporosis International*, 13:917924, 2002.
- [12] F. Nabhani and J.S. Bamford. Impact properties of floor coverings and their role during simulated hip fractures. *Journal of Materials Processing Technology*, 153-154:139–144, 2004.

- 
- [13] M. Bessho, I. Ohnishi, T. Matsumoto, S. Ohashi, J. Matsuyama, K. Tobita, M. Kaneko, and K. Nakamura. Prediction of proximal femur strength using a ct-based nonlinear finite element method: Differences in predicted fracture load and site with changing load and boundary conditions. *Bone*, 45:226–231, 2009.
- [14] M. Bessho, I. Ohnishi, J. Matsuyama, T. Matsumoto, K. Imai, and K. Nakamura. Prediction of strength and strain of the proximal femur by a ct-based finite element method. *Journal of Biomechanics*, 40:1745–1753, 2007.
- [15] M. J. Gómez-Benito, J. M. García-Aznar, and M. Doblaré. Finite element prediction of proximal femoral fracture patterns under different loads. *Journal of Biomechanical Engineering*, 127:9–14, 2005.
- [16] J. H. Keyak. Relationships between femoral fracture loads for two load configurations. *Journal of Biomechanics*, 33:499–502, 2000.
- [17] J.H. Keyak, I.Y. Lee, and H.B. Skinner. Correlations between orthogonal mechanical properties and density of trabecular bone: use of different densitometric measures. *Journal of Biomedical Materials*, 28:1329–1336, 1994.
- [18] J. H. Keyak, S. A. Rossi, K. A. Jones, and H. B. Skinner. Prediction of femoral fracture load using automated finite element modeling. *Journal of Biomechanics*, 31:125–133, 1998.
- [19] J.E.M. Koivumäki, J. Thevenot, P. Pulkkinen, V. Kuhn, T. M. Link, F. Eckstein, and T. Jämsä. Ct-based finite element models can be used to estimate experimentally measured failure loads in the proximal femur. *Bone*, 50:824–829, 2012.
- [20] T. Ota, I. Yamamoto, and R. Morita. Fracture simulation of the femoral bone using the finite-element method: How a fracture initiates and proceeds. *Journal of Bone and Mineral Metabolism*, 17:108–112, 1999.
- [21] N. Wakao, A. Harada, Y. Matsui, M. Takemura, H. Shimokata, M. Mizuno, M. Ito, Y. Matsuyama, and N. Ishiguro. The effect of impact direction on the fracture load of osteoporotic proximal femurs. *Medical Engineering & Physics*, 31:1134–1139, 2009.
- [22] Z. Yosibash, N. Trabelsi, and C. Milgrom. Reliable simulations of the human proximal femur by high-order finite element analysis validated by experimental observations. *Journal of Biomechanics*, 40:3688–3699, 2007.
- [23] J.H. Keyak, H.B. Skinner, and J.A. Fleming. Effect of force direction on femoral fracture load for two types of loading conditions. *Journal of Orthopaedic Research*, 19:539–544, 2001.
- [24] W.A. Brekelmans, H.W. Poort, and T.J. Slooff. A new method to analyse the mechanical behaviour of skeletal parts. *Acta Orthopaedica Scandinavica*, 43(5):301–317, 1972.
- [25] M.E. Taylor, K.E. Tanner, M.A. Freeman, and A.L. Yettram. Stress and strain distribution within the intact femur: compression or bending? *Medical Engineering & Physics*, 18(2):122–131, 1996.
- [26] P.K. Basu, A.G. Beall, D.J. Simmons, and M. Vannier. 3-d femoral stress analysis using ct scans and p-version fem. *Biomaterials, Medical Devices, and Artificial Organs*, 13:163–186, 1986.

- [27] M. Kaneko, I. Ohnishi, T. Matsumoto, S. Ohashi, M. Bessho, N. Hayashi, and S. Tanaka. Prediction of proximal femur strength by a quantitative computed tomography-based finite element method creation of predicted strength data of the proximal femur according to age range in a normal population. *Modern Rheumatology*, 26:151–155, 2016.
- [28] L. Mosekilde, S.M. Bentzen, G. Ørtoft, and J. Jørgensen. The predictive value of quantitative computed tomography for vertebral body compressive strength and ash density. *Bone*, 10(6):465–470, 1989.
- [29] G. P. Vose and A. L. Kubala. Bone strength-its relationship to x-ray determined ash content. *Human Biology*, 31(3):261–270, 1959.
- [30] R.J. McBroom, W.C. Hayes, Edwards W.T., Goldberg R.P., and A.A. White, III. Prediction of vertebral body compressive fracture using quantitative computed tomography. *The Journal of Bone and Joint Surgery (American Volume)*, 67(8):1206–1214, 1985.
- [31] Cann C.E. and Genant H.K. Precise measurement of vertebral mineral content using computed tomography. *Journal of Computer Assisted Tomography*, 4(4):493–500, 1980.
- [32] A. Nazarian, B. D. Snyder, D. Zurakowski, and R. Müller. Quantitative micro-computed tomography: A non-invasive method to assess equivalent bone mineral density. *Bone*, 43:302–311, 2008.
- [33] T. S. Keller. Predicting the compressive mechanical behaviour of bone. *Journal of Biomechanics*, 27(9):1159–1168, 1994.
- [34] A. C. Laing and S. N. Robinovitch. Low stiffness floors can attenuate fall-related femoral impact forces by up to 50% without substantially impairing balance in older women. *Accidental Analysis and Prevention*, 41:642–650, 2009.
- [35] S. N. Robinovitch, T. A. McMahon, and W. C. Hayes. Force attenuation in trochanteric soft tissues during impact from a fall. *Journal of Orthopaedic Research*, 13:956–962, 1995.
- [36] P. Kannus, J. Parkkari, and J. Poutala. Comparison of force attenuation properties of four different hip protectors under simulated falling conditions in the elderly: an in vitro biomechanical study. *Bone*, 25(2):229–235, 1999.
- [37] N.M. van Schoor, A.J. van der Veen, L.A. Schaap, T.H. Smit, and P. Lips. Biomechanical comparison of hard and soft hip protectors, and the influence of soft tissue. *Bone*, 39:401–407, 2006.
- [38] S. Derler, A.B. Spierings, and K.U. Schmitt. Anatomical hip model for the mechanical testing of hip protectors. *Medical Engineering & Physics*, 27(6):475–485, 2005.
- [39] S. Li, A. Abdel-Wahab, E. Demirci, and V. V. Silberschmidt. Fracture process in cortical bone: X-fem analysis of microstructured models. *International Journal of Fracture*, 184:43–55, 2013.
- [40] S. Li, A. Abdel-Wahab, and V. V. Silberschmidt. Analysis of fracture processes in cortical bone tissue. *Engineering Fracture Mechanics*, 110:448–458, 2013.

- [41] B.E. Groen, V. Weerdesteyn, and J. Duysens. The relation between hip impact velocity and hip impact force differs between sideways fall techniques. *Journal of Electromyography and Kinesiology*, 18:228–234, 2008.
- [42] J. Lo and J.A. Ashton-Miller. Effect of pre-impact movement strategies on the impact forces resulting from a lateral fall. *Journal of Biomechanics*, 41:1969–1977, 2008.
- [43] T. M. Ryan and R. A. Ketcham. Angular orientation of trabecular bone in the femoral head and its relationship to hip joint loads in leaping primates. *Journal of Morphology*, 265(3):249–263, 2005.
- [44] M. M. Barak, D. E. Lieberman, and J. J. Hublin. A wolf in sheep’s clothing: Trabecular bone adaptation in response to changes in joint loading orientation. *Bone*, 49:1141–1151, 2011.
- [45] C. M. Les, J. H. Keyak, S. M. Stover, K.T. Taylor, and A.J. Kaneps. Estimation of material properties in the equine metacarpus with use of quantitative computed tomography. *Journal of Orthopaedic Research*, 12:822–833, 1994.
- [46] J.R. Calvert and R.A. Farrar. *An Engineering Data Book*. Calvert Technical Press, 1998.
- [47] S. H. Teoh, Z. G. Tang, and G. W. Hastings. Thermoplastic polymers in biomedical applications: Structures, properties and processing. In Jonathan Black and Garth Hastings, editors, *Handbook of Biomaterial Properties*. Springer US, Boston, MA, 1998.
- [48] A.C. Courtney, E.F. Wachtel, E.R. Myers, and W.C. Hayes. Effects of loading rate on strength of the proximal femur. *Calcified Tissue International*, 55(1):53–58, 1994.
- [49] S Backman. The proximal end of the femur. *Acta radiologica. Supplementum.*, 146:1–16, 1957.
- [50] T.P. Pinilla, K.C. Boardman, M.L. Bouxsein, E.R. Myers, and W.C. Hayes. Impact direction from a fall influences the failure load of the proximal femur as much as age-related bone loss. *Calcified Tissue International*, 58(4):231–235, 1996.
- [51] H. Singh Ranu. The thermal properties of human cortical bone: an in vitro study. *Engineering in Medicine*, 16:175–176, 1987.
- [52] W.N. Sharpe. *Springer Handbook of Experimental Solid Mechanics*. Springer, New York City, 2008.
- [53] T.M. Wright and W.C. Hayes. Strain gage application on compact bone. *Journal of Biomechanics*, 12:471–475, 1979.
- [54] J. Cordey and E. Gautier. Strain gauges used in the mechanical testing of bones part ii: “in vitro” and “in vivo” technique. *Injury*, 30:SA14 – SA20, 1999.
- [55] P. Eyerer and R. Jin. Influence of mixing technique on some properties of pmma bone cement. *Journal of Biomedical Materials Research*, 20:1057–1094, 1986.

- [56] H. J. Jung, G. Vangipuram, M. B. Fisher, G. Yang, S. Hsu, J. Bianchi, C. Ronholdt, and S.L. Woo. The effects of multiple freeze-thaw cycles on the biomechanical properties of the human bone-patellar tendon-bone allograft. *Journal of Orthopaedic Research*, 29(8):1193–1198, 2011.
- [57] J. M. Shaw, S. A. Hunter, J. C. Gayton, G. P. Boivin, and M. J. Prayson. Repeated freeze-thaw cycles do not alter the biomechanical properties of fibular allograft bone. *Clinical Orthopaedics and Related Research*, 470:937–943, 2012.
- [58] J.H. Zar. *Biostatistical Analysis*. Prentice Hall, Upper Saddle River, 5 edition, 2010.
- [59] Tensile property testing of plastics. <http://www.matweb.com/reference/tensilestrength.aspx>. Accessed: 02-08-2016.
- [60] A.E. Anderson, C.L. Peters, B.D. Tuttle, and J.A. Weiss. Subject-specific finite element model of the pelvis: development, validation and sensitivity studies. *Journal of Biomechanical Engineering*, 127:364–373, 2005.
- [61] E. Doukhitch, M. Salamah, and E. Ozen. An efficient approach for trilateration in 3d positioning. *Computer Communications*, 31:4124–4129, 2008.
- [62] N. Y. P. Afoke, P. D. Byers, and W. C. Hutton. Contact pressures in the human hip joint. *The Journal of bone and joint surgery. British volume*, 69:536–541, 1987.
- [63] Comsol. *Comsol Structural Mechanics Module Users Guide*, 4.3 edition, May 2012.
- [64] K. L. Johnson. *Contact Mechanics*. Cambridge University Press, Cambridge, 1985.
- [65] W. C. Young and R. G. Budynas. *Roark's Formulas for Stress and Strain*. McGraw-Hill, New York, 7 edition, 2002.
- [66] S. V. Hainsworth, R. J. Delaney, and G. N. Ruttly. How sharp is sharp? towards quantification of the sharpness and penetration ability of kitchen knives used in stabbings. *International Journal of Legal Medicine*, 122:281–291, 2008.
- [67] R. J. Barlow. *Statistics: A Guide to the Use of Statistical Methods in the Physical Sciences*. Wiley, Chichester, 1989.
- [68] A.T.M. Phillips. The femur as a musculo-skeletal construct: A free boundary condition modelling approach. *Medical Engineering & Physics*, 31:673–680, 2009.